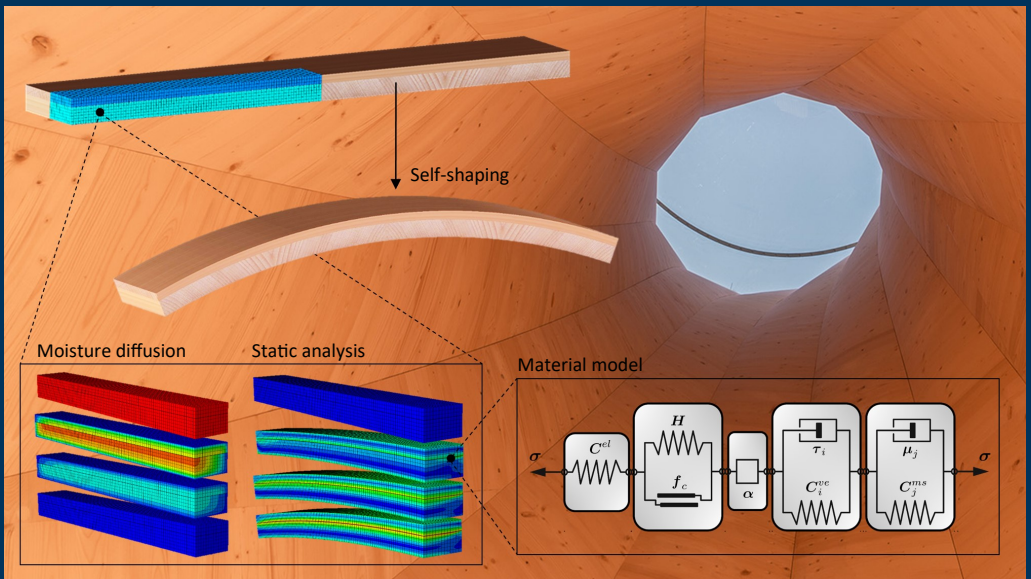


Philippe Grönquist

Smart Manufacturing of Curved Mass Timber Components by Self-Shaping



DISS. ETH NO. 26610

SMART MANUFACTURING OF CURVED MASS
TIMBER COMPONENTS BY SELF-SHAPING

A dissertation submitted to attain the degree of
DOCTOR OF SCIENCES of ETH ZURICH
(Dr. sc. ETH Zurich)

presented by
PHILIPPE GRÖNQVIST
MSc ETH Civil Eng
born on 17 June 1990
citizen of Zug (ZG)

accepted on the recommendation of
Prof. Dr. Ingo Burgert, examiner
Prof. Dr. Kristofer Gamstedt, co-examiner
Prof. Dr. Josef Füssl, co-examiner
Dr. Markus Rüggeberg, co-examiner

2020

Philippe Grönquist: *Smart manufacturing of curved mass timber components by self-shaping*, © 2020, distributed under: Creative Commons Attribution 4.0 International (CC-BY).

DOI: 10.3929/ethz-b-000405617

Cover image background: Urbach Tower interior (Photo: © ICD/ITKE University of Stuttgart)

Für Sarah

ABSTRACT

With the rise of complex and free-form timber architecture enabled by digital design and fabrication, timber manufacturing companies increasingly need to produce curved components. In this thesis, a novel approach for the manufacturing of curved timber building components is proposed and analyzed. Following biological role models such as the bending of pine cone scales, a smart way to curve wood at large-scale is given by the biomimetic concept of bi-layered laminated wood. This principle enables large programmed material deformations upon controlled moisture content change. The main objectives of this thesis are the in-depth understanding of the mechanics of self-shaping wood bilayers and the up-scaling of the already known principle from the laboratory to the industrial scale in order to enable an application as form-stable curved elements in architecture. Hereby, the main challenges addressed are the accurate prediction of shape-change in terms of the natural variability in wood material parameters, the scale-dependent impact of moisture gradients on mechanical behavior, and the influence of wood-specific time- and moisture-dependent deformation mechanisms such as creep or mechano-sorption in the shaping process. Major impacts of these aspects on the shaping behavior could be demonstrated by the use of continuum-mechanical material models adapted to wood, both in the form of analytical and numerical models. Based on the gained insight, the up-scaling process to industrial manufacturing was successfully made possible. A collaborative project realized in 2019, the 14 m high *Urbach tower*, is presented as a proof of concept for application and competitiveness of the novel biomimetic method for production of curved mass timber components. Furthermore, next to self-shaping by bending to single-curved components, possibilities and limitations for achieving double-curved structures using wood bilayers in a gridshell configuration are analyzed and discussed.

ZUSAMMENFASSUNG

Die heutige Architektur des Holzbaus wird zunehmend von komplexen Freiformen geprägt, welche dank digitaler Entwurfs- und Herstellungsprozessen ermöglicht werden. Dies erfordert eine vermehrte Produktion von gekrümmten Holzbauteilen seitens der Holzbaufirmen. In der vorliegenden Arbeit wird ein neuartiger Herstellungsprozess für gekrümmte Holzelemente entwickelt und untersucht. Dabei werden Prinzipien der Biomimetik angewendet, wie zum Beispiel das Bilayerprinzip, welches sich im (feuchteabhängigen) selbstöffnenden Kiefernzapfen findet. Dieses Prinzip wird auf Holz angewendet in Form von zwei verklebten Schichten mit unterschiedlicher Faserorientierung, die miteinander verklebt einen sogenannten Holzbilayer ergeben, welcher nach Feuchteänderung grosse Verformungen zeigt. Hierbei ist das Hauptziel der Arbeit, ein vertieftes Verständnis der Mechanik des selbst-formenden Holzes zu gewinnen, anschliessend dieses Prinzip auf grosser Skala industriell anzuwenden, um schlussendlich formstabile gekrümmte Holzbauteile für den Holzbau zu erhalten. Die Herausforderung bildet dabei hauptsächlich die exakte Vorhersage der Krümmung der Holzbilayer in Anbetracht der Variabilität in den mechanischen Eigenschaften des Holzes, des zeit- und feuchteabhängigen mechanischen Verhaltens, wie zum Beispiel Kriechen oder Mechano-Sorption, und des Einflusses von Feuchtegradienten über die Dicke der Holzbilayer und deren skalenabhängiges Verhalten in Bezug auf die Selbstformung. Durch die Verwendung von komplexen, kontinuum-mechanischen analytischen und numerischen Modellen konnten wichtige Einflüsse dieser Aspekte nachgewiesen und verstanden werden. Basierend auf diesen Erkenntnissen wurde ein industrieller Herstellungsprozess für selbst-geformte, gekrümmte Holzbauteile erfolgreich entwickelt. Als Machbarkeitsnachweis des neuen biomimetischen Herstellungsprozesses für gekrümmtes Holz in Massivbauweise konnte im Rahmen eines Kollaborationsprojekts 2019 der 14 m hohe *Urbach Turm* realisiert werden. Weiterführend wird in dieser Arbeit die Möglichkeit untersucht, doppelt-gekrümmte Holzstrukturen durch Selbst-formung zu realisieren. Hierbei werden Möglichkeiten und Grenzen von Gitterschalen-Konstruktionen, die aus Holzbilayern aufgebaut sind, aufgezeigt und diskutiert.

ACKNOWLEDGEMENTS

Because this thesis is not my work alone but rather the result of contributions from many people, I would like to sincerely thank:

- My supervisors - for your mentoring, the introduction to science, and for having me here during three years: First and foremost *Markus Rüggeberg*, but also *Falk Wittel*, and *Ingo Burgert*.
- The co-examiners: *Kristofer Gamstedt* and *Josef Füssl*.
- My many collaborators in science and industry - for your contribution, support, and the nice collaborations: *Dylan Wood*, *Achim Menges*, *Patrick Huser*, *Josua Preisig*, *Markus Fitzi*, *David Riggenbach*, *Urban Jung*, *Martin Antemann*, *Katharina Lehmann*, *Lotte Aldinger*, *Simon Bechert*, *Jan Knippers*, *Michael Klippel*, *Martin Viertel*, *Dominik Werne*, *Katharina Müller*, *Fabian Mahrt*, *Stefan Bockel*, *Peter Niemz*.
- My working colleagues and friends - for your help and support, and the nice and funny moments we shared: In alphabetical order *Adrian Wick*, *Andrea Merletti*, *Chiara Vailati*, *Christian Goldhahn*, *Christopher Dreimol*, *Daniel Widner*, *Erik Bachtiar*, *Etienne Cabane*, *Etienne Trachsel*, *Gilberto Siquiera*, *Huizhang Guo*, *Jianguo Sun*, *Josef Taut*, *Julia Bucher*, *Katerina Andric*, *Kunkun Tu*, *Liuyang Han*, *Livia Schneider*, *Luca Schelbli*, *Marcel Janser*, *Maria Adobes-Vidal*, *Marion Frey*, *Marta Vidiella*, *Mathilde Lecomte*, *Merve Özparpucu*, *Michael Hausmann*, *Miki Tsunehisa*, *Munish Chanana*, *Oliver Kläusler*, *Paul-Antoine Spies*, *Philipp Hass*, *Raphaela Hellmayr*, *Samuel Olaniran*, *Sandro Stucki*, *Sanja Kostic*, *Sarah Lämmlein*, *Selin Vitas*, *Sophie Koch*, *Stéphane Croptier*, *Styfen Schär*, *Thomas Schnider*, *Tobias Keplinger*, *Walter Sonderegger*, *Wei Qu*, *Yaru Wang*, *Yasmine Mekacher*, *Yong Ding*.
- My family and friends - for your continuous support all my life.

Finally, I want to apologize to the person that has provided me with the greatest support of all, during this time and during a fair part of my life, and without whom this work would not have been possible: *Sarah*.

CONTENTS

1	INTRODUCTION	1
1.1	Motivation	1
1.2	Background and research gap	2
1.3	Objectives	3
1.4	Outline of thesis	4
2	BIOMIMETIC SELF-SHAPING COMPOSITES	7
2.1	The concept of biomimetics	7
2.2	Self-shaping biological role models	8
2.3	Self-shaping mechanisms	9
2.4	Physics of self-shaping composites	10
2.5	Relevant implications for self-shaping wood	15
2.6	Applications of self-shaping wood composites	17
3	THE MATERIAL WOOD	19
3.1	Wood structure	19
3.2	Wood-water interaction	24
3.3	Mechanical behavior	28
3.4	Wood computational mechanics	30
4	MODELING AND DESIGN OF THIN BENDING WOODEN BILAYERS	35
4.1	Publication preamble	35
4.2	Introduction	37
4.3	Theory	38
4.4	Materials and methods	42
4.5	Results	44
4.6	Discussion	47
4.7	Conclusions	50
5	ANALYSIS OF HYGROSCOPIC SELF-SHAPING WOOD AT LARGE-SCALE	53
5.1	Publication preamble	53
5.2	Introduction	55
5.3	Materials and Methods	58
5.4	Results	61

5.5	Discussion	65
5.6	Summary	68
5.7	Supplementary Materials	69
6	INDUSTRIAL APPLICATION OF SELF-SHAPING WOOD	79
6.1	Introduction	79
6.2	The Urbach tower: Project description	82
6.3	Self-shaping manufacturing process	85
6.4	Structural testing	92
7	HYGROMORPHIC SELF-SHAPING WOOD GRIDSHELL STRUCTURES	101
7.1	Publication preamble	101
7.2	Introduction	103
7.3	Methods	105
7.4	Results and discussion	106
7.5	Application	110
7.6	Conclusions	112
7.7	Supplementary Materials	113
8	SYNTHESIS	117
8.1	General discussion	117
8.2	Summary	130
8.3	Significance and application potential	131
8.4	Outlook	133
	BIBLIOGRAPHY	137

INTRODUCTION

1.1 MOTIVATION

Timber and wood products are common materials used in the building sector where they have a long tradition. The availability, machinability, and excellent mechanical properties with respect to density make wood a lightweight structural material perfectly fitted to the needs of the construction sector. As for today, wood still represents the only truly sustainable material in this vast sector. In fact, wood, the biomass produced by trees following the photosynthesis reaction, serves as natural carbon storage. If stored in large amount over periods of time surpassing the natural life-expectancy of trees, and preferably in the functional form of structural building components, wood represents a significant carbon sink in view of atmospheric CO₂ reduction [1]. Nowadays, the use of mass timber products in construction, especially cross-laminated timber (CLT) [2, 3], represents one of the few effective methods for the modern building sector to address climate change [4].

Competitiveness among building materials is nowadays not only a question of costs, availability, structural performance, and sustainability, but also of aesthetics and freedom in form and design space. Contemporary architecture often favors curved and complex-shaped building elements. And wood can increasingly fulfill these demands [5, 6]. However, compared to casting materials, this often comes with the inherent drawback of high production costs due to the complexity of free-form shape-giving. Current manufacturing standards involve techniques such as subtractive milling-to-shape or extensive formwork and machines to bend, press, and glue thin timber lamellas to the desired curved shapes.

The motivation of this work is to contribute towards the establishment of a new and alternative manufacturing technique for complex-shaped wood components with reduced costs. The new method builds on principles of the prominent biomimetics field in science and engineering of the last two decades. Specifically, wood can be programmed to act as a hygromorphic self-shaping bi-layered composite [7, 8], which e.g. is mimicking the bending of pine cone scales upon drying [9]. With wood, this concept has the unique potential to be applied at a large-scale for the manufacturing of

curved mass timber products such as curved CLT. Hereby, the required form-stability with respect to further changes in moisture content of the wood shall be given by applying a stack-lamination of multiple, previously self-shaped, wood bilayer components. This novel concept removes the mechanical compatibility of the curved composite to further self-shape by creating a multi-layer component with a number of layers equal or greater than four. The one-time actuation by moisture-content change and the subsequent shape-freezing by stack-lamination foresee a more efficient and completely revolutionary use of the material wood, and with this, its further promotion in the construction sector.

1.2 BACKGROUND AND RESEARCH GAP

As wood is a biological material with complex hierarchical structure, its mechanical behavior on the bulk material scale inherits an equivalently complex behavior [10]. Under given mechanical and climatic loads, multiple anisotropic phenomenological deformation mechanisms can be observed. In fact, these deformation behaviors, in the case of wood namely elasticity, visco-elasticity, plasticity, mechano-sorption, and hygro-expansion often manifest in coupled and moisture-dependent manner. In numerical simulations, constitutive material models accounting for these mechanisms are usually composed of a large number of mechanical material parameters [11]. The complexity of the mechanical behavior is further increased by the natural and aleatory variability in these parameters [12, 13]. The influences of both aspects on the shaping behavior of self-shaping wood bilayer composites were up to date never investigated in the context of increasing precision in shape prediction.

Next to material parameters and mechanical behavior, geometry and assembly of the self-shaping composite are decisive in dictating deformation and shape [14]. A diversity of shapes is achievable in function of material orientation, width, length, and especially thickness of the composite. While the influence of geometry has previously been investigated for the case of narrow bilayer strips [7], the effect of thickness, especially towards values that enable large-scale applications, has not been studied yet. Next to influencing extent of shaping, lamella thickness also influences kinetics of shaping. The hygromorphic wood composite is in the motion of shaping while, over its whole body, the moisture content is not yet in equilibrium to the climate. Moisture diffusion processes and their time-dependency thus directly influence the time-dependent mechanical response of the composite.

Up to date, gradients in state-variables such as moisture and their coupling to rate-dependent mechanical behavior, which is essential at large-scale, have not been investigated in any field of self-shaping materials.

Finally, a characteristic of bi-layered self-shaping composites is that the change in their Gaussian curvature is a function of their geometric configuration [14, 15]. In the case of wood, systematic optimization studies using numerical mechanical simulations in order to achieve self-shaping double-curved structures that deform along multiple directions at the same time have not been conducted yet.

1.3 OBJECTIVES

The objectives of the fundamental investigations in this thesis are to:

- Optimize the parameters of self-shaping wood composites for application at large-scale with increased lamellae thickness. This includes characterization of the influence of material parameters, geometry, and change in moisture conditions of the shaping composite as well as the moisture diffusion process and its effect on time-dependent mechanical behavior.
- Characterize the predictability of shape by the use of complex numerical mechanical simulations. Especially, the variability in prediction shall be assessed in terms of the variability in model input parameters, with respect to the natural variability in wood material properties.
- Investigate and optimize different structure designs using wood in order to achieve significant changes in Gaussian curvature by self-shaping towards dome-like shell structures.

This thesis was conducted in the frame of an *Innosuisse* industry project with the aim to implement a large-scale self-shaping manufacturing process for efficient production of curved mass timber products. Hereby, the additional technical objectives include:

- Developing an application-based design and integrated manufacturing process. Therewith, freedom in design of complex curved structures shall be enabled by a custom adjusting of the manufacturing of the shaping components.

- Assessing influence of industrial production on the shaping process and its fundamental feasibility in industry. This includes optimization of the drying process for bilayers that shape starting from a wet state, and of the manufacturing process with respect to the quality of lamination and adhesive used. In addition, influences of sorting aspects such annual ring orientation and moisture content distribution of boards prior to the shaping shall be analyzed with respect to the context of an industrial (less controlled) environment in contrast to laboratory (controlled) conditions. Furthermore, resulting structural properties shall be assessed in view of load-bearing applications.

1.4 OUTLINE OF THESIS

This cumulative thesis is divided into eight chapters. After the present chapter, in which the motivation, the background, and the objectives of the thesis are stated, two theoretical chapters follow in order to prepare the reader to the topics of the main investigations. In chapter 2, an introduction and theoretical background is given on the biomimetic self-shaping mechanism and its application to wood. Chapter 3 introduces relevant wood material behavior ranging from structure, water interaction, to mechanical behavior and simulation. Chapters 4-7 then present the main investigations of this thesis. The chapters 4 and 5 feature separate publications about design and modelling, while chapter 6 showcases an example of industrial application enabled by the findings from chapters 4 and 5 in the frame of the *Innosuisse* project. Ultimately, chapter 7 features a publication about the continuing fundamental and applied research on achieving shell structures by self-shaping. The main investigations compile as follows:

- Chapter 4 - **Paper I:** *Modeling and design of thin bending wooden bilayers*
- Chapter 5 - **Paper II:** *Analysis of hygroscopic self-shaping wood at large-scale for curved mass timber structures*
- Chapter 6 - **Application:** *The Urbach Tower & the industrial application of self-shaping wood*
- Chapter 7 - **Paper III:** *Computational analysis of hygromorphic self-shaping wood gridshell structures*

Chapter 8 subsequently synthesizes the main findings of the publications, discusses the latter in a broader context ranging from fundamental

to applied considerations, and provides an outlook. An integral bibliography, containing all references cited in this thesis, including the citations from papers I-III, is provided at the end.

BIOMIMETIC SELF-SHAPING COMPOSITES

2.1 THE CONCEPT OF BIOMIMETICS

Biomimetics has been one of the major concepts in materials science and engineering starting in the early 1990s [16]. The study, imitation, and transfer of nature's systems and models in order to solve applied, material-related problems is nowadays vastly prevalent [17, 18]. In nature, over time, living organisms have optimized and adapted their structure to fulfill necessary purposes related to their survival. Researchers and engineers, since centuries, have tried to mimic biological concepts where structure and form follow a predefined function. One often mentioned historical example is Leonardo Da Vinci's study of bird anatomy with the vision in mind of creating a man-made flying machine [19].

Functional adaptations can be identified in nature's material structures not only at the macroscopic but also at the micro- and nano-scale [20, 21]. Almost all biological materials are to some extent hierarchically structured. From bottom-up, each structure at each hierarchical scale is often optimized given specific boundary conditions [22]. Such hierarchical features have indeed been equally inspiring to humanity. A worth-mentioning example of applying biomimetics in the context of wood is the mimicking of its cellulose microfibril tilt angle [23] and its structure for the development of materials and composites with high work of fracture [24, 25].

The relevance and benefits of biomimetics for construction engineering and architecture was early-on realized [26]. Not only can biomimetics help in optimizing structures but it can also contribute towards sustainability in the construction sector [27]. Up to date, architects and engineers have indeed successfully applied biomimetic concepts to design structures [28–30]. In this chapter, a specific biomimetic principle, the inspiration from self-shaping plant tissue structures, will be explained and discussed in the context of application to the material wood.

2.2 SELF-SHAPING BIOLOGICAL ROLE MODELS

Many plant species have developed tissue structures that display large deformations when their moisture content (MC) is changed. In the exemplary case of some fruits, when the tissue structure containing the seeds is attached to the mother plant, it is typically water-saturated and in its native shape configuration, protecting the growing seeds. As soon as the mother plant releases the fruit, it stops being alimented and dries out at the air. During drying, the large deformations that can be observed are likely programmed by nature for efficient opening of the structure resulting in seed release. An example is the Chinese wisteria (*Wisteria sinensis*). Both halves of its large haricot-like seed pod extensively twist upon drying (Fig. 2.1). The twisting splits the seed pod and efficiently prevents any possibility of the pod to remain closed.

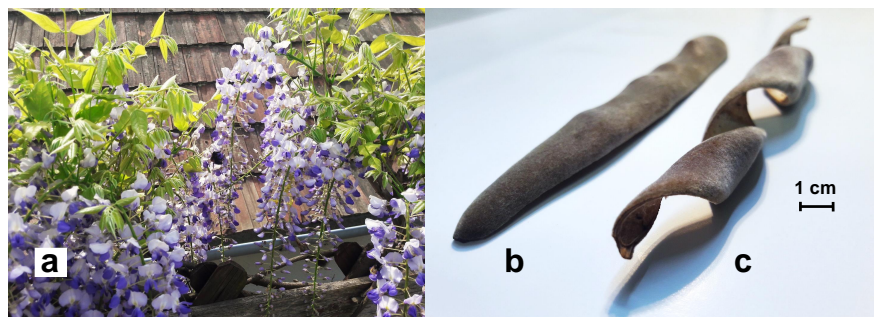


FIGURE 2.1: **Example of self-shaping biological role model.** a: *Wisteria sinensis* during blooming season. b: Water saturated seed pod of *Wisteria sinensis* (half piece, re-wetted). c: Air-dried seed pod (half piece) displaying extensive self-shaping in the form of combined bending and torsion.

While *Wisteria sinensis* has not yet been specifically studied, the mechanisms of many other examples, often referred to as hygromorphs, were thoroughly studied and analyzed. Similar to the case of molecular chirality [31], a chirality-creating mechanism of bi-layered anisotropic plant tissue was identified and mathematically described for the twisting seed pods of *Bauhinia variegata* [14]. Further prominent examples of natural self-shaping mechanisms include the opening of the pine cone scales [9, 32, 33], the bending of wheat awns [34], or the twisting of rod-like structures such as the stork's bill [35] in function of humidity. Similar to these programmed

bilayer self-shaping mechanisms in dead plant tissue, living plant tissue movement, to some extent is controlled by a coupling of change in hydraulic conditions and mechanical properties of the tissue [36]. An example is the natural shaping of leaves during their growth.

Following the concept of biomimetics, many of these natural role models have recently been highlighted for innovative applications of self-shaping in different fields [37–46]. Recent literature reviews highlight further examples and application possibilities [47, 48]. In all the mentioned plant-based role models, nature has elegantly optimized the system to act at the same time as actuator and structure. This will represent a key aspect later-on for the case of self-shaping wood as structural building material in construction. In the next sections, the complex shaping mechanism will be concisely described, before a review on its application to wood will be given in the last section of this chapter.

2.3 SELF-SHAPING MECHANISMS

Most of the previously mentioned biological role models have the common attribute of their self-shaping originating from a bi-layered composite structure. In fact, these large deformations are caused by only small differences of strains in one layer respective to the other. Plant cell wall tissue is composed of polymer material that shrinks or swells in function of the amount of bound water. Another important attribute is the anisotropy of the tissue, which results in direction-dependent swelling and shrinkage and mechanical stiffness. Consequently, the amount of stretching caused by a change in MC is depending on local tissue direction. It is now straightforward, that two bonded layers made up of such tissue, with a significant angle ϕ between their principal directions of shrinkage or swelling, will bend because of the differential strain (ϵ) along the thickness (h) direction. Hereby, the curvature of bending (κ) follows the simple compatibility condition $\kappa = \epsilon/h$. For plant systems, the shaping is thus inherently programmed in the tissue and results as a response to changes in environmental conditions only, i.e. changes in relative humidity or temperature [49].

Next to this, self-shaping mechanisms can result from adequate composite structures made from various other types of materials. Some examples are given by electro-thermo-hygro sensitive polymers [50], temperature differences in metals [51], mechanical pre-stretch of soft materials [14], magnetically actuated matter [52], moisture-driven buckling of plate composite assemblies [53], pneumatic elastomers [54], or wetting of natural fibre com-

posite mats with a thickness-gradient of fibre orientation [55]. However, the simplest form of self-shaping is probably represented by inducing a state-variable gradient over a homogeneous cross-section, e.g. a one-sided wetting of paper [56].

Another example, where understanding the origin of a self-shaping mechanism is of practical relevance, are the process-induced distortions by residual stresses created by curing laminated high performance carbon fibre reinforced composites with a thermo-setting matrix [57, 58]. Here, the residual stresses leading to self-shaping are a result of coupled thermal, chemical, and mechanical induced strains due to the curing in a shape-giving mold. The (curved) mold shape is often designed based on a prior simulation and analysis of the superimposed (self-shaping) distortions, such that the composite part automatically adopts the desired (flat) shape after removing from the mold (spring-in effect).

2.4 PHYSICS OF SELF-SHAPING COMPOSITES

Application of mathematical and mechanical theories to plant actuation systems, such as in the case of the snapping of the Venus fly trap [59], has tremendously helped understanding the fundamental mechanisms at play. Hereafter, a general theory, derived and described in the work of Armon et al. [14], will be used to explain the multitude of possible resulting shapes of self-shaping bi-layered composites. First, a basic notion will be given on curvature of surfaces.

2.4.1 Curvature of surfaces

In differential geometry, in three-dimensional Euclidean space (E^3), *principal curvatures* (κ_1 and κ_2) at a given point on a surface are defined as the eigenvalues of the shape operator [60]. Its eigenvectors point in the directions of maximum and minimum curvatures, which are given by κ_1 and κ_2 (curvatures of red lines in Fig. 2.2).

For a 2D smooth surface embedded in E^3 , the *Gaussian curvature* is given as $K = \kappa_1 \kappa_2$. Hereby, K is an intrinsic invariant, as under any isometric deformation of the surface, i.e. line elements on the surface do not change length, area elements do not change area, and angles between line elements remain constant, K remains constant.

In the context of self-shaping composites, the *natural curvature* κ_0 is the curvature that a self-shaping composite would adopt if it was in an in-

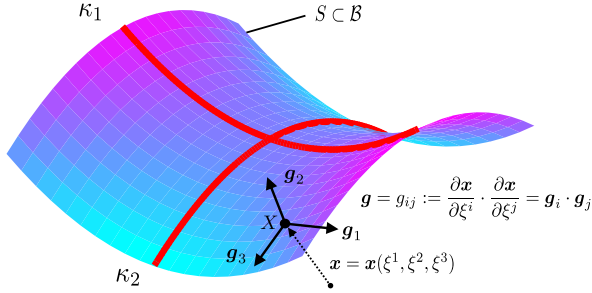


FIGURE 2.2: **Principal curvatures κ_1 and κ_2 of a 2D surface S on a body \mathcal{B} in \mathbb{E}^3 .**
 Bottom right: Definition of the metric tensor \mathbf{g} of S at point X (with position vector \mathbf{x} and convected coordinates ξ^1, ξ^2, ξ^3) as dot product of tangent vectors \mathbf{g}_i .

finitely narrow strip configuration (such as in Fig. 2.3c). Therefore, in this configuration, the curvature of the strip is independent of the curvature along other directions, which would not be the case in a shell configuration.

2.4.2 Self-shaping-induced elastic energy

Natural hygromorphs become, under any other MC state than their native state (water-saturated tissue), so called non-Euclidean bodies [61]. Consequently, they do not possess a configuration, at rest or under any external stress state, which is internally stress-free. The resulting strain tensor can be expressed by

$$\boldsymbol{\varepsilon} = \frac{1}{2}(\mathbf{g} - \bar{\mathbf{g}}), \quad (2.1)$$

where \mathbf{g} is a metric tensor (see ¹ and Fig. 2.2) describing the surface configuration after differential swelling or shrinkage has occurred in the bilayer hygromorph structure. Here, a reference metric tensor $\bar{\mathbf{g}}$ is used to describe a reference surface with stretches and curvatures that would make the surface free of residual stresses. The difference of both these metric tensors allows for the concept of a strain tensor describing a self-shaped

¹ A metric tensor inherently describes properties of a surface regardless of its type of parametrization and basis coordinate system. The metric tensor allows for deriving surface-specific values such as length of line elements or angles between line elements. For further information see [60].

non-Euclidean body that has changed its Gaussian curvature during shaping, such that $\mathbf{g} \neq \bar{\mathbf{g}}$. The difference to classical continuum mechanics is that here $\bar{g}_{ij} \neq 0$, as usually, \mathbf{g} can directly be related to $\boldsymbol{\varepsilon}$ (see ²). Assuming linear elasticity, the residual energy per unit volume (w), and the energy over a body \mathcal{B} with reference volume V (E), are given by

$$w = \frac{1}{2} C_{ijkl} \varepsilon_{ij} \varepsilon_{kl}, \text{ and } E = \int_{\mathcal{B}} w J dV. \quad (2.2)$$

Here, C_{ijkl} is the 4th order stiffness tensor written in terms of Einstein summation notation (indices i, j, k, l) containing the material's elastic parameters and J is a Jacobian.

Now considering a plate geometry, e.g. an idealized 2D surface in \mathbf{E}^3 (such as in Fig. 2.2) with an attributed thickness h of small value, e.g. $h \ll (w, l)$ where w is the width and l the length of the plate, Armon et al. [14] derived an expression for E in terms of the first and second fundamental forms \mathbf{a} and \mathbf{b} of \mathbf{g} :

$$\begin{aligned} E \propto h \int [(1-\nu)|\mathbf{a} - \bar{\mathbf{a}}|^2 + \nu \text{tr}^2(\mathbf{a} - \bar{\mathbf{a}})] dS \\ + h^3 \int [(1-\nu)|\mathbf{b} - \bar{\mathbf{b}}|^2 + \nu \text{tr}^2(\mathbf{b} - \bar{\mathbf{b}})] dS. \end{aligned} \quad (2.3)$$

The first fundamental form term $\mathbf{a} - \bar{\mathbf{a}}$ contains the natural stretches λ_0 of the mid-plane of S and the second term $\mathbf{b} - \bar{\mathbf{b}}$ contains the natural curvatures κ_0 . Both λ_0 and κ_0 are visualized in Fig. 2.3 for a bilayer shell manufactured by bonded pre-stretched sheets. The expression above is based on the assumptions of classical Kirchhoff-Love plate theory [63], and an isotropic material of two bonded layers of same thickness $h/2$ and Poisson ratio ν . A comprehensive reformulation is

$$E \propto h(\text{stretching term}) + h^3(\text{bending term}). \quad (2.4)$$

The elastic energy of self-shaping is either stretching dominated, when the composite can bend but not stretch, or bending dominated when it

² For any Euclidean body under external load, the strain tensor is traditionally expressed by $\boldsymbol{\varepsilon} = \frac{1}{2}(\mathbf{C}_c - \mathbf{I})$ for example, where $\boldsymbol{\varepsilon}$ is the Green-Lagrange strain tensor derived from the right Cauchy-Green tensor $\mathbf{C}_c = \mathbf{F}^T \mathbf{F}$, with \mathbf{F} being the deformation gradient tensor derived from a measured field of displacements. Using a curvilinear coordinate representation of line elements on the body surface, $\mathbf{C}_c = \mathbf{g}$ for the case where \mathbf{g} is the metric tensor of the deformed body. This relation follows from $\mathbf{F} = \mathbf{g}_i \otimes \mathbf{G}^i$, where \mathbf{g}_i are the tangent vectors in deformed and \mathbf{G}^i are the dual basis tangent vectors in reference configuration at a given point X . See Fig. 2.2 and Ref. [62]

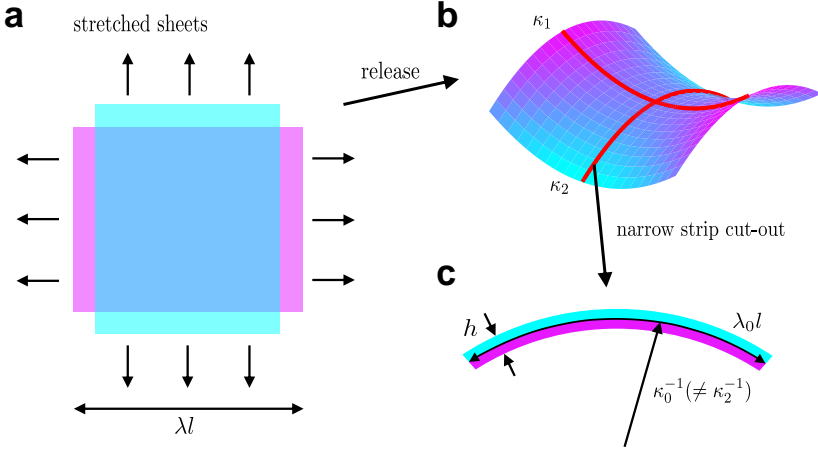


FIGURE 2.3: Shaping of stretched, bonded, and released sheets to a saddle-like surface. **a:** Imaginary isotropic sheets of initial length l are uni-axially stretched by a factor of λ . **b:** Upon release, the composite self-shapes into a saddle-like shell. **c:** A strip of infinitesimal width theoretically cut out from the saddle shell displays natural curvature κ_0 and natural stretch λ_0 of the mid-plane, which do not coincide with curvatures and stretches from the saddle configuration.

can stretch but not bend. From Eq. 2.4 it can be recognized that the transition or equilibrium between these two states is primarily influenced by the thickness h , which is seen to affect the stretching term proportionally but affects the bending term proportional to its cube. According to Gauss' *Theorema Egregium*, both fundamental forms \mathbf{a} and \mathbf{b} are coupled by the constraint that K remains constant³. In other words, one term of Eq. 2.3 and Eq. 2.4 is always dependent on the other and vice-versa. In addition, a configuration such that the system can totally minimize E by $\mathbf{a} = \bar{\mathbf{a}}$ and at the same time $\mathbf{b} = \bar{\mathbf{b}}$, is not possible. A shape configuration where E is minimized is thus characterized by a competitive balance of both terms of Eq. 2.3.

³ The Gauss equation, or Gaussian curvature, is dependent on both fundamental forms as $K = f(\mathbf{b}, \mathbf{a})$. For further information about the coupling constraints of \mathbf{a} and \mathbf{b} , see the Gauss-Codazzi-Mainardi equations, e.g. in [14].

2.4.3 Configuration-dependent shaping

Depending on the geometry of the composite, i.e. its length l , width w , and thickness h in a quasi 2D configuration, limit states of the shaping mechanism can be defined. Different final shapes of the composite arise with different choice of parameters along with varying the angles θ or ϕ (Fig. 2.4). The variation of these angles represents a parameter space of all possible combinations for arbitrary strips cut out from the two bonded sheets. The configuration-dependent shaping is shown for the case of narrow strips in Fig. 2.4. In the following, two relevant limit states depending on the geometry will be discussed, taking h and κ_0 as fixed parameters.

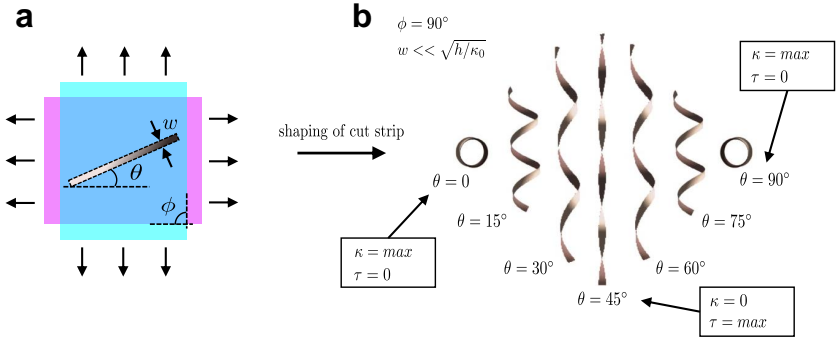


FIGURE 2.4: **Configuration-dependent shaping of narrow arbitrary bilayer strips.** **a:** Stretched and bonded sheet at an angle ϕ , with strip of width w cut out at an angle θ . **b:** Upon release, the composite strip self-shapes into the shown configurations (from [14]) in dependence of θ . Pure bending configurations maximize the curvature of the mid-plane curve, and pure twist configurations maximize the torsion of the mid-plane curve.

In the case of wide strips, such that $w \gg \sqrt{h/\kappa_0}$ (e.g. the saddle-like shell shown in Fig. 2.3), the bending term in the energy equation is minimized while the stretching term is near zero. In such a state, the resulting shapes are stretching dominated and can be characterized by parameters

of the mid-plane curve of S . The resulting curvature κ and torsion τ are given in terms of natural curvature κ_0 as

$$\begin{aligned}\kappa &= \frac{\kappa_0}{2}(1 - \nu)(\pm 1 - \cos 2\theta) \sin \phi, \\ \tau &= \frac{\kappa_0}{2}(1 - \nu) \sin 2\theta \sin \phi.\end{aligned}\tag{2.5}$$

In the case of narrow strips fulfilling the condition $w \ll \sqrt{h/\kappa_0}$ (strips as shown in Fig. 2.4), the energy is characterized by minimizing the stretching term while the bending term is near zero. Here, the resulting shape is bending dominated. In that state, the parameters of the mid-curve of the strip, κ and τ , are given by

$$\begin{aligned}\kappa &= \kappa_0 \cos 2\theta \sin \phi, \\ \tau &= \kappa_0 \sin 2\theta \sin \phi.\end{aligned}\tag{2.6}$$

The shape of any arbitrary and isotropic bi-layered composite, with induced stretch λ of one layer with respect to the other, and with parameters w , h , ϕ , θ , and κ_0 , can therefore be predicted. Armon et al. [14] show in their work the procedure to derive expressions such as in Eq. 2.5 and 2.6 starting from the general energy formulation (Eq. 2.3).

2.5 RELEVANT IMPLICATIONS FOR SELF-SHAPING WOOD

While the above presented theory and equations are valid for isotropic thin sheets, it is straightforward that they do not necessarily apply to wood, which in contrast, is an anisotropic material. Recently, updated models derived from this theory have been proposed for thin anisotropic soft matter [64]. However, bulk wood is a stiff material with complex mechanical behavior and cannot be considered a soft material. Therefore, the above presented theory is still useful, in its frame of limited validity with wood, for drawing the following fundamental conclusions:

- From the energy formulation in Eq. 2.3 it can be seen that the thickness h has a major influence whether the shaping of the composite will be stretching or bending dominated. For high values of h , the bending term will be high and the material will want to stretch in order to minimize that term. However, for self-shaping wood bilayers in wide strip configurations and cross-ply lamination ($\phi = 90^\circ$ and $\theta = 0$), an isotropic stretching will be hindered because of the stiff fiber directions of both layers. And as was shown, a change of

K inherently includes both a stretching and a bending about two in-plane axes of a plate. Therefore, changes in K for wood bilayers are favorable with very small values of h (see ⁴). Otherwise, a practicable solution is to keep $K \approx 0$ by choosing a narrow strip configuration. In such a configuration, the mid-plane needs to stretch only along a single axis and the wood strip can freely bend.

- For narrow wood bilayer strips with $\phi = 90^\circ$ and $\theta = 0$, the curvature κ is equivalent to the natural curvature κ_0 (Eq. 2.6), whose value is therefore directly predicting the self-shaping of the strip in a bending mode.

The value of κ_0 is dependent on the geometry of the narrow strip, the mechanical material parameters of the wood species, the swelling and shrinkage coefficient (for hygromorphs, λ is induced by the swelling and shrinkage strain $\varepsilon^\omega = \lambda - 1$), and the difference in moisture. These observations could be made from the analytical prediction of κ for temperature-responsive narrow bimetal strips, often referred to as the Timoshenko function [51]. This function was applied for the first time with hygromorphic structures in Ref. [39], and was then, later on, also shown valid in the case of thin wood self-shaping composites in the work of Rüggeberg and Burgert [7]. Experiments in [7] showed that, in fact, for wood bilayers $\kappa_0 \propto \Delta\omega$, where $\Delta\omega$ is the change in MC of the wood. The main impacting geometrical parameters on κ_0 were identified as both layer thicknesses h_1 and h_2 and especially, their ratio (h_1/h_2) and because of $\kappa = \varepsilon/h$, also their sum ($h_1 + h_2$). Relevant material parameters are the ratio of the axial stiffness of the layers (E_1/E_2) and the difference of swelling coefficients ($\alpha_2 - \alpha_1$) of the wood. Hereby, on a conceptual level, wood was idealized as an isotropic and linear-elastic material, and with material parameters independent of moisture. The formulation is

$$\kappa \approx \kappa_0 = \left[\frac{h_1 + h_2}{2} + \frac{2(E_1 I_1 + E_2 I_2)}{h_1 + h_2} \left(\frac{1}{E_1 h_1} + \frac{1}{E_2 h_2} \right) \right]^{-1} (\alpha_2 - \alpha_1) \Delta\omega. \quad (2.7)$$

The indices 1 and 2 refer to both layers of a bilayer composite depicted in Fig. 2.5. I_i is the second moment of area per unit width of the two bonded prismatic Euler-Bernoulli beams.

⁴ No experimental investigations or proofs on this aspect yet exist for wood self-shaping bilayers. This conclusion is drawn solely on the analysis of the physics of self-shaping presented above.

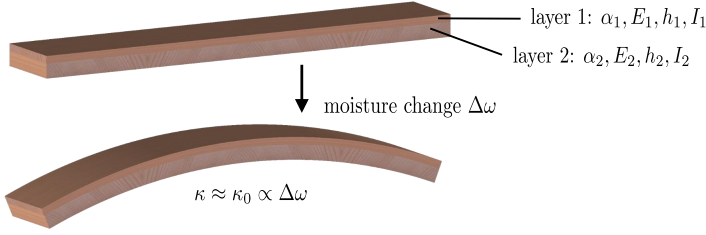


FIGURE 2.5: **Narrow wood bilayer strip.** Two bonded layers, layer 1 and layer 2, with respective parameters as in Eq. 2.7, self-shape by a change in wood MC $\Delta\omega$ to a configuration with curvature $\kappa \approx \kappa_0$.

In chapter 4, Eq. 2.7 will be further adapted to the material wood by consideration of anisotropy and moisture-dependency (explained in chapter 3), and be used for relevant investigations of implicated design principles. In chapter 5, effects of increasing h for narrow strips will be numerically investigated to incorporate complex rheological behavior and moisture gradients.

2.6 APPLICATIONS OF SELF-SHAPING WOOD COMPOSITES

Many applications of self-shaping wood bilayers were already conceptualized. Most of the previous work was of experimental nature and application-motivated concepts in the frame of architecture have mainly been the center of investigations. Examples are self-assembling wood structures and materialization, e.g. building skins in responsive architecture [65–69], autonomous shading elements [70–73], or application of wood bilayers as climate-regulated motor elements [7]. Attempts at numerical modelling have also been made [74]. A common aspect of previous work is that layer thicknesses were limited to < 10 mm and that modelling was restricted to the original Timoshenko function and to linear elastic material behavior. In contrast, the main investigations in this thesis aim at filling the gap of modelling of wood bilayers, especially in order to transgress the restriction of thin layers and to enable large-scale and industrial applications for building components.

THE MATERIAL WOOD

3.1 WOOD STRUCTURE

Wood is an excellent lightweight and biological building material. It possesses comparable specific strength as much stronger materials such as steel or reinforced concrete [75]. Nature has optimized its hierarchical structure, see Fig. 3.1, to build tall and structurally efficient trees from only very few but available elements, mainly C, O, H, and N. At every length scale, as many other biological materials, the wood structure seems to follow a specific function [22]. This is best understood by first taking a top-down approach in the hierarchy, and by considering the function and needs of the living tree. For example, the leaves of the tree crown need constant water supply in order to conduct photosynthesis. A big part of the structure's function is thus to enable sufficient water flow. Or, the trees in forests are in constant competition for light with their conspecifics, and thus need to grow tall, which implies a strong structure.

At every length scale, the structural mechanical behavior can be explained by the interplay of the different hierarchical levels below, which can be illustrated by taking a bottom-up approach. At the bottom (the molecular level (d) in Fig. 3.1), the principal wood components are the polymers cellulose, hemicelluloses, and lignin. At the cellular level (c), the microfibrils, formed by bundles of cellulose chains, represent a fibre-alike reinforcement in a matrix of amorphous hemicelluloses and lignin. This structuring results in a transverse-isotropic cell wall-layer behavior, where the angle of microfibrils with respect to the cell wall longitudinal direction, the microfibril angle, strongly influences mechanics and swelling behavior [77, 78]. At the next scale (the tissue level (b)), the alternation of latewood and earlywood results in an orthotropic mechanical behavior of the wood. Three anatomical directions, R, T, and L, illustrated in Fig. 3.3, can be identified. Here, the mechanical behavior of the strong fiber direction (L), as well as swelling and shrinkage, are still dictated by the microfibril angle. On the largest scale (the tree level (a)), a tree stem displays a transverse isotropic behavior due to the radial growth pattern of annual rings.

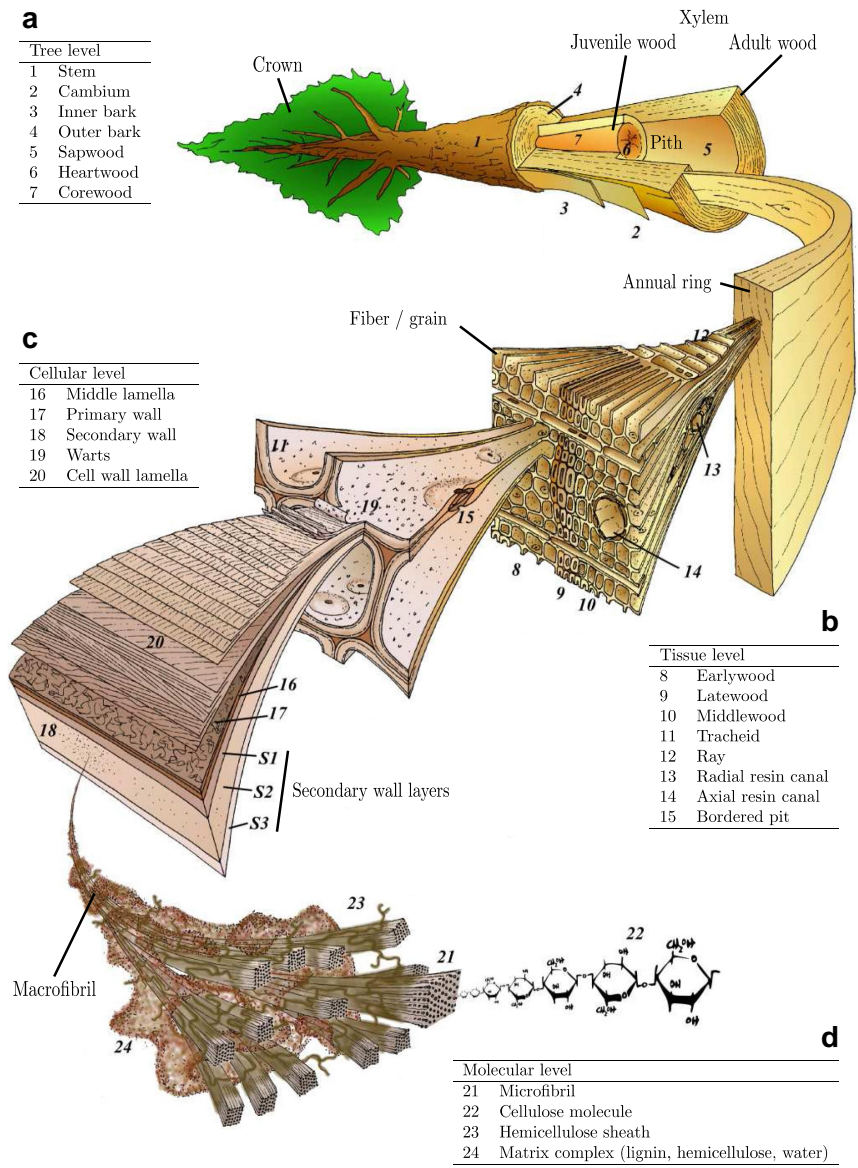


FIGURE 3.1: **Wood hierarchical structure (softwood) and terminology.** a: Macroscopic level. b: Tissue level. c: Cellular level. d: Molecular level. Adapted from [76], based on artwork from M. Harrington.

In the following, the two relevant wood species used in this work, belonging to two different classifications, softwoods and hardwoods, will be concisely described.

3.1.1 *Norway spruce*

Norway spruce (*Picea abies*) wood is one of the default construction woods used in Europe, and thus one of the economically most relevant coniferous species. It is evergreen, fast-growing, and trees typically reach a height between 30 and 55 m with a straight and slender stem of up to 1.2 m in diameter [13]. It grows mainly in Scandinavia, the Baltic region, and the mountain regions of central Europe (Fig. 3.2a). Its wood is characterized by a light color, low density, softness, low shock resistance (minor impacts cause damages), moderate stiffness, good dimensional stability in service, and low decay resistance. Its structure follows the one shown in Fig. 3.1. An overview of relevant physical properties is given in Tab. 3.1 and a texture image at the macroscopic scale is given in Fig. 3.3. In the context of this thesis and self-shaping wood, spruce is mainly of interest because of its standard processing in industry, which is necessary for large-scale curved building component applications.

3.1.2 *European Beech*

European beech (*Fagus sylvatica*) wood is a hardwood that grows all over of central Europe (Fig. 3.2b). The trees typically grow up to 30 m in height with straight stems up to 1.0 m in diameter [13]. Its wood is hard and heavy, has high bending and crushing strength, possesses a moderate to high stiffness and a high shock resistance. It is of poor dimensional stability and decay resistance, and thus very sparsely used in construction. However, it is a typical and general purpose furniture wood. Being a diffuse-porous hardwood, its tissue structure considerably differs from the one shown in Fig. 3.1. Instead of possessing tracheids, which for softwood fulfill both water transport and structural stability, hardwoods possess vessels (large pores) and mainly fibers for the respective functions. An overview of relevant physical properties is given in Tab. 3.1 and a texture image at the macroscopic scale is given in Fig. 3.3. In the context of self-shaping wood, beech is of interest thanks to its high swelling coefficients relative to other wood species, which targets towards maximizing curvature of wood bilayers.

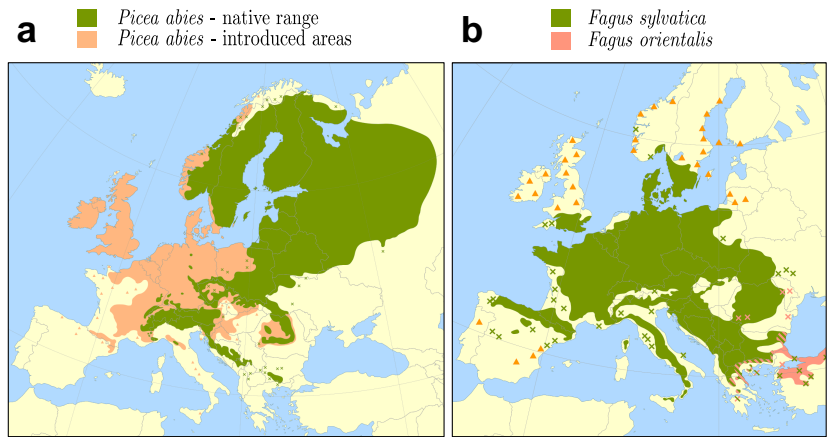


FIGURE 3.2: **Natural distribution of investigated wood species.** a: Norway spruce (*Picea abies*). b: European beech (*Fagus sylvatica*). (Figure adapted from 2017 data found in [79], crosses and triangles represent isolated populations; green: Native range; orange: Introduced areas).

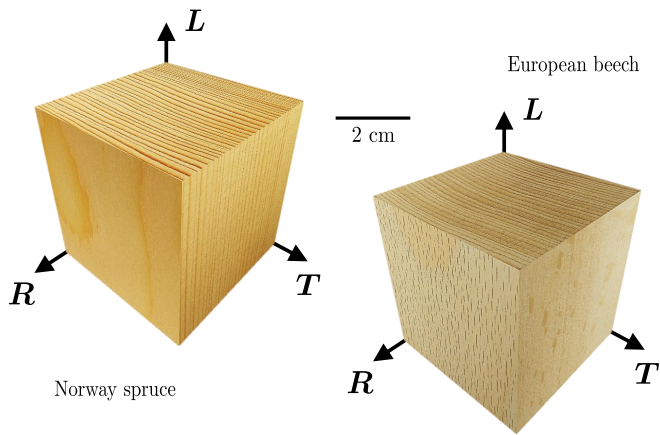


FIGURE 3.3: **Macroscopic samples with wood anatomical directions.** Radial (R), tangential (T), and longitudinal (L, grain) directions for spruce and beech samples with respective texture in each plane.

TABLE 3.1: **Selected physical properties and their natural range for Norway spruce and European beech wood.** Values found in [13] (lower bound - mean value - upper bound), and where denoted * in [80].

	Norway spruce	European beech
Polymeric composition (%)		
Cellulose	38.1 - 46.0	33.7 - 46.4
Pentosan (hemicellulose)	6.8 - 12.0	17.8 - 25.5
Lignin	19 - 29	11.6 - 22.7
Density (g cm^{-3})		
Green density	0.70 - 0.80 - 0.85	0.82 - 1.07 - 1.27
Density at 12% MC	0.33 - 0.47 - 0.68	0.54 - 0.72 - 0.91
Oven-dry density	0.30 - 0.43 - 0.64	0.49 - 0.68 - 0.88
Mechanical properties (MPa) (at 12% MC, and \parallel to the grain)		
Young's modulus	7'300 - 11'000 - 21'400	10'000 - 16'000 - 18'000
Compressive strength	33 - 50 - 79	41 - 62 - 99
Tensile strength	21 - 90 - 245	57 - 135 - 180
Bending strength	49 - 78 - 136	74 - 123 - 210
Shear strength	4.0 - 6.7 - 12.0	6.5 - 8.0 - 19.0
Brinell hardness	32	72
Differential swelling and shrinkage coefficients (%/%)		
Volumetric	0.39 - 0.40	0.46 - 0.60
Radial	0.15 - 0.19	0.19 - 0.22*
Tangential	0.27 - 0.36	0.38 - 0.44*

3.2 WOOD-WATER INTERACTION

The mechanical properties of wood (e.g. Tab. 3.1) at the scale relevant for its application as bulk structural material (Fig. 3.3) are strongly influenced by moisture. For example, by decreasing moisture content (MC) stiffness and strength tend to increase. An other important phenomenon coupled to the wood MC are the dimensional changes by swelling or shrinkage. Therefore, moisture can be seen as a state variable of high interest. Hereafter, the main principles of wood-water interaction will be concisely explained.

3.2.1 *Water in the cell wall*

The wood cell, composed of wall and lumen, is a practical representative scale for explanation of the water state in macroscopic wood. Here, the MC or water content, denoted ω can be separated in free and bound water depending on environmental conditions. The different states of water in the wood cell are represented in Fig. 3.4. In the living tree, the wood cell lumen is used for water transport and is thus always filled by water, called free water. In this state, referred to as green state, ω is composed of the amount of free water and the maximal amount of water bound in the cell wall per unit of dry cell wall mass. The gravimetric method to determine the MC is by using $\omega = (m - m_0)m_0^{-1}$ where m is the wet and m_0 is the dry mass. In the wet (or over-hygroscopic [81]) range, ω is typically above 30-35%, which approximately ($\pm 5\%$) represents the fiber saturation point (FSP) for most wood species. The exact FSP is of theoretical nature and defined as the point where there is no more free water in the lumen but where the cell wall is still fully water saturated. If the partial water vapor pressure p/p_0 (in terms of percentage, the relative air humidity) in the lumen is < 1 , then the cell wall enters the hygroscopic range. Here, ω is linked to the environment conditions (p/p_0 and temperature T) by the sorption isotherm.

3.2.2 *The sorption isotherm*

Below the fiber saturation point the amount of water in wood is dictated by the number of water molecules present in the wood cell wall. This quantity can be experimentally determined in dependence of p/p_0 at a given T and is called the sorption isotherm [82]. Reciprocally, but of lower relevance, the sorption isobar is determined in dependence of T at a given p/p_0 . A

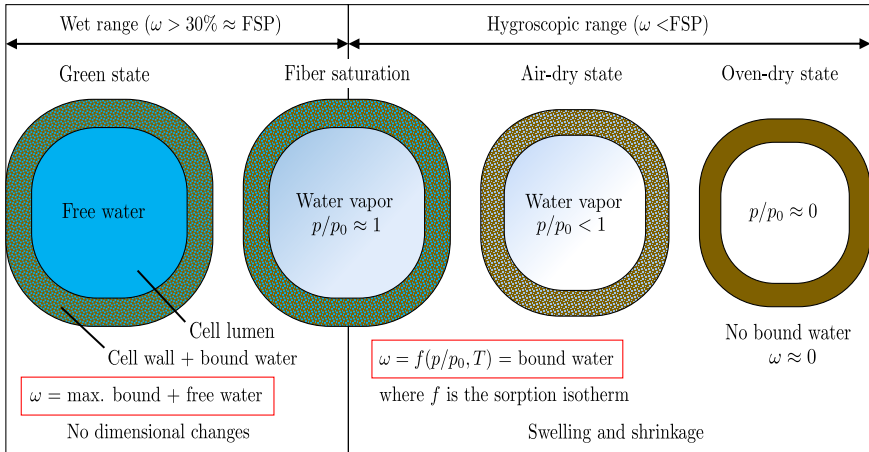


FIGURE 3.4: **Illustration of the states of water in the wood cell.** From left to right: Wet to dry.

typical representation of sorption isotherm for Norway spruce, measured by a dynamic vapor sorption device at $T = 25^\circ\text{C}$, is given in Fig. 3.5. The isotherm displays hysteresis and can generally be divided into three distinct parts: The desorption curve from water saturated state [83], the adsorption curve starting at the dry state, and the scanning desorption curve starting the drying process at any given state reached in adsorption. Therefore, sorption history has to be taken into account when ω is not directly determined by the gravimetric method.

Although thoroughly investigated, the sorption mechanisms of lignocellulosic materials such as wood are still largely hypothetical [84–89]. A realistic scenario based on the current knowledge of type IV sorption isotherms [90] is as follows: Upon drying from the FSP, larger clusters of water molecules first evaporate from pores and capillaries at the nanoscale formed by voids in the wood cell wall and middle-lamella. And by further drying, water molecules bound on the local functional hydroxyl (OH) groups of the cell wall polymers then evaporate. Hereby, the localized H-bonding to the polymers is close to a pure physisorption mechanism. A sound explanation of the apparent sorption hysteresis between desorption and adsorption branches is yet missing [91–93].

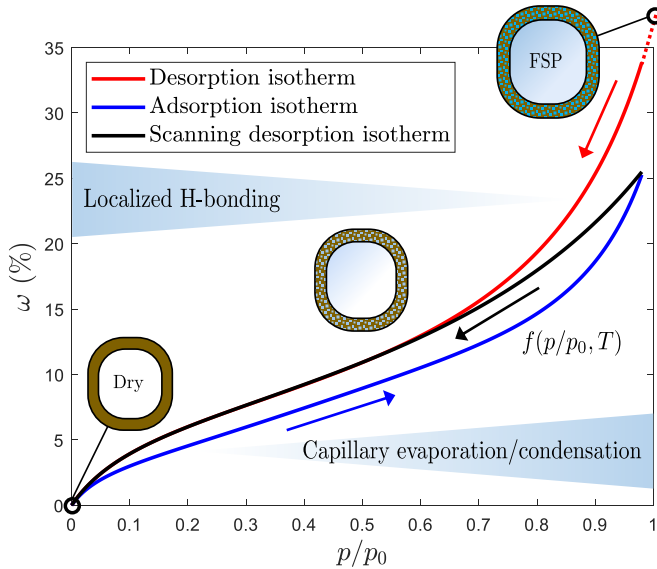


FIGURE 3.5: **Norway spruce earlywood sorption isotherm at $T = 25^{\circ}\text{C}$.** Sorption history: Start at water saturated state and drying to $p/p_0 = 0$ (red desorption curve), re-wetting until $p/p_0 = 0.98$ (blue adsorption curve), and drying to $p/p_0 = 0$ (black scanning desorption curve). Sorption mechanisms: At lower p/p_0 : Localized H-bonding of water molecules onto OH groups of polymers (physisorption-alike). At higher p/p_0 : Capillary evaporation and condensation in voids of the cell wall and middle lamella ($2 < r < 50$ nm). Sorption data from [94].

3.2.3 Swelling and shrinkage

In the hygroscopic range, water molecules adsorbing on the polymer functional groups by H-bonding decrease the Van der Waals interactions and break existing H-bonds between the polymers, and thus act as repellent. This mechanisms results in expansion, and at the same time, structural weakening of the polymer network in the cell wall. At the macroscopic level wood swells and shrinks by different amounts in different anatomical directions. The origin lies in the cellular geometry and the early- and latewood alternation. The anisotropic shrinkage can be visualized by considering different green-state cuts of subsequently dried boards from a

stem as shown in Fig. 3.6. In a single anatomical direction, the swelling and shrinkage strain calculates as

$$\varepsilon^\omega = \int_{\Omega} \alpha d\omega, \quad \text{where } \Omega \subset [0, \text{FSP}(\%)] \quad (3.1)$$

Here, α is the differential swelling or shrinkage coefficient in units of $\%^{-1}$ and ω is the wood MC in %. The symbol Ω denotes a domain below the FSP. Reciprocally, the swelling coefficient can be experimentally determined by $\alpha = \varepsilon^\omega \Delta\omega^{-1}$ if a domain of linear swelling and shrinkage in function of ω is assumed. Previous works concluded that this is the case below a MC of approximately 20% [95–97]. For the three wood anatomical directions R, T, and L, and in Voigt matrix notation, the relation reads

$$\varepsilon^\omega = \alpha \Delta\omega, \quad \text{with } \alpha = (\alpha_R, \alpha_T, \alpha_L, 0, 0, 0), \quad (3.2)$$

where ε^ω is a second-order swelling strain tensor and α is a diagonal second-order tensor mapping from the change in moisture $\Delta\omega$.

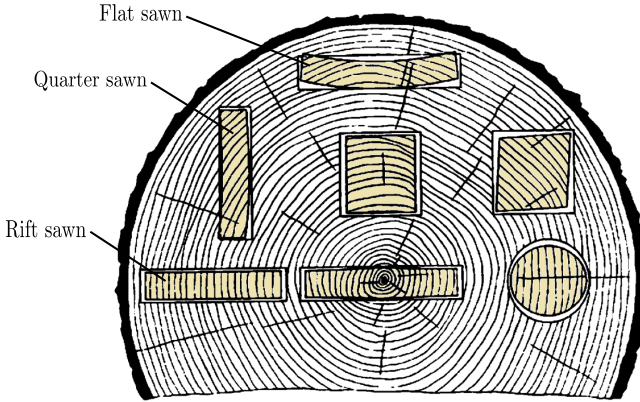


FIGURE 3.6: **Drying-induced deformations of different board cuts originating from shrinkage-anisotropy.** Material waste: Flat < quarter < rift. Board quality: Flat < quarter < rift. Graphic modified from [98]. (Notice: Quarter and rift terminology is often interchanged in literature, the author judges this one to be accurate)

3.3 MECHANICAL BEHAVIOR

As previously stated, the mechanical behavior of wood at the macroscopic scale is a consequence of its hierarchical structuring and its polymeric composition. This has the main effect that the mechanical parameters are strongly influenced by state variables such as moisture or temperature. In addition, due to its biological growth origin affecting material structuring, different xylem types such as e.g. sapwood and heartwood, juvenile and adult wood, tension wood (hardwoods) or compression wood (softwoods), early or latewood, display significantly different mechanical behaviors. These types tend to mix and to average out in typical macroscopic wood samples used to determine mechanical parameters (e.g., see [99, 100]), and therefore, contribute to their typical high variability. Hereby, important structural factors influencing mechanics of the different xylem types are the microfibril angle and the wood's density [101].

Wood displays at the macroscopic scale different phenomenological and coupled deformation mechanisms, which have to be taken into account and carefully separated from one-another in order to determine mechanical material parameters. These mainly depend on velocity and level of loading, changes in state variables while loading, and direction of loading as wood is an anisotropic material with a strong and stiff fiber direction (L) but much more compliant and weak transverse directions (R and T). Furthermore, tension and compression asymmetries exist and have to be accounted for in the mechanical behavior of wood [102]. A recent integral reference work is given in [103]. In the following, an overview of individual relevant deformation mechanisms in wood will be given.

- **Elasticity:** For wood samples loaded with high velocity and up to moderate load levels, the material behavior can be observed to be approximately linear-elastic. Hereby, different stiffnesses manifest for the different anatomical wood directions R , T , and L . In fact, wood can be considered as an orthotropic material if curvature in annual rings of the samples is small. Therefore, wood possesses a 4th order stiffness tensor of orthotropic type, i.e. with 12 non-zero entries and 9 independent material parameters such as shown in chapter 4 in Eq. 4.1 (these are plotted in Fig. 4.1 for beech in dependence of ω). For both species spruce and beech, the inverse stiffness matrix is visualized in dependence of R , T , and L in Fig. 3.7 with so-called elastic deformation bodies [104], at normal climate (20°C and 65% RH).

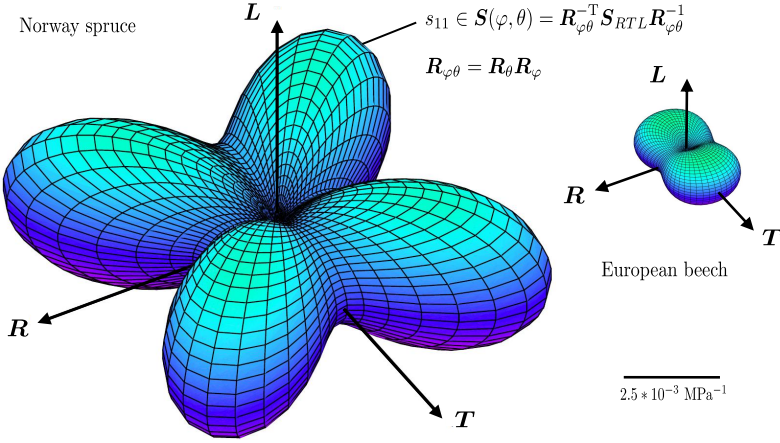


FIGURE 3.7: **Elastic deformation body (compliance) for Norway spruce and European beech under uniaxial loading.** 3D representation of the inverse elastic stiffness tensor $S = C^{-1}$ at normal climate where the diagonal element s_{11} is plotted in function of a rotation of the tensor by two angles φ and θ (polar coordinates). The matrix S (in Voigt notation) can be rotated by two 6×6 rotation matrices R_φ and R_θ (quaternion-derived). For Norway spruce, the effect of rolling shear (contained in S) is impressively visualized at 45° between the R and T directions. Figure modified from [105] and [106].

- **Plasticity:** Upon fast loading up to high load levels, wood displays plastic deformations. These irreversible deformations happen, in dependence of type of loading (tensile, compressive, bending, or shear) after a typical strength or yield value is surpassed. Due to the anisotropic nature, a multitude of behaviors such as brittle fracture (e.g. in tension), strain softening (e.g. compression in L -direction), or strain hardening (e.g. compression in R -direction) can be observed.
- **Visco-elasticity:** Under slow ramping or under sustained load, wood creeps as a consequence of its polymeric nature. This type of deformation is difficult to fully separate from pure elasticity as already under fast strain-controlled loading, stress relaxation can be observed. Creep in wood manifests in dependence of loading level with the three classical known phases of primary, secondary, and tertiary creep, until creep failure. Hereby, visco-elasticity, i.e. reversible creep de-

formations over time, is a mechanism mostly used to describe the primary creep phase, as for higher loadings, visco-plasticity can be observed.

- **Mechano-sorption:** Regardless of the level or the velocity of loading, if the MC is changed simultaneously while a load is being applied, wood displays an additional deformation mechanism called mechano-sorption. This mechanism can theoretically be separated from the others, but this still represents a great challenge in today's experimental wood mechanics. The difficulty is to accurately separate swelling and shrinkage strains and the effect of moisture dependency in all other parameters of simultaneously happening mechanisms. Mechano-sorptive behavior remains up to date, even for the well-studied species spruce or beech, vastly uncharacterized [11].

3.4 WOOD COMPUTATIONAL MECHANICS

Owning to the relevance of timber in construction, wood computational mechanics have a vast tradition over the past decades; for a recent review, readers are referred to [107–109]. Within the frame of the Finite Element Method (FEM) [110], today's standard computational mechanical method in engineering, constitutive material models reflecting the mechanical material behavior need to be defined in order to make a relation between deformation and loading. Experimental characterization of wood material properties¹, under the specific considerations mentioned above, have led to the development of complex material models for accurate simulation of the wood material behavior. For wood at the clear-wood scale (approx. 10 mm - 10 cm), these models are often based on a rheological approach [118], taking into account the time- and moisture-dependent behavior. Currently, a handful such models have been developed, e.g. [119], [120] or [11, 121]. In the following, the rheological material model presented in Hassani et al. [11] will be concisely outlined (without details on numerical implementation). This model uniquely couples the aforementioned deformation mechanisms, including hygro-expansion, and is implemented in an FE-framework with a fully moisture- and time-dependent formulation. The

¹ E.g., for experimental characterization of European beech mechanical properties see references [111–117].

Helmholtz free energy function Ψ , characterizing the constitutive material model, is defined as

$$\Psi = \frac{1}{2} \boldsymbol{\varepsilon}^{el} \mathbf{C}^{el} \boldsymbol{\varepsilon}^{el} + \frac{1}{2} \sum_{i=1}^n \varepsilon_i^{ve} \mathbf{C}_i^{ve} \varepsilon_i^{ve} + \frac{1}{2} \sum_{j=1}^m \varepsilon_j^{ms} \mathbf{C}_j^{ms} \varepsilon_j^{ms} + \frac{1}{2} \sum_{l=1}^r q_l \alpha_l. \quad (3.3)$$

The stress tensor $\boldsymbol{\sigma}$ acting on a material point is in constitutive relation to the total strain tensor $\boldsymbol{\varepsilon}^{tot}$ by $\boldsymbol{\sigma} = \partial \Psi / \partial \boldsymbol{\varepsilon}^{tot}$, where $\boldsymbol{\varepsilon}^{tot}$ decomposes additively, in the frame of an infinitesimal strain theory, as

$$\boldsymbol{\varepsilon}^{tot} = \boldsymbol{\varepsilon}^{el} + \boldsymbol{\varepsilon}^{pl} + \boldsymbol{\varepsilon}^{\omega} + \sum_{i=1}^n \varepsilon_i^{ve} + \sum_{j=1}^m \varepsilon_j^{ms}. \quad (3.4)$$

\mathbf{C} hereby represents the respective tensors containing the material parameters. The superscripts *el*, *pl*, *ve*, and *ms* stand for the elastic, plastic, visco-elastic, and mechano-sorptive deformations. The last term in Eq. 3.3 stands for the isotropic hardening energy upon irrecoverable plastic deformations. The constitutive material model can be visualized by a series of rheological elements such as in Fig. 5.2 from chapter 5. The swelling strain tensor component $\boldsymbol{\varepsilon}^{\omega}$, containing the swelling coefficients, does not enter Ψ , i.e. it is independent on the acting stress, and was described above in Eq. 3.2. The remaining wood material properties² enter the computational model as follows:

- **Elasticity:** The elastic stiffness tensor calculates as $\mathbf{C}^{el} = (\mathbf{S}^{el})^{-1}$ with \mathbf{S}^{el} as shown in Eq. 4.1 of chapter 4 containing the moisture-dependent elastic properties $P_i = f(\omega)$. Here, P_i stands for the orthotropic engineering constants, i.e. three Young's moduli, three shear moduli, and three (out of six) Poisson ratios, which are dependent on ω .
- **Plasticity:** The model makes use of a multi-surface plasticity model (C0 continuity) and consists of three independent failure mechanisms in compression along the wood anatomical directions R, T, L . In 3D stress space

$$f_l(\boldsymbol{\sigma}, \alpha_l, \omega) = \mathbf{a}_l \boldsymbol{\sigma} + \boldsymbol{\sigma} \mathbf{b}_l \boldsymbol{\sigma} + q_l(\alpha_l, \omega) - 1 \quad (3.5)$$

² All wood material parameters described in the following can be found in the appendix of [11]. Especially, the parameters for Norway spruce and European beech are given as a function of MC ω .

represent the respective yield functions for $l = R, T, L$. With q_l the plastic hardening functions, α_l the internal hardening variables, and \mathbf{a}_l and \mathbf{b}_l the tensors containing the moisture-dependent strength values. The moisture-dependent hardening functions are calculated using modified Ramberg-Osgood functions as

$$q_l(\alpha_l, \omega) = (\beta_{0l}\omega + \beta_{1l})(1 - e^{-\beta_{2l}\alpha_l}) / f_{c,l}(\omega). \quad (3.6)$$

The scalar values β_{0l} , β_{1l} and β_{2l} are experimentally determined material parameters and $f_{c,l}(\omega)$ are the compressive strengths, which normalize $q_l(\alpha_l, \omega)$ for consistency with Eq. 3.5. The associated flow rules, describing the constitutive relation of plastic deformations are given by

$$\dot{\epsilon}^{pl} = \sum_{l=1}^r \dot{\gamma}^l \partial_{\sigma} f_l(\sigma, \alpha_l, \omega) = \sum_{l=1}^r \dot{\gamma}^l (\mathbf{a}_l + 2\mathbf{b}_l \sigma), \quad (3.7)$$

where r denotes number of active yield mechanisms. And in similar manner, the evolution equation for the hardening law is

$$\dot{\alpha} = \sum_{l=1}^r \dot{\gamma}^l \partial_{\alpha} f_l(\sigma, \alpha_l, \omega) = \sum_{l=1}^r \dot{\gamma}^l. \quad (3.8)$$

In the above expressions $\dot{\gamma}^l$ represent consistency parameters subject to Karush-Kuhn-Tucker consistency conditions.

- **Visco-elasticity:** Recoverable creep deformations are modelled using a serial combination of $n = 4$ Kelvin-Voigt rheological elements, i.e. with 4 visco-elastic material tensors \mathbf{C}_i^{ve} . The visco-elastic strain-rate $\dot{\epsilon}_i^{ve}$ is described as linear function of the visco-elastic driving stress $\sigma_i^{ve} = \sigma - \mathbf{C}_i^{ve} \epsilon_i^{ve}$ as

$$\dot{\epsilon}_i^{ve} = \frac{1}{\tau_i} \mathbf{C}_i^{-1} \sigma_i^{ve}, \quad (3.9)$$

and the governing rate equation is

$$\dot{\epsilon}_i^{ve} + \frac{1}{\tau_i} \epsilon_i^{ve} = \frac{1}{\tau_i} \mathbf{C}_i^{-1} \sigma(t). \quad (3.10)$$

Here, τ_i denotes the characteristic retardation time for the i^{th} Kelvin-Voigt element. The components of the single entries of the visco-

elastic compliance tensors C_i^{-1} (see ³) calculate in dependence of ω as

$$J_{iL}^{ve} = (J_{i1}\omega + J_{i0})(1 - e^{-t/\tau_i}), \quad (3.11)$$

where J_{i1} and J_{i0} are the material parameters. The visco-elastic strains of the i^{th} Kelvin-Voigt element can now be computed by integration of Eq. 3.10 with

$$\begin{aligned} \epsilon_{i,n+1}^{ve} &= \epsilon_{i,n}^{ve} \exp\left(-\frac{\Delta t}{\tau_i}\right) \\ &+ \int_{t_n}^{t_{n+1}} \frac{C_i^{-1}\sigma(t)}{\tau_i} \exp\left(-\frac{t_{n+1}-t}{\tau_i}\right) dt. \end{aligned} \quad (3.12)$$

The above expression is valid for stress-driven problems with time increments $\Delta t = t_{n+1} - t_n$ and strain tensors $\epsilon_{i,n+1}^{ve}$, $\epsilon_{i,n}^{ve}$ at the times t_{n+1} and t_n .

- **Mechano-sorption:** The formulation of mechano-sorption follows the one for creep deformations shown above. A serial combination of $m = 3$ Kelvin-Voigt rheological elements with 3 mechano-sorptive material tensors C_j^{ms} is used. Here, the driving stress is formulated as $\sigma_j^{ms} = \sigma - C_j \epsilon_j^{ms}$, and the reciprocal strain-rate is defined as

$$\dot{\epsilon}_j^{ms} = \frac{|\dot{\omega}|}{\mu_j} C_j^{-1} \sigma_j^{ms}. \quad (3.13)$$

Here, μ_j stands for the characteristic moisture, which is analogous to τ_i . As before, for a single Kelvin-Voigt element

$$\dot{\epsilon}_j^{ms} + \frac{|\dot{\omega}|}{\mu_j} \epsilon_j^{ms} = \frac{|\dot{\omega}|}{\mu_j} C_j^{-1} \sigma(t), \quad (3.14)$$

and

$$\begin{aligned} \epsilon_{j,n+1}^{ms} &= \epsilon_{j,n}^{ms} \exp\left(-\frac{|\Delta\omega|}{\mu_j}\right) \\ &+ \int_{\omega_n}^{\omega_{n+1}} \frac{C_j^{-1}\sigma(t)}{\mu_j} \exp\left(-\frac{|\omega_{n+1}-\omega(t)|}{\mu_j}\right) d|\omega(t)|. \end{aligned} \quad (3.15)$$

³ Note that for the species spruce and beech, multiple of such entries, i.e. material parameters, are still missing because of lack of experimental characterization. A common procedure applied for the missing parameters is to scale known parameters by assumption of arbitrary proportionalities, e.g. by the degree of anisotropy in the elastic properties, or by density if the parameters originate from another wood species.

Instead of a time increment, a moisture increment with absolute value $|\Delta\omega| = |\omega_{n+1} - \omega_n|$ is used. The mechano-sorptive strains at times t_{n+1} and t_n are represented with $\varepsilon_{j,n+1}^{ms}$ and $\varepsilon_{j,n}^{ms}$.

As mentioned above, the presented constitutive material relations can be used at the macroscopic (clear-wood) scale exclusively and are therefore valid for defect-free wood samples as shown in Fig. 3.3, which showcases the typical representative elementary volume (REV). Therefore, the model is perfectly suited for studying self-shaping wood composites with thicknesses ranging from the mm to the cm scale, and which undergo complex moisture diffusion processes as a function of time.

In general, the wider field of computational wood mechanics involves multiple scales where each wood REV possesses a different structure and mechanical behavior. The typical order of scales is: The molecular scale of wood polymers [89], the cell wall tissue scale [108, 122], the cellular or growth-ring scale [123, 124], the clear wood scale [107, 118–120], the board scale [109, 125, 126], and finally the building scale used for design of timber structures. While the FEM (or variants, e.g. XFEM) are applied at most of the scales, some other often used methods include molecular dynamics, the material point method, or additional stochastic modelling. However, in order to gain fundamental understanding of phenomenological mechanisms happening in wood at the next larger scale, often bottom-up multi-scale approaches are used [124, 127–131]. Such approaches can be used e.g. for inverse material parameter fitting across scales.

MODELING AND DESIGN OF THIN BENDING WOODEN BILAYERS

4.1 PUBLICATION PREAMBLE

Modeling and design of thin bending wooden bilayers

Philippe Grönquist^{1,2}, Falk K. Wittel², Markus Rüggeberg^{1,2}

¹ Empa, Applied Wood Materials, 8600 Dübendorf, Switzerland

² ETH Zurich, Institute for Building Materials, 8093 Zürich, Switzerland

Journal: PloS ONE 13(10)

Submitted: 13 July 2018

Published online: 16 October 2018

DOI: <https://doi.org/10.1371/journal.pone.0205607>

Author contributions: Conceptualization: PG, FKW, MR. Data curation: PG, MR. Formal analysis: PG. Funding acquisition: MR. Investigation: PG. Methodology: PG. Project administration: PG, MR. Resources: MR. Software: PG. Supervision: FKW, MR. Validation: PG. Visualization: PG. Writing - original draft: PG. Writing - review & editing: PG, FKW, MR.

Key findings

- Wood-adapted simple analytical model is derived for prediction of natural curvature of narrow bilayer strips after moisture changes.
- Elastic energy and axial stresses are found to be minimized for a given ratio of the two layer thicknesses of the bilayer.
- Residual axial stresses of the deformed bilayer after self-shaping are independent of the sum of the single layer-thicknesses of the bilayer.

Abstract

In recent architectural research, thin wooden bilayer laminates capable of self-actuation in response to humidity changes have been proposed as sustainable, programmed, and fully autonomous elements for facades or roofs for shading and climate regulation. Switches, humidistats, or motor elements represent further promising applications. Proper wood-adapted prediction models for actuation, however, are still missing. Here, a simple model that can predict bending deformation as a function of moisture content change, wood material parameters, and geometry is presented. We consider material anisotropy and moisture-dependency of elastic mechanical parameters. The model is validated using experimental data collected on bilayers made out of European beech wood. Furthermore, we present essential design aspects in view of facilitated industrial applications. Layer thickness, thickness-ratio, and growth ring angle of the wood in single layers are assessed by their effect on curvature, stored elastic energy, and generated axial stress. A sensitivity analysis is conducted to identify primary curvature-impacting model input parameters.

4.2 INTRODUCTION

Wood, as a sustainable and natural-grown fiber composite material, has been used over many centuries as mankind's research on wood and wood-based products has enabled countless applications. More recently, novel and innovative concepts for application as self-actuation-capable, humidity-responsive structures have arisen in applied research for biomimetic architecture [7, 43, 48, 66–69, 71]. Bi-layered wooden structures, capable of complex and extensive shape changes in function of a given geometrical setup and change in ambient climate have been envisaged for diverse uses including shading elements [71], climate-adaptive facades [65], or motor elements [7]. The promising and sustainable principle found its inspirations in nature where anisotropic biological materials with inherent bi-layered and differential fiber structure use humidity changes to generate movement [14, 37, 39].

Transferring such innovative concepts to industrial production standards with essential economic benefits requires high reliability of the performance of the elements according to given design and specific application. Next to this, the accurate prediction of actuation as a function of geometry and climate change is crucial. A model was derived by Timoshenko [51] for predicting bending of thin bi-metal strips as a function of temperature change. This concept has recently been applied to the material wood as a linear-elastic prediction of thin bending wooden bilayers [7]. However, the consideration of the essential physical characteristics of the material wood for such simple models is missing. Wood, a biological, anisotropic and hygroscopic material shows a strong moisture-dependency of its material parameters that should be incorporated when modeling its mechanical behavior [11, 115]. Furthermore, as a consequence of orthotropic material behavior, wood should not be treated as isotropic when reduced to two dimensions (2D) for modeling.

We present a simple, wood-adapted, 2D linear-elastic model for predicting curvature for a given moisture content change of thin bending bilayers, based on Refs. [7, 51]. The model is validated using experimental data collected on cross-grained bilayers made out of European beech wood. Using the model, we assess geometrical design aspects such as thicknesses, thickness-ratio, or growth ring angle of the wood in single layers in function of available climate and wood species. These insights help in avoiding potential secondary problems such as adhesive-bond delamination or increased deformation prediction errors. Furthermore, we analyze the ef-

fects of these parameters on resulting curvature, stored elastic energy, and maximum axial elastic stresses. Important dimensioning characteristics are suggested in view of optimized structures for industrial application.

High variability in material parameters, a natural characteristic inherent to wood [132], in combination with fabrication tolerances resulting from wood-processing, affecting bilayer geometry, may considerably influence resulting deformation magnitude and thus the precision of the model. To assess these uncertainties, we make use of total Sobol' indices [133] for a sensitivity analysis on each model input parameter. Through partial variances, the impact of variability in each input parameter on the variability of the model output, i.e., bilayer curvature, can be quantified. Critical parameters can be identified and separated from less important ones in view of efficient in-situ sample measurements and model parameter-updating for facilitated industrial processes.

4.3 THEORY

Elastic properties of European beech

Considering Hooke's law in three dimensional Euclidean space $\sigma = \mathbf{C}\epsilon$, a strain state ($\epsilon = \epsilon_{kl}\mathbf{e}_k \otimes \mathbf{e}_l$) is mapped onto a stress state ($\sigma = \sigma_{ij}\mathbf{e}_i \otimes \mathbf{e}_j$) by a 4th-order stiffness tensor \mathbf{C} ($\mathbf{C} = C_{ijkl}\mathbf{e}_i \otimes \mathbf{e}_j \otimes \mathbf{e}_k \otimes \mathbf{e}_l$). The compliance tensor \mathbf{S} ($\mathbf{S} = \mathbf{C}^{-1}$), for an orthotropic material such as wood, is expressed in terms of the engineering constants (w.r.t a basis $\mathbf{e}_1, \mathbf{e}_2, \mathbf{e}_3$) and in Voigt-notation as

$$\mathbf{S} = \begin{bmatrix} E_1^{-1} & -\nu_{21}E_2^{-1} & -\nu_{31}E_3^{-1} & 0 & 0 & 0 \\ -\nu_{12}E_1^{-1} & E_2^{-1} & -\nu_{32}E_3^{-1} & 0 & 0 & 0 \\ -\nu_{13}E_1^{-1} & -\nu_{23}E_2^{-1} & E_3^{-1} & 0 & 0 & 0 \\ 0 & 0 & 0 & G_{23}^{-1} & 0 & 0 \\ 0 & 0 & 0 & 0 & G_{31}^{-1} & 0 \\ 0 & 0 & 0 & 0 & 0 & G_{12}^{-1} \end{bmatrix} \quad (4.1)$$

where E_i (Young's moduli), G_{ij} (shear moduli), and ν_{ij} (Poisson's ratios) can be collected from mechanical characterization experiments. In the case of wood, the local anatomical growth directions L , T , and R (Longitudinal or grain direction, tangential, and radial direction) can be assigned in arbitrary order to the basis $\mathbf{e}_1, \mathbf{e}_2, \mathbf{e}_3$. Hereby, the representative elementary vol-

ume is considered far away from the pith, i.e., the growth-ring-curvature is neglected. Elastic material properties have been collected for the hardwood species European beech (*Fagus sylvatica* L.), in L , R , and T directions as functions of wood moisture content ω in Ref [115]. A linear dependence on ω is assumed for the species beech as $P_i = b_0 + b_1\omega$, where P_i stands for the i^{th} property P that represent the engineering constants, and b_0 and b_1 are coefficients found in Ref [11]. Fig 4.1 shows P_i in terms of ω as they are used in the present study.

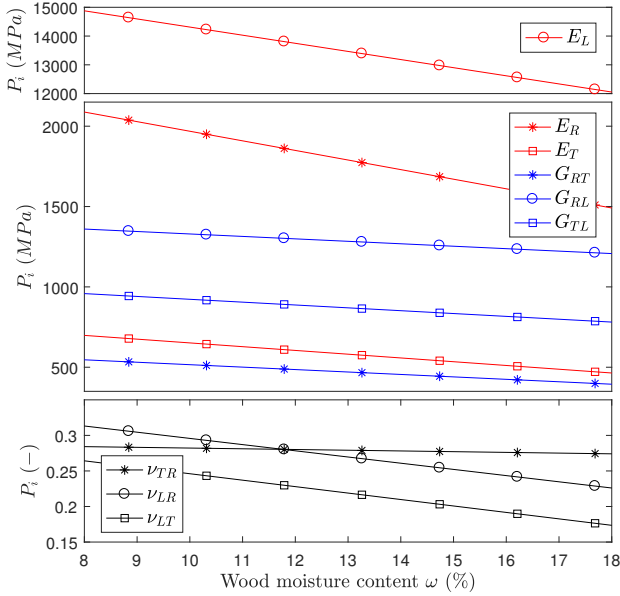


FIGURE 4.1: **Elastic properties for European beech.** Properties P_i as function of moisture ω as found in Refs [115] and [11]. The moisture interval [8%, 18%] roughly corresponds to a relative humidity range of [35%, 85%] (adsorption at 85% and desorption at 35%).

2D linear elastic model for wooden bilayer curvature

The 3D elastic material law $\varepsilon = \mathbf{S}\sigma$ with \mathbf{S} as described in Eq (4.1) is hereafter reduced to 2D by assuming (i) a plane strain state, and alternatively, (ii) a plane stress state. A 2D schematic of a wooden bilayer is represented

in Fig 4.2, where the undeformed state (with initial wood moisture content ω_0) is shown along a deformed state (curvature κ , wood moisture content $\omega_1 < \omega_0$, for drying). Typically, the wood is oriented such that in layer 1, L aligns with \mathbf{e}_x and in layer 2 R aligns with \mathbf{e}_x and T with \mathbf{e}_y . This results in a stiff and resisting layer 1 (called "passive" layer, very low swelling in L direction) to block axial deformation at the interface (an adhesive bond) coming from the driving layer 2 (the "active" layer, high swelling and shrinkage in R - or T -direction). For the resulting curvature κ of a 2D model, the stiffnesses $Q_{i,x}$ in direction of \mathbf{e}_x of each layer ($i = 1, 2$) are of interest. For cases (i) and (ii), and using the same basis as for Eq 4.1, they are derived as

$$Q_{i,x}^{(i)} = \frac{E_1}{1 - \nu_{13}\nu_{31}}, \quad Q_{i,x}^{(ii)} = \frac{E_1 - \nu_{12}^2 E_2}{1 - \nu_{12}\nu_{21}}, \quad (4.2)$$

assuming a uni-axial stress state $\sigma^{(2D)} = (\sigma_x, 0, 0)^T$ to act on the bilayer.

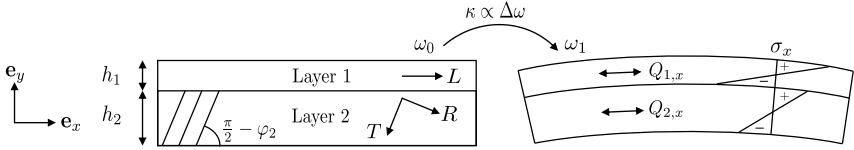


FIGURE 4.2: **2D schematic of wooden bilayer.** Initial flat (wet, ω_0) and resulting deformed state (dry, ω_1) after drying ($\omega_0 > \omega_1$). Global 2D coordinate system (basis $\mathbf{e}_x, \mathbf{e}_y$) and local anatomical directions (R, T, L) for layers 1 and 2 with growth ring inclination φ_2 of layer 2. Passive layer (layer 1) with thickness h_1 and active layer (layer 2) with thickness h_2 . Stiffnesses $Q_{i,x}$ in \mathbf{e}_x -direction of layer i and axial stress distribution σ_x over cross-section.

The curvature for a cross-grained wooden bilayer structure is a function of the applied difference in moisture content. Existing models assume a direct proportionality $\kappa \propto \Delta\omega$ [7]. The presumed proportionality factor (referred to as K) is, in the case of wood, not constant but is itself a function of moisture ($K = K(\omega)$). For any bilayer configuration, K contains the effects of geometry and material parameters and is obtained by formulating equilibrium, compatibility, and a deformation equilibrium at the interface

of two bonded Euler-Bernoulli beams [51]. In terms of Eqs 4.2 and considering the basis $\mathbf{e}_x, \mathbf{e}_y$ in Fig 4.2, the term is derived as

$$K = \left[\frac{h_1 + h_2}{2} + \frac{2(Q_{1,x}I_1 + Q_{2,x}I_2)}{h_1 + h_2} \left(\frac{1}{Q_{1,x}h_1} + \frac{1}{Q_{2,x}h_2} \right) \right]^{-1} (\alpha_{2,x} - \alpha_{1,x}) \quad (4.3)$$

where $I_1 = h_1^3/12$ and $I_2 = h_2^3/12$ are the second moments of area per unit width of bilayer-strip. h_1 and h_2 denote layer thicknesses and $\alpha_{1,x}$ and $\alpha_{2,x}$ are the differential swelling coefficients in bilayer axial direction (\mathbf{e}_x) such that $\alpha = \varepsilon^\omega \Delta\omega^{-1}$ where ε^ω is the swelling strain. For beech wood, typical values used are $\alpha_L = 0.0001$, $\alpha_R = 0.0019$, and $\alpha_T = 0.0040$ in $\%^{-1}$ [11]. Here, we assume α as remaining constant over Ω , otherwise, the swelling strain would read $\varepsilon^\omega = \int_\Omega \alpha d\omega$. Ω stands for a moisture domain such that for beech wood $\Omega \subset [0, FSP(\%)]$ contains all possible states of ω where FSP denotes the fiber saturation point. For any moisture increment $\Delta\omega \in \Omega$, the change in layer-thickness (direction \mathbf{e}_y) of layer i can thus be calculated as $\Delta h_i = h_i \alpha_{i,y} \Delta\omega$, and added (swelling) or subtracted (shrinkage) to the actual layer thicknesses. Next to updating thicknesses and mechanical parameters over changes of $\omega \in \Omega$, the growth ring inclination φ , considered only in layer 2 as φ_2 (Fig 4.2) affecting the orientation of the local wood-RT-plane, results in a rotation of the properties (analogous to an element-rotation in Mohr's circle). In layer 2, α is thus transformed as $\alpha_{2,x} = \alpha_{2,11} \cos^2(\varphi_2) + \alpha_{2,22} \sin^2(\varphi_2)$, and equally, the transformed stiffness, where $Q_{2,11}$ is calculated as in Eqs 4.2, reads

$$Q_{2,x} = Q_{2,11} \cos^4 \varphi_2 + Q_{2,22} \sin^4 \varphi_2 + 2(Q_{2,12} + 2Q_{2,66}) \sin^2 \varphi_2 \cos^2 \varphi_2. \quad (4.4)$$

Considering all moisture dependencies, thickness changes of layers and growth ring inclination, the resulting curvature κ over any Ω is calculated as

$$\kappa = \int_\Omega K d\omega + \kappa_0. \quad (4.5)$$

The total work performed, or resilient elastic energy stored, W ($[W] = Nm \cdot m^{-2}$), to achieve κ over Ω can be expressed, in the 2D case, as

$$W = \frac{1}{2} \int_\Omega K^2 F d\omega + W_0, \quad F_i = \frac{4(Q_i I_i + Q_i I_i)^2}{Q_i h_i (h_1 + h_2)^2} + Q_i I_i. \quad (4.6)$$

The factor F_i stands for contribution from layer i . For a bilayer with passive layer 1 and active layer 2, $F = F_1 + F_2$.

If, as in the calculation of Eq 4.3, it is assumed that the neutral axes situate at half the thicknesses of each layer and that stiffnesses Q_i are constant over cross-section, the axial maximal and absolute stress values in layer i at layer-interface and layer-edge (in \mathbf{e}_x -direction) can be expressed by

$$\sigma_i = \int_{\Omega} K \sqrt{\frac{2F_i Q_i}{h_i}} d\omega + \sigma_{i,0}. \quad (4.7)$$

We note that h, I, Q, K, W, F , and σ are all functions of ω , and that in a strict sense, the integrals of Eqs 4.5-4.7 can be evaluated for any given $\Delta\omega \in \Omega$. However, for practical application, it is convenient to replace them using an incremental approach. For Eq 4.5, e.g. $\kappa - \kappa_0 \approx \sum_i^n \Delta K_i \Delta\omega_i$ for $\Delta\omega_i = \Omega/n$, where in each increment, the geometry and engineering constants (all E, G , and ν) are updated for the actual moisture level.

4.4 MATERIALS AND METHODS

Bilayer validation samples

Six different configurations of cross-grained bilayers were fabricated from beech wood (*Fagus sylvatica* L.) grown in the region of Zurich, Switzerland. Three samples were fabricated for each configuration. The wood was initially conditioned at a wet climate of 85% r.h. (relative humidity) and 20°C. The single layers were cut as strips of 120 mm length and 20 mm width. For the six configurations, the thicknesses were varied according to the ratio $r = h_1(h_1 + h_2)^{-1}$ as shown in Table 4.1 where h_1 and h_2 denote thickness of layers 1 and 2 respectively (Fig 4.2). A growth ring angle φ_2 of zero was chosen for all experimental validation samples. The layers were glued using a one-component polyurethane glue (1cPUR, Purbond HB S709, Henkel & Cie AG, Switzerland) and manufacturer's standards were applied for the gluing procedure. The samples were placed inside a 35% r.h. and 20°C climate room to dry and curvatures were measured after $t = 1, 2, 4, 6, 8, 24$, and 48 hours using image analysis (polynomial fits to edge-thresholds). Simultaneously, wood moisture contents ω_t at time t were measured using a gravimetric determination method, i.e. $\omega_t = (m_t - m_0)m_0^{-1}$, where m_t is the sample mass at time t and m_0 is the oven-dry sample mass. Finally, experimental data is verified against Eq 4.5.

TABLE 4.1: **Configurations of experimental sample-set.** Layer thicknesses h_1 and h_2 of passive layers (layer 1) and of active layers (layer 2) in mm along ratios r .

h_1 (mm)	0.6	0.8	1.2	2.2	3.2	3.9
h_2 (mm)	4.1	4.1	4.1	4.1	4.1	4.1
$r = h_1(h_1 + h_2)^{-1}$	0.12	0.17	0.22	0.34	0.43	0.49

Sensitivity analysis

Defining Eq 4.5 as the model with uncertain input, where each parameter is following a specific probability density function (PDF) with given parameters or moments, model output variability can be assessed using a Monte-Carlo (MC) sampling approach. This procedure allows for calculating partial variances of the model parameters and their combinations w.r.t. the model output variance. We make use of total Sobol' indices to conduct a global-type sensitivity analysis of the model [133, 134]. The indices, normalized values between 0 and 1, for each parameter i , equal the contribution of variability of that parameter to the model output variability.

For the analysis, the *Matlab*-based uncertainty quantification tool *UQLab* was used [135]. The engineering constants E_L , E_R , and E_T entering the model (for the plane strain case), the three swelling coefficients α_L , α_R , and α_T , the two thicknesses h_1 , and h_2 , and the growth ring orientation φ_2 , were sampled using 10^7 MC samples. We assume a log-normal PDF for the material properties ($\{E_L, E_R, E_T, \alpha_L, \alpha_R, \alpha_T\} \sim \mathcal{LN}$), where a coefficient of variation ($COV = \sigma/\mu$) of 10% is attributed to each property, and a Gaussian PDF for the geometrical properties ($\{h_1, h_2, \varphi_2\} \sim \mathcal{N}$) where standard deviations (σ) of 0.1 mm , 0.1 mm and 1° are attributed respectively. Exemplary, four beech bilayer configurations were analyzed (described along Results). The mean values μ_i (first moments of the input PDFs of i) for the material properties are taken as in Fig 4.1. The described input parameters were chosen in view of direct applicability in industry. The Young's moduli, the differential swelling coefficients, and the geometry are deemed easier to record than other input parameters (i.e. shear moduli and Poisson ratios).

4.5 RESULTS

Model validation with experimental data

The plane strain (i) and the plane stress (ii) model formulations were validated against the obtained experimental results. Fig 4.3 presents the data of measured (κ^d) and predicted (κ^m) curvature versus wood moisture content (ω). The measured curvatures exhibit significant dependence on the ratio r . A maximum of $\kappa^d \approx 4.5 \text{ m}^{-1}$ was reached for $r = 0.17$ and a minimum of $\kappa^d \approx 1.5 \text{ m}^{-1}$ was reached for $r = 0.49$ after 48 hours in 35% r.h. climate, at $\omega \approx 9.5\%$. For the cases (i) and (ii), errors in prediction are displayed starting with a value of zero at initial conditions ($\omega \approx 17.5\%$). It can be seen, that the prediction errors are lower for model (i) than for model (ii). In fact, for low values of r ($r = 0.12$ and $r = 0.17$), both models slightly under-predict κ^d , while for higher values ($r = 0.43$ and $r = 0.49$), κ^d is over-predicted. At a value of $r = 0.34$, which corresponds approximately to $h_1 : h_2 = 1 : 2$, both models predict κ^d very well ($R_i^2 = 0.986$ and $R_{ii}^2 = 0.992$) with an absolute prediction error lower than 10%. Over all configurations, model (i) reached a mean goodness of fit (R^2) to experimental data of $\bar{x}_{R_i^2} = 0.972$ and model (ii) of $\bar{x}_{R_{ii}^2} = 0.950$.

Parametric study on curvature, elastic energy, and axial stress

In this section, κ , W , and σ_i are analyzed as function of r (from 0 to 1), of bilayer-thickness $h_1 + h_2$ (from 2 to 10 mm), and of φ_2 (0° , 45° , and 90°). A complete range of feasible configurations of thin beech bilayers is thus represented. The plane strain model for a moisture variation of $\Omega : 17.5\% \rightarrow 9\%$ was used, and the results are displayed in Fig 4.4a (configurations described in figure caption). Highest curvatures are reached at a same value of r regardless of $h_1 + h_2$. This optimal value of r (maximizing κ , e.g. at $r = 0.253$ for $\varphi_2 = 0^\circ$) is, however, shifted in function of φ_2 . The higher φ_2 is chosen, the higher κ for a same value of $h_1 + h_2$. High curvatures of $\kappa \approx 10 - 25 \text{ m}^{-1}$ result for 2 mm thick bilayers (depending on φ_2). By choosing higher values of $h_1 + h_2$, κ drastically drops in magnitude and seems to converge to a minimum value (at a given r) for large $h_1 + h_2$ according to the spacing of the curves in the semi-log plot for κ .

It can be seen, that W_{tot} is a linear function of total thickness $h_1 + h_2$ for any r (Fig 4.4b). Considering the contribution of layer 1 (W_1) and layer 2 (W_2) to W_{tot} separately, it is seen that there are values of r for each layer

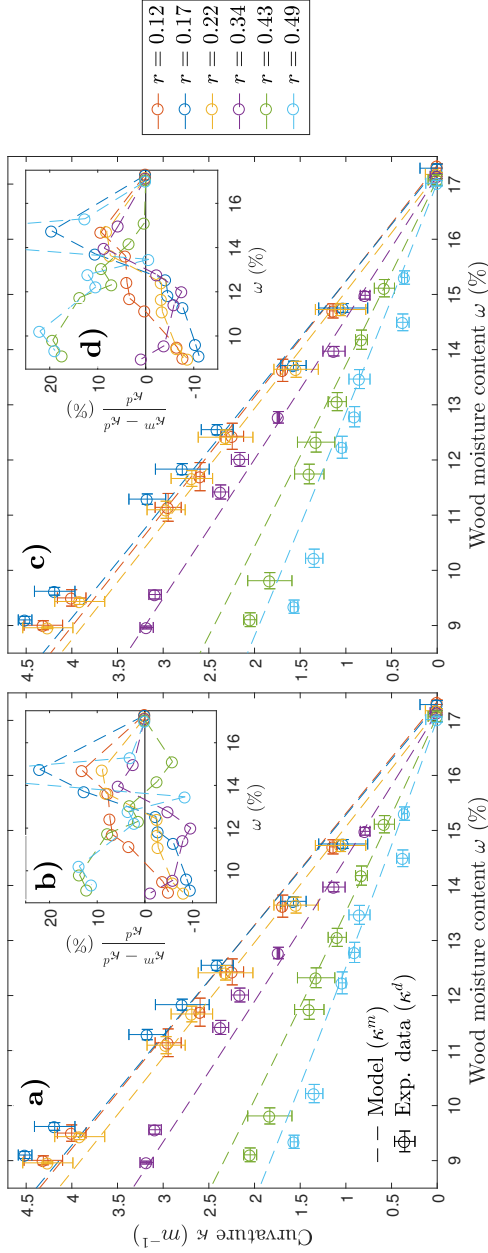


FIGURE 4.3: **Model curvature (κ^m) vs. experimental validation data (κ^d).** a) Plane strain model versus data (error-bars denote positive and negative standard deviations); b) Error in prediction of plane strain model with respect to experimental data $((\kappa^m - \kappa^d)/(\kappa^d - 1))$; c) Plane stress model versus data; d) Error in prediction of plane stress model with respect to experimental data.

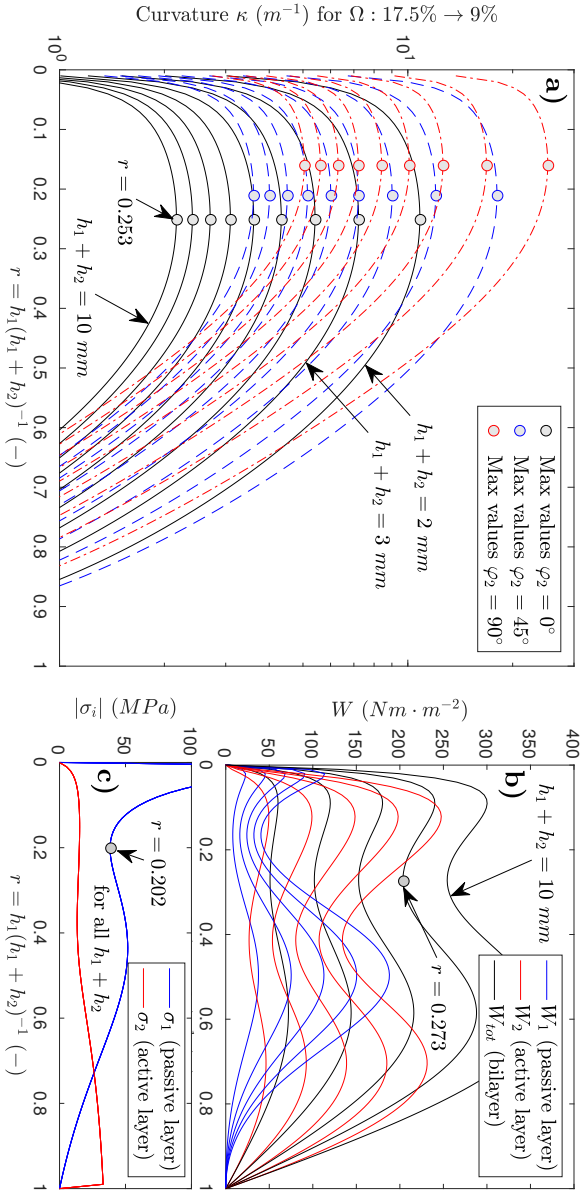


FIGURE 4.4: **Parametric study using plane strain model.** a) Curvatures κ (semi-log plot) versus all possible thickness ratios r over an exemplary moisture domain of $\Omega : 17.5\% \rightarrow 9\%$ for beech bilayers ($L//e_x$ in layer 1 and $R//e_x$ in layer 2, T in other directions). Black lines $\varphi_2 = 0^\circ$, blue lines $\varphi_2 = 45^\circ$, and red lines $\varphi_2 = 80^\circ$. $h_1 + h_2$ is chosen from 2 mm (top lines) to 10 mm (bottom lines) in steps of 1 mm. b) Strain energy W vs. r for same setup with $\varphi_2 = 0^\circ$. Blue and red lines represent contribution to W_{tot} (black line) from passive and active layers. $h_1 + h_2$ is chosen from 2 mm (top lines) to 10 mm (bottom lines) in steps of 2 mm c) Absolute values of axial stresses at interface σ_i for layer i , two curves represent all possible $h_1 + h_2$.

i where W_i is either minimized or maximized. As for κ , these r remain independent of $h_1 + h_2$. W_1 is minimized where W_2 is maximized and vice versa, and W_{tot} is minimized at $r = 0.273$. Surprisingly, the axial interface-stress does not depend on total bilayer thickness $h_1 + h_2$ but only on r (Fig 4.4c). Stresses in the passive layer are found to show higher dependence on r as those of the active layer. The minimum stress of the passive layer situates at $r = 0.202$, whereas for the active layer, stresses seem to remain approximately constant between $r = 0.1$ and $r = 0.4$.

Model input parameter sensitivity analysis

Results of the sensitivity analysis are displayed in Fig 4.5. Four different model configurations were considered for which r was set as the optimal value maximizing κ according to Fig 4.4 and $\Omega : 17.5\% \rightarrow 9\%$. In the case of $\mu_{h_1} = 1 \text{ mm}$ and $\mu_{\varphi_2} = 0^\circ$, most of the model response variability can be attributed to α_R . Input variabilities in thicknesses h_1 and h_2 also contribute to a small amount. In the case of $\mu_{h_1} = 2 \text{ mm}$, the contribution from the thicknesses is marginal, and all model variability seems to be exclusively attributed to the variability of α_R . Setting $\mu_{\varphi_2} = 45^\circ$, a major shift from α_R to α_T in total Sobol' indices can be observed. When $\mu_{\varphi_2} = 45^\circ$, additionally, some contribution seems to be attributed to Young's moduli in bilayer axial direction \mathbf{e}_x of the passive layer (E_L) and the active layer (E_R , but surprisingly not E_T). Regardless of the model configuration, no effects of input variability of the parameters φ_2 , E_T , and α_L are visible.

4.6 DISCUSSION

Model validity

It is seen that the proposed 2D linear elastic model can predict curvature of beam-like bilayer structures with narrow widths and thin layers. Model precision tends to get worse when high or low values of r (close to 1 or 0) are chosen. A plane strain state assumption predicted data better than a plane stress state assumption. This is in line with the known phenomena of strong out-of-plane effects of anisotropic materials when the out-of-plane material axis is stronger than the in-plane axis, as in the case of the active layer in a wooden bilayer. Besides, we note that curvature in such a bilayer is not a uni-axial phenomenon but, will happen about two perpendicular axes simultaneously. A wooden bilayer plate will, however, tend

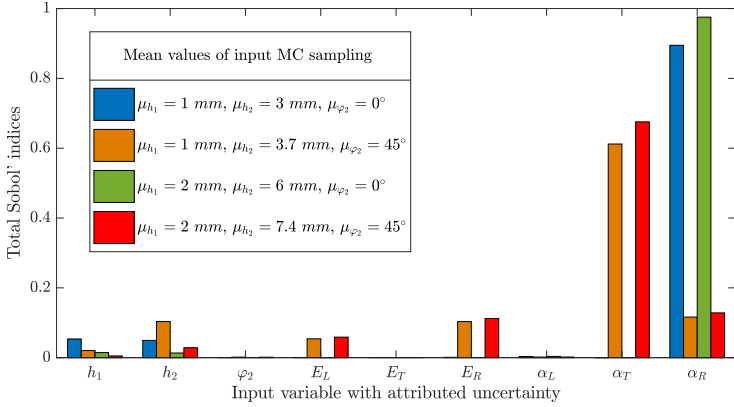


FIGURE 4.5: **Computed total Sobol' indices using plane strain model.** Four different exemplary configurations are considered. Two different thicknesses of passive layer are considered: $h_1 = 1\text{ mm}$ and $h_2 = 2\text{ mm}$. Thicknesses of active layers follow optimal values for ratio r (see in Fig 4.4a) for respective cases $\varphi_2 = 0^\circ$ ($r = 0.253$) and $\varphi_2 = 45^\circ$ ($r = 0.212$). These parameters constitute the first moments of the respective pdfs (μ_i).

to minimize the change in Gaussian curvature. Curvature out of plane is thus expected to affect axial curvature to some extent. Besides modeling only a reduced geometry (2D), known beech-wood-inherent deformation mechanisms such as visco-elasticity [114, 116], mechano-sorption [11], and plasticity [117] are here neglected for the sake of simplicity. Also, the presented model assumes steady-state moisture conditions, which is an ideal assumption, supposedly valid for thin layers. Time and moisture-diffusion effects, especially for increased layer thicknesses, are certainly of further interest when understanding wooden bilayer mechanical behavior. Overall, the relation $\kappa \propto \Delta\omega$ appears to hold true despite the highly non-linear nature of the model and the complex physical effects in experimental data.

Design principles

Given the validity of the presented model, design aspects can be discussed using parametric studies as presented in Fig 4.4. For any arbitrary configuration defined by local orientations L , T , and R , material properties, and growth ring angle φ_2 , the optimal thickness ratio r_{opt} , for which the curva-

ture κ is maximized (over any Ω) can be calculated applying $d\kappa/dr = 0$ and solving for r . In Ref [136] an exemplary solution for the case of isotropic bi-materials with constant material properties is given as $E_1 h_1^2 = E_2 h_2^2$, where E_1 and E_2 are the layer stiffnesses. For the presented model and wood, the optimal ratio r_{opt} is, however, dependent on many input parameters. It was seen that κ can be maximized, or W_{tot} and σ_i can be minimized, and that in either case r_{opt} is different. We state that in certain range of r , however, there is a tendency for the maximum curvature being reached while simultaneously, the system minimizes stored elastic energy and axial stresses. Furthermore, model prediction of validation data was better in the case of the samples with r close to r_{opt} , tending to the conclusion that maximized κ and minimized W and σ influence model precision and justify the use of a 2D linear elastic model, as presented, to predict κ for such cases. Given the opportunity to vary $h_1 + h_2$ or $\Delta\omega$ in order to set a target κ , we thus recommend to always set r to an optimal value r_{opt} when designing wooden bilayers.

Increasing model precision

The model parameters of relevance were identified as the swelling coefficients in the active layer in all of the cases studied. Nearly all variability in κ was attributed to the variability of α_R (or α_T). Other parameters appear to be of much lower relevance (vanishing total Sobol' indices), and it can be concluded that measuring and updating the model with those parameters is not necessary. By measuring the swelling coefficients and updating the model input to *in situ* values, most of the epistemic uncertainty in the model response can be reduced to nearly only including the aleatory uncertainty of that input (given the measurement is accurate). Aleatory uncertainty in model input parameters, however, can never be reduced. For wood, as a naturally grown material with high variability, a precision range of predicted model response compared to experimental validation data can realistically not be lower than the range of spread in measured input material parameters.

Remarks on cracking and delamination

Under mechanical, but mainly moisture loading, cross-laminated wooden structures are prone to cracking [137]. For thin wooden bilayers, two ba-

sic failure modes can be considered: Axial delamination of the adhesive bond at the layer interface, and transverse cracking in the active layer. Both modes supposedly originate from a combination of the crack separation modes I and II (mode-mixity). At the bilayer edges, the zero axial stress boundary condition results in a stress intensity factor K_I at the interface. In combination with the interface-inherent stress intensity factor K_{II} due to the shear transfer, the edge-near interface can be identified as a zone with high risk of failure. We refer to the work of Refs [138, 139] where the failure of multilayers is analyzed, and, as general finding, the term $h_i \sigma_i^2 Q_i^{-1} \Gamma_c^{-1}$ is to be minimized to reduce failure risk. Γ_c denotes the interface toughness and is a configuration-specific parameter to be experimentally determined. The dominant influence of the axial stress σ_i on the term can directly be recognized, underlining the importance of choosing a ratio r , for which axial stress is minimized (for beech bilayers with $\varphi_2 = 0$, $r_{opt,\sigma} \approx 0.2$). Layer thickness h_i , stiffness Q_i , and Γ_c , only have secondary effects on failure risk. We state that failure was not observed for the experimental bilayer samples in this study, but that it can hypothetically occur for very high $\Delta\omega$ in combination with unsuitable design.

4.7 CONCLUSIONS

We derive and propose a simple 2D linear elastic model for predicting curvature of thin wooden bilayers as a function of moisture change. The model takes into account moisture-dependent orthotropic properties for wood and a physically accurate reduction to two dimensions. Experimental curvature data of beech bilayers is accurately modeled within a 10% precision range given an optimal ratio of layer thicknesses. In the design process, anatomical orientations of wood in each layer, the wood species, the growth ring angle in the active layer, the applied moisture difference, and the bilayer thickness combined with the thickness ratio of passive and active layers need to be considered. An optimal thickness ratio can be found for every configuration where either bilayer curvature is maximized or the passive layer axial stress at the interface and the edge is minimized. Axial stresses are found independent of total bilayer thickness and only depend on thickness ratio and applied moisture content difference. Further, they exert a considerable influence on delamination risk. The variability in axial swelling coefficient in the active layer was identified to have a decisive impact on bilayer curvature. Finally, we recommend considering effects such

as moisture gradients or time-dependent mechanical behavior for modeling and design of wooden bilayers with increased layer thickness.

ANALYSIS OF HYGROSCOPIC SELF-SHAPING WOOD AT LARGE-SCALE

5.1 PUBLICATION PREAMBLE

Analysis of hygroscopic self-shaping wood at large-scale for curved mass timber structures

Philippe Grönquist^{1,2}, Dylan Wood³, Mohammad M. Hassani², Falk K. Wittel², Achim Menges³, Markus Rüggeberg^{1,2}

¹ Empa, Laboratory for Cellulose & Wood Materials, 8600 Dübendorf, Switzerland

² ETH Zurich, Institute for Building Materials, 8093 Zürich, Switzerland

³ University of Stuttgart, Institute for Computational Design and Construction, 70174 Stuttgart, Germany

Journal: Science Advances 5(9)

Submitted: 01 March 2019

Published online: 13 September 2019

DOI: <https://doi.org/10.1126/sciadv.aax1311>

Author contributions: PG designed and performed the analysis and experiments and wrote the paper. MR and FKW contributed to the conception and design of the analysis and experiments. MMH contributed to the numerical analysis. DW and AM contributed to the conception of application. All authors discussed and commented on the manuscript.

Key findings

- A novel method for production of form-stable curved mass timber products and building components by self-shaping is presented.
- Complex wood material model used for numerical simulation of self-shaping wood bilayers reveals precise contribution of elasticity, plasticity, visco-elasticity, and mechano-sorption to the total strain.
- 3D coupled modelling of mechanics and moisture diffusion reveals inversion of axial stress state at the bilayer surface and identifies a critical time in the drying process.

Abstract

The growing timber manufacturing industry faces challenges due to increasing geometric complexity of architectural designs. Complex and structurally efficient curved geometries are nowadays easily designed, but still involve intensive manufacturing and excessive machining. We propose an efficient form-giving mechanism for large-scale curved mass timber by using bi-layered wood structures capable of self-shaping by moisture content changes. The challenge lies in the requirement of profound material knowledge for analysis and prediction of the deformation in function of setup and boundary conditions. Using time- and moisture-dependent mechanical simulations, we demonstrate the contributions of different wood-specific deformation mechanisms on the self-shaping of large-scale elements. Our results outline how to address problems such as shape prediction, sharp moisture gradients, and natural variability in material parameters in light of an efficient industrial manufacturing.

5.2 INTRODUCTION

Wood is a vastly abundant, sustainable, and well-performing construction material. From its biological origin, it inherits material characteristics such as anisotropy and hygroscopy, which are still seen as drawbacks in wood technology as they limit traditional uses. In nature, many biological systems have been identified as being capable of large shape-changes in response to changes in humidity. The unique combination of anisotropy and hygroscopy with their smart structure makes this possible [14, 32, 34, 37–46]. Large shape-changes can reciprocally be achieved by wood cross-ply laminates with lay-up $[0^\circ/90^\circ]$, referred to as bilayers, when changing moisture content by either drying or wetting. Making use of the seeming inherent disadvantage of swelling and shrinkage of wood, thin wooden bilayers with fast dynamic responsiveness have recently been highlighted for diverse applications, predominantly as functional elements in biomimetic architecture [7, 8, 48, 65–69, 71, 74].

Using wood, we demonstrate the unique ability of upscaling the self-shaping mechanism of bilayers to the meter scale in order to obtain large-scale components with high curvature. The shaping process by drying of large wood bilayers is illustrated in Fig. 5.1A–D and an exemplary time-lapse video is shown in supplementary S1. After drying, multiple curved wood bilayer plates can be laminated together to produce curved cross-laminated timber (CLT) plates, which are fully form-stable, independent of further changes in moisture (Fig. 5.1E). Application concepts as efficient CLT roof or wall structural elements are shown in Fig. 5.1F–G. Using this innovative manufacturing approach, material waste by subtractive milling to shape is eliminated, while extensive cold-bending of thick lamellae is rendered unnecessary. In addition, higher curvature than in standard form-giving processes is enabled, while at the same time, thicker wood lamellae can be used. The shown concept is arbitrarily scalable in any in-plane direction of the CLT plate with respect to the size of available material. We suggest a 4D production approach [140–142] where a simulated target element shape enables design of the initial flat-shaped structure in function of boundary conditions such as change in wood moisture content (WMC), lamella thickness, or growth ring inclination. The shown approach has the potential to revolutionize mass timber production and application, for which the promotion is seen as key step towards improving sustainability in the modern building sector [4].

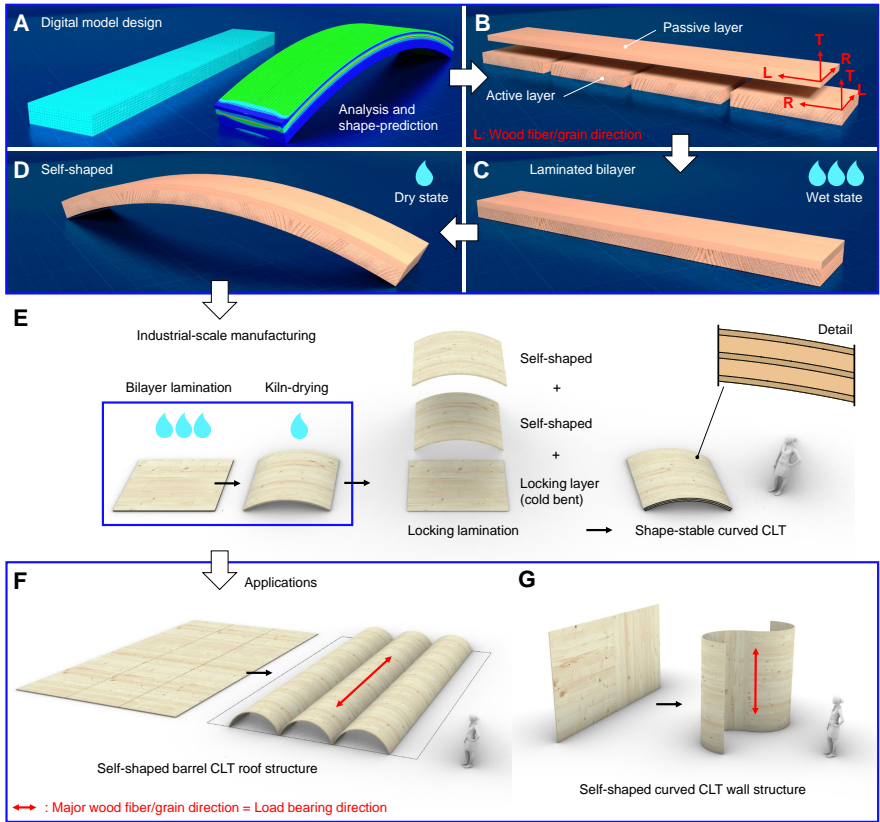


FIGURE 5.1: Self-shaping wood bilayer application at large-scale. **A-D:** Analysis and design process at laboratory scale. **E-G:** Industrial scale, same thickness but increased length and width of bilayers towards plate geometries. **A:** Parametric digital model and FE analysis for shape-prediction of arbitrary configuration. **B:** Example bilayer strip configuration (here, European beech wood) with passive and active layer components with wood anatomical directions radial (R), tangential (T), and longitudinal (L). **C:** Laminated wooden bilayer strip in initial, wet, and flat shape. **D:** Curved self-shaped bilayer after drying. **E:** Industrial-scale manufacturing (here, Norway spruce wood) in plate and shell configurations. Plates can be air-dried or kiln-dried to achieve self-shaping. Multiple shaped bilayer plates can be stack-laminated and in addition with a thin cold bent locking layer (with same thickness as a passive layer) to form shape-stable curved CLT. **F:** Application example as barrel vaulted CLT roof structure with wood fiber direction of thick lamellas (active layers) in load bearing direction. **G:** Application example as curved CLT wall with wood fiber direction of thick lamellas (active layers) in vertical direction.

To make use of this novel approach, a fundamental understanding of the mechanics of shape-change at large-scale is required and will be in focus of this study. Inspired by the analysis of bimetal thermostats [51], elastic models for predicting bilayer shape-change were developed and adapted for diverse swelling systems [15, 56, 143–145]. In the case of bilayers made out of hardwood species, such models have shown to perform reasonably well in predicting shape-change of thin layers of thickness below 10 mm [7, 146]. They do not, however, give suitable insight into the mechanical behavior of wood bilayers. Too many simplifying assumptions, such as restriction to linear elastic deformation, 2D geometry, or steady-state moisture conditions, are not valid for bulk wood. In fact, under time-dependent loading conditions as well as under simultaneous changes in WMC, wood displays more complex behavior. Under the high residual stress state induced by self-shaping [146], phenomenological deformation mechanisms such as visco-elasticity, mechano-sorption, and plasticity may simultaneously occur [11, 114, 121]. In addition to time- and moisture-dependent mechanical behavior, effects of moisture diffusion due to bilayer drying (or wetting) of exposed surfaces need to be considered. In the bulk, diffusion time is proportional to squared diffusion path when assuming Fickian transport laws. Thus, bilayer equilibration time in the target climate is drastically increased with lamella thickness and moisture gradients may heavily impact the time-dependent mechanical response.

We address the mentioned issues by 3D Finite Element (FE) analysis using an elaborate rheological model for wood. Experimental data of self-shaping by drying of three wood bilayer configurations made out of the abundant hard- and softwood species European beech and Norway spruce are shown. Hereby, the total bilayer thicknesses range from 15 to 45 mm. The numerically and experimentally investigated layer thicknesses are chosen in the optimal scale-range for industrial timber production. Thus, direct application is enabled without the need of further up-scaling studies. To capture influence of the inherent natural variability in material parameters on resulting shape, a global-type sensitivity analysis [133] is conducted.

5.3 MATERIALS AND METHODS

Constitutive material model for wood

Bulk wood is modeled using a 3D orthotropic, moisture- and time-dependent constitutive material model. The model is based on a representative elementary volume (REV) as shown in Fig. 5.2A. It considers all up-to-date known deformation mechanisms in coupled manner by additive decomposition of the total strain tensor assuming infinitesimal strain theory. Following [118], the Helmholtz free energy function Ψ is defined as

$$\Psi = \frac{1}{2} \epsilon^{el} C^{el} \epsilon^{el} + \frac{1}{2} \sum_{i=1}^n \epsilon_i^{ve} C_i^{ve} \epsilon_i^{ve} + \frac{1}{2} \sum_{j=1}^m \epsilon_j^{ms} C_j^{ms} \epsilon_j^{ms} + \frac{1}{2} \sum_{l=1}^r q_l \alpha_l. \quad (5.1)$$

The Cauchy stress tensor σ acting on a material point is in relation to the total strain tensor ϵ^{tot} by $\sigma = \partial \Psi / \partial \epsilon^{tot}$, where ϵ^{tot} decomposes as shown in Fig. 5.2B into elastic, plastic, visco-elastic, mechano-sorptive, and swelling and shrinkage strain components. In the first term of Eq. 5.1, C^{el} represents the elastic stiffness tensor. C_i^{ve} is the i -th visco-elastic stiffness tensor and C_j^{ms} is the j -th mechano-sorptive tensor of the respective Kelvin-Voigt rheological elements connected in series ($n = 4$ and $m = 3$) (Fig. 5.2B). The last term in Ψ considers the isotropic hardening energy standing for irrecoverable plastic deformation accumulated by a multi-surface plasticity model (r denotes number of active yield mechanisms, q_l the plastic hardening functions and α_l the internal hardening variables for $l=R,T,L$). All element entries of the mentioned compliance tensors (C^{-1}) for the species European beech and Norway spruce are considered as functions of moisture ω . Further, hygro-expansive (ϵ^ω) and elastic (ϵ^{el}) deformations are rate-independent, and ϵ^ω is independent on σ . A detailed description of the material model, used material parameters, and numerical implementation into the FE framework *Abaqus CAE* as a user material subroutine is found in [11, 121].

Computational model

Wood bilayers were modeled using the FE method with the above described material model. The geometrical model and BCs are presented in Fig. 5.2c. The dimensions were chosen according to the experimental sample set described below. The interface region, acting as a diffusion barrier,

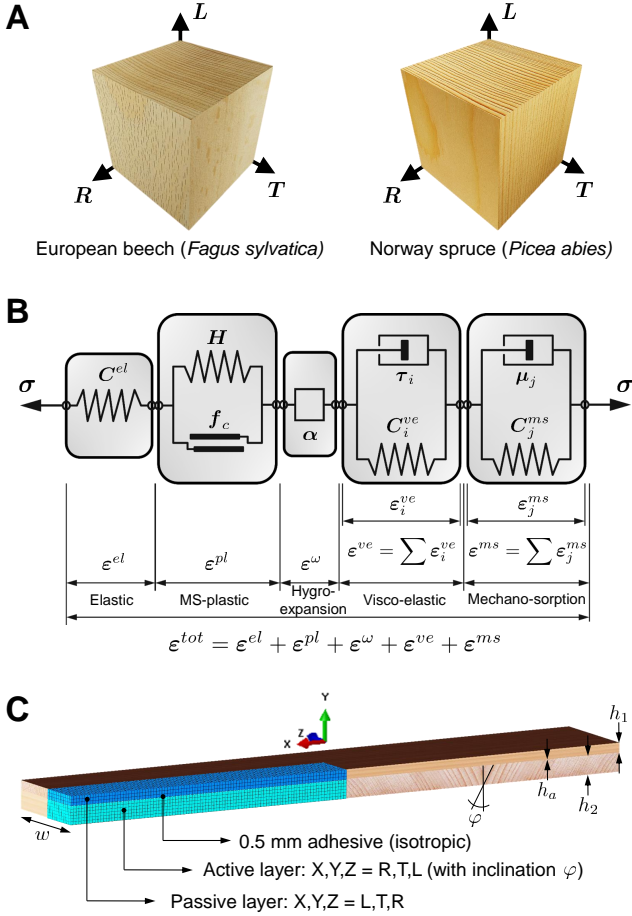


FIGURE 5.2: **Simulation model.** **A:** REV for wood material model (beech and spruce wood) with anatomical growth directions R, T, and L. **B:** Schematic rheological model for bulk wood as in [11]. **C:** Setup and BC for the FE bilayer models (quarter model with XY and YZ symmetry). Symbols: C : Stiffness matrices of springs for respective deformation modes, H : Hardening moduli, f_c : Yield functions, α : Differential swelling coefficients, τ_i : Characteristic retardation times, μ_j : Moisture analogous to τ_i , σ and ϵ : Stress and strain tensors.

was modeled by a 0.5 mm thick and isotropic one-component polyurethane adhesive (1cPUR) by tie connection. The moisture diffusion process (BC for surface moisture flux) was inversely fitted to experimental data of average moisture content evolution over time by comparing the volume-weighted average WMC. Analogy between temperature and moisture was made for modeling transient diffusion using Fick's second law; $\partial\omega/\partial t = \nabla(\mathbf{D}\nabla\omega)$ is equivalent to $(\rho c_T)\partial T/\partial t = \nabla(\mathbf{K}\nabla T)$ when $\rho c_T = 1$, so that the matrix of diffusion coefficients D equals the matrix of thermal conductivity coefficients K . In a first step, heat transfer analyses were conducted using 20-node quadratic brick elements. The resulting temperature evolution fields were then used as predefined fields for static analyses with same mesh and elements. A large deformation theory was applied. Resulting bilayer curvature was calculated as $\kappa = -2u_y(u_y^2 + (l + u_x^2))^{-1}$, using the tip displacements u_x and u_y and assuming a uniform circle-arc-segment-shaped bilayer of initial length l .

Analytical model

An analytical model, derived in [146] (Content of chapter 4), was used to alternatively model the investigated wood bilayer configurations. The model follows Timoshenko's work on bimetal thermostats [51] but further represents the anisotropic and moisture-dependent material behavior of wood in 2D by assuming a plane-strain state. A linear elastic deformation mechanisms is considered exclusively.

Experimental samples

Using European beech (*Fagus sylvatica*) and Norway spruce (*Picea abies*) wood conditioned at 95% RH and 85% RH respectively, three bilayer configurations were produced for each species. Beech was conditioned in adsorption and spruce in desorption equilibrium from the green state. This setup targeted a similar initial moisture content for comparability of both species. The used wood was defect-free and cut from the same stem respectively. A scheme of the bilayer setup is given in Fig. 5.2c, where the local, wood-anatomical orientations R,T,L are given in terms of global orientations X,Y,Z for passive (layer 1, top) and active (layer 2, bottom) layers. The components were bonded using 1cPUR adhesive (HB S309 Purbond, Henkel & Cie. AG, Switzerland) as curing by poly-addition enables gluing at high moisture contents. A constant thickness ratio of $h_1 : h_2 = 1 : 2$

(passive:active) was maintained in all configurations. The total thicknesses $h_1 + h_2$ of the three configurations were chosen to be 15 mm (config. 1), 30 mm (config. 2) and 45 mm (config. 3). Width and length of bilayers were chosen to be 100 and 600 mm. In the active layers, growth ring inclinations (φ) of $0 - 20^\circ$ for the beech and $0 - 30^\circ$ for the spruce were measured on reference samples (details in supplementary S4). After production in initial climate, the beech samples were relocated in 65% RH and the spruce samples in 50% RH climate for drying. Curvature and weight were measured over 900 hours of acclimatization time on 8 samples per configuration. Curvature was calculated as $\kappa = \psi''(1 + \psi'^2)^{-3/2}$ by image analysis. Second order polynomials ψ were fitted to thresholded edge-segments obtained by applying a Canny edge detector algorithm. Wood moisture contents ω were determined using reference samples cut from the bilayer samples prior to climate relocation (details in supplementary S4).

5.4 RESULTS

Shape-change after drying

Climate-induced shaping of three investigated bilayer configurations, i.e. increase in curvature and decrease in WMC over time is represented in Fig. 5.3 for two wood species, European beech and Norway spruce, respectively. The investigated experimental samples showed neither cracking in the bulk wood nor delamination at the bond lines during the shaping process, in which they were relocated from a high to a low relative air humidity (RH) climate at 20°C . WMCs were approximately equilibrated after 400 hours in the dry target climate, except for the bilayer series with a thickness of 45 mm, for which an equilibration is not visible after 900 hours. Beech bilayers reached an equilibrium WMC of around 14.5%, representing a difference of 7.5% as compared to the initial state. Spruce bilayers reached around 12.5% with a difference of approximately 9% in WMC. Despite the larger difference, curvature of spruce bilayers was lower than that of beech bilayers for all three configurations respectively. In the case of beech bilayers (Fig. 5.3A), curvature is simulated with reasonable accuracy, including light over-estimation. In contrast, for spruce (Fig. 5.3B), considerable overestimation can be recognized. Comparing both beech and spruce FE simulations with the performance of a simple analytical model derived for shape prediction, a matching trend can be observed. The predictions

by both models are close, and especially for spruce, do not appear to considerably differ in comparison to the data.

Stress and strain states

Bilayer axial stresses and strains as a function of square-root of drying time are shown in Fig. 5.4 for all configurations and at four relevant points of interest, namely, at the outer edge and interface of both passive and active layer, respectively. Maximum compressive stresses of around 30 MPa for beech and 25 MPa for spruce are found at the passive layer interface. At the passive layer edge, the tensile stresses range between 17 and 24 MPa. No distinct difference between species nor any dependency on bilayer thickness of the stresses can be recognized. However, in the active layer, stress is in general found higher for beech than for spruce. At the edge of the active layer, tensile stresses up to 6 MPa are developed until approximately 100 hours of drying. And after that, they reverse into compression. The opposite pattern is observed at the active layer interface where final tensile stresses range between 2 to 8 MPa. Across the entire bilayer cross-section and after 900 hours, the stress states show the typical bending-stress shape of two bonded layers [51].

For the elastic strains a similar pattern as in the case of the stresses can be observed. The highest elastic strains reach 0.25% in the passive layer, and 0.55% in the active layer. No systematic influence of bilayer thickness nor species can be seen. The visco-elastic strains are in the same order of magnitude as the elastic strains. However, here, an apparent difference between the two species beech and spruce can be observed. Visco-elastic strains are approximately twice as high for beech than for spruce. Noticeably, the visco-elastic strains do not converge even after 900 hours, while curvature and WMC remain constant after 400 hours already. Mechano-sorptive strains for the passive layer are lower by approximately one order of magnitude compared to the other two strain components and show convergence after 900 hours. Plastic strains do not appear for any configuration.

Sensitivity analysis

A global-type, non-linear sensitivity analysis for quantification of uncertainty in model input parameters is presented in the supplementary material S2-S4. For beech wood bilayers, variability in simulated shape is ob-

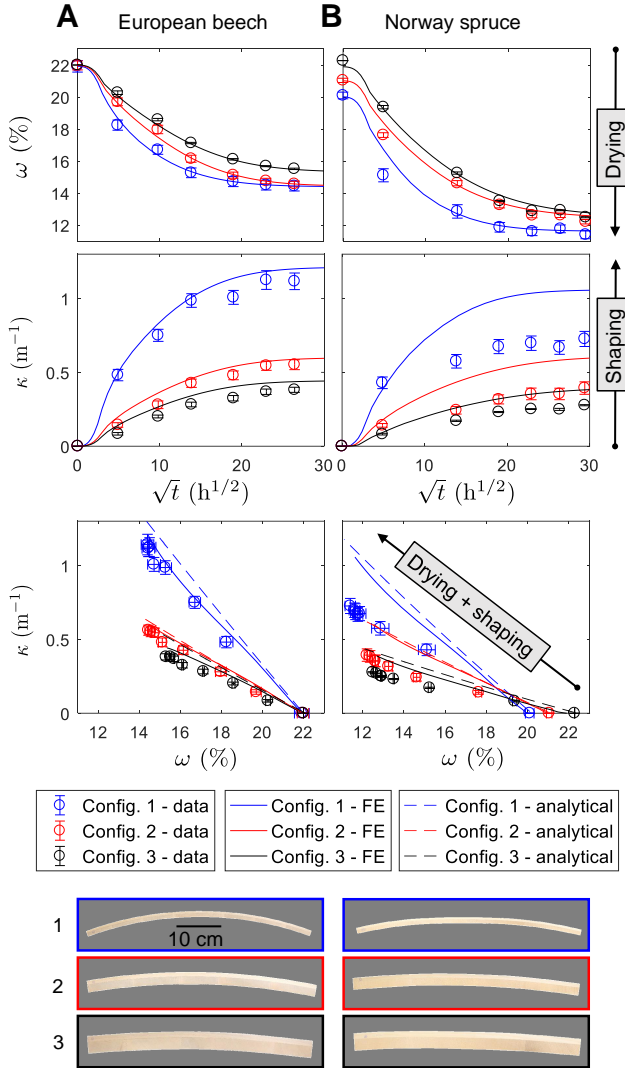


FIGURE 5.3: Shape-change after drying. Bilayer samples (config. 1-3, depicted at bottom) made out of beech (A) and spruce (B) wood during 900 h drying time. Drying dynamics (WMC, denoted ω) as simulated by the FE models and measured on experimental samples (error bars denote positive and negative standard deviations). Curvatures (denoted κ) versus square-root of time, and curvatures vs. moisture contents with comparison to model predictions.

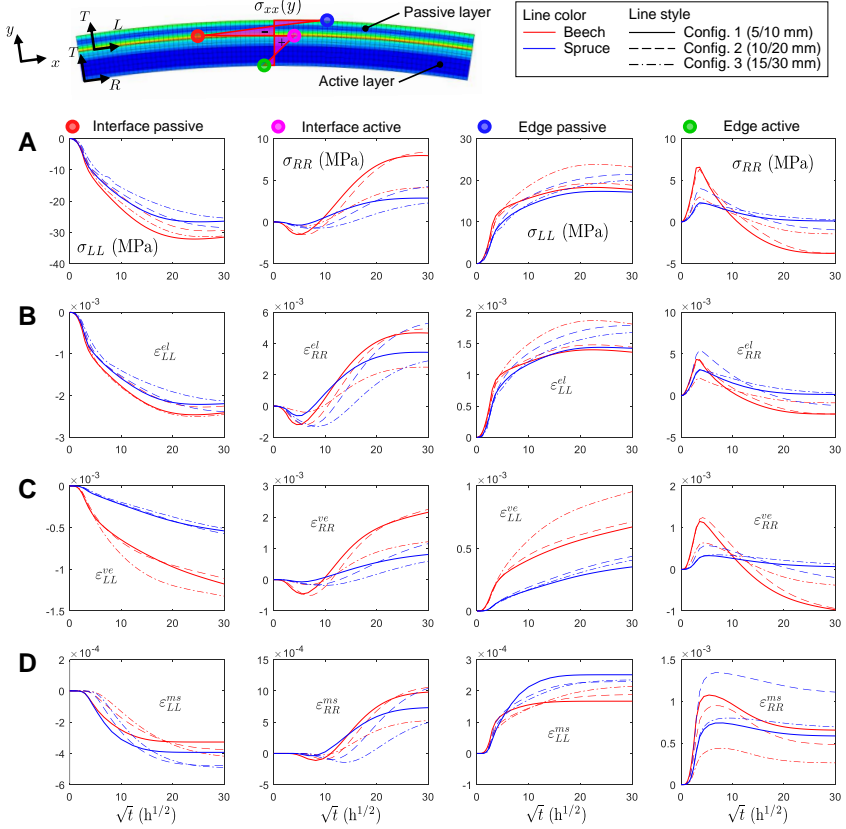


FIGURE 5.4: Shaping-induced stresses and strains. **A:** Bilayer axial stress states (σ_{xx} , indices LL for passive and RR for active layer corresponding to local wood-anatomical coordinate system) at four points of interest versus time (t) for configurations 1-3 and both wood species. Strain state (ϵ_{xx}) separated in individual contributors. **B:** Elastic (ϵ_{xx}^{el}). **C:** Visco-elastic (ϵ_{xx}^{ve}). And **D:** Mechano-sorption (ϵ_{xx}^{ms}). Irreversible plastic strains (ϵ_{xx}^{pl}) equal zero for all configurations. Total strains (ϵ^{tot}) and hygro-expansion strains (ϵ^{ω}) are not shown.

tained as being entirely dependent on variability in the axial swelling (or shrinkage) coefficient of the active layer. In the case of spruce, the variability in axial stiffness of layers appears to dictate variability in shape-change.

5.5 DISCUSSION

Self-shaping by drying within the hygroscopic range of wood has been demonstrated for lamellae thicknesses up to 30 mm and for two abundant European wood species from the hardwood and the softwood type. Commonly, wooden cross-ply laminates such as CLT experience extensive cracking and delamination due to high environmentally induced residual stresses [137]. Especially for hardwood species, standard-conform gluing for structural applications is still challenging. To avoid moisture induced delamination, the application of priming solutions before applying polyurethane adhesive is recommended [147, 148]. For the case of self-shaping wood, this is not necessary. In fact, the mechanical compatibility of bilayer structures, allowing large unconstrained deformations, prevents delamination even for very high changes in WMC.

The computational model fairly predicted the curvature of beech bilayers, while spruce bilayer curvature was overestimated in all configurations. Up to date unknown material non-linearity in wood or inaccuracy in used material parameters may contribute to the observed deviation. In addition, a more accurate model may be provided by considering the next smaller representative elementary volume (REV). At the intra-growth-ring scale, spruce shows considerably larger inhomogeneity compared to beech because of more pronounced differences in material properties of early- and latewood. Such localized mechanical behavior may considerably affect mechanics at large-scale. However, the required material parameters are still missing and collecting them is a non-trivial task. Considering that Norway spruce is one of the most widely used construction woods, a future clarification is certainly of great interest.

The sensitivity analysis revealed that in the case of beech wood, all model variability can be attributed to the natural variability in swelling coefficients. Therefore, a statistical analysis thereof needs to be conducted in order to increase model prediction (an example is shown in supplementary S4). The other input parameters are of negligible relevance in terms of reducing uncertainty in shape-prediction, given the model is valid as in the case of beech. This finding is relevant for application cases where there is a large apparent variability in quality of available material. In the case

of spruce wood, a single dominating parameter could not be identified. Effectively, even by attributing a coefficient of variation (COV) of 10% to the most important considered parameters, identified as being the axial elastic layer stiffnesses, total model variation is found to be 3.99% only (supplementary S2). Since the probability that the model-propagated uncertainty decreases is low, further parameters remain to be investigated to explain the more complex behavior of spruce wood.

A further insight provided by the sensitivity analysis is that the parameters of the adhesive layer, namely its thickness, stiffness, and shear modulus, do not influence shape-change. This can be explained by the fact that in bilayer laminates, the edge stresses dictate deformation due to the bending regime, even though stresses are found highest at the interface. The exclusive task of the adhesive bond is to block relative deformation of the two layers with respect to each other. This implies that modeling and accounting for an adhesive layer is not necessary for self-shaping bilayer composites where bond thickness is small compared to the lamina thickness. However, modeling an adhesive bond accounts for correct moisture and drying behavior, as it represents a diffusion barrier.

In terms of predicting shape-change alone, simple analytical models proved to be equally suitable even for thick lamellae. However, axial stresses developing over drying time were found considerably lower in the FE analyses than if the analyses were conducted using a 2D linear elastic-only model [146]. In the FE analyses, relaxation occurred in both passive and active layers simultaneously, seemingly canceling out influence on curvature. Independent of the thickness or species, visco-elastic strains did not fully converge after 900 hours of drying even though curvature change has already ceased before, indicating a layer-wise compensation. As a consequence, mechanical energy dissipation can here not be correlated with shape-change. Accordingly, bilayer shape-change can be interpreted as originating from a ratio of axial stresses of active to passive layer, and thus is unaffected by stress magnitudes. This can be used to explain the observed accuracy of analytical models that neglect complex deformation mechanisms. In fact, in such models, elastic material parameters enter a simple expression in terms of ratios [7, 51].

The FE analyses showed that bilayer thickness does not affect axial stress magnitudes, which confirms findings in [146]. Thicker wood bilayers resulted in lower curvature solely due to the cross section's higher second moment of area increasing the bending stiffness. For industrial large-scale application, this implies that any arbitrary lamella thickness can be used

in consideration with the trade-off in target curvature. Design principles valid for thin layers at small scale can therefore also be applied at large scale.

It was seen that no plastic strains develop and that the maximum axial stresses for beech and spruce are far lower than theoretical yield stresses or strengths. For beech and spruce, axial stresses in passive layer after 900 hours roughly reach 60% of the theoretical yield stress in L-direction (e.g., at $\omega = 14.5\%$, $f_{c,L} = 53$ MPa for beech [11]). In the active layer, the maximal stresses scale as 70% and 50% of the strengths in R-direction for beech and spruce. The fact that no irreversible strains were accumulated can be attributed to the slow drying dynamic allowing time for relaxation. These findings imply that in the case of application of bilayers as climate-regulated actuator elements, shape-change dynamics and shape-reversibility are affected by rate-dependent deformation mechanisms. This may be relevant for any dynamic bilayer structure made from biological materials. However, as mentioned above, final shape in a state where moisture- and time-dependent deformation mechanisms converged, is mainly influenced by factors affecting stress state and bending stiffness, such as layer thicknesses, expansion coefficients, or elastic material properties.

Moisture gradients were shown to have significant effects on the developing stresses and strains. This was demonstrated in Fig. 5.4 where for the case of the active layer edge, stress and strain states inverted over the drying time. The outer active layer edge, which is drying first, will shrink and develop tensile stresses and set the still wet core under compression. Later in time, when moisture gradients decrease, bending regime takes over as the bilayer bends and stresses invert to compression. A critical moment is identified when the strongest moisture gradients are created caused by boundary condition (BC) driven drying. For the investigated samples, this critical time can be identified as being 10-20 hours after climate relocation. There, the gradient-induced tensile stresses of the active layer edges are maximal and close to theoretical strength values. A fast drying procedure creating sharp moisture gradients may thus lead to cracking in the active layer. When using drying kilns at industrial scale, a mild drying procedure is thus recommended in order to avoid potential cracks, which would affect target curvature.

5.6 SUMMARY

Self-shaping was presented as a novel concept for industrial production of form-stable curved mass timber elements. The combination of a computational mechanical analysis, a sensitivity analysis, and an experimental investigation has revealed insight into the complex behavior of the self-shaping mechanism of wood. Specific large-scale problems, such as predictability of shape, sensitivity to natural variation in material properties, or drying procedure were addressed and discussed for two wood species, for which considerable differences were identified. Target curvature remains constant if layer stress ratios remain balanced under the influence of different deformation mechanisms. Creep mechanisms prevent exceeding yield stresses and strengths during shaping. Axial stress levels remain independent of bilayer thickness given the layer thickness ratio is the same. And a critical moment is reached when axial stresses in the active layer are of tensile nature due to the initial BC-dictated drying phase. The findings enable application of the biomimetic self-shaping of wood at large-scale and promote its integration into mass timber industry.

5.7 SUPPLEMENTARY MATERIALS

S1. Time-lapse video of large-scale wood bilayer actuation

Link to the video

https://advances.sciencemag.org/highwire/filestream/218766/field_highwire_adjunct_files/0/aax1311_Movie_S1.mp4



FIGURE 5.5: **Video Caption.** Shape-change of a large-scale Norway spruce bilayer plate with total thickness of 31.5 mm (passive and active layer thicknesses of 6.5 and 25 mm), length of 1.5 m, and width of 0.5 m. **A:** Production in initial flat shape with wood conditioned at 85% RH. **B:** Self-shaping in 35% RH and room temperature over 270 hours.

S2. Sensitivity analysis

Methods

A sensitivity analysis using total Sobol' indices S_i^{tot} was conducted on the FE models of the wood bilayers. S_i^{tot} reveal how much an attributed uncertainty, i.e. a distribution function of a certain model input parameter contributes to the final model output distribution. The computational costs of the FE models did not allow for a standard Monte-Carlo (MC) sampling approach in order to conduct the sensitivity analyses. Using a MC based calculation, the convergence rate is $\propto N^{-1/2}$, where N is the number of MC samples, i.e., required model evaluations. A convenient surrogating approach is to replace the model by a set of sparse truncated polynomial chaos (PC) expansions [149]. The derivation of the sensitivity measure S_i^{tot} from PC expansion is described in supplementary S3. Here, bilayer curvature after 900 hours represents the model response ($Y = \kappa$) for beech and spruce bilayers drying from 21% to 14% WMC. The selected input variables (their number M is limited, even for sparse PC approaches) with associated uncertainty were divided in three categories per wood species such that six sensitivity analyses were conducted, denoted UQ 1-6. Odd and even numbering correspond to beech and spruce bilayers respectively.

- UQ 1 & 2: The influence of the variability in geometry is analyzed together with variability in adhesive material properties. Uncertainty was attributed to the bilayer thicknesses (h_1 and h_2) and width (w), the adhesive layer thickness (h_a), the growth ring orientation in active layer (φ), and to the Young's and shear moduli of adhesive (E_a and G_a , for 1cPUR at $\omega = 0$).
- UQ 3 & 4: Here, variability was attributed only to the independent engineering constants in the wood elastic compliance tensor C^{el} , i.e. to E_R , E_T , E_L , G_{RT} , G_{RL} , G_{TL} , ν_{TR} , ν_{LR} , ν_{LT} , at $\omega = 0$.
- UQ 5 & 6: Finally, the most relevant parameters from UQ 1-4 were chosen along with the three differential swelling coefficients α_R , α_T , and α_L .

All input parameters were assumed as being independent random variables following a specific probability density function (PDF) with parameters as given in Tab. 5.1. Geometrical parameters were assumed to follow a Gaussian PDF (\mathcal{N}) and material properties a lognormal PDF (\mathcal{LN}). An updated probabilistic input model, namely a three-parameter Burr Type

XII PDF (β_{XII}) was chosen for α_R . The parameters of the updated PDF were experimentally determined and the statistical analysis is described in supplementary S4 (Fig. 5.7 and Tab. 5.2).

The PC expansion was conducted using the *UQlab* framework in *Matlab* [135]. The MC-sampled set of input parameters is transferred from *Matlab* to parametric *Python* (FE model) and *Fortran 77* (material model) scripts for the automated UQ and FE analysis via parameter interfacing scripts. The obtained simulated data set, chosen as 150 FE model evaluations for each sensitivity analysis, allowed calculation of the sparse PC expansions with a total polynomial degree of $p = 5$ using a least angle regression method.

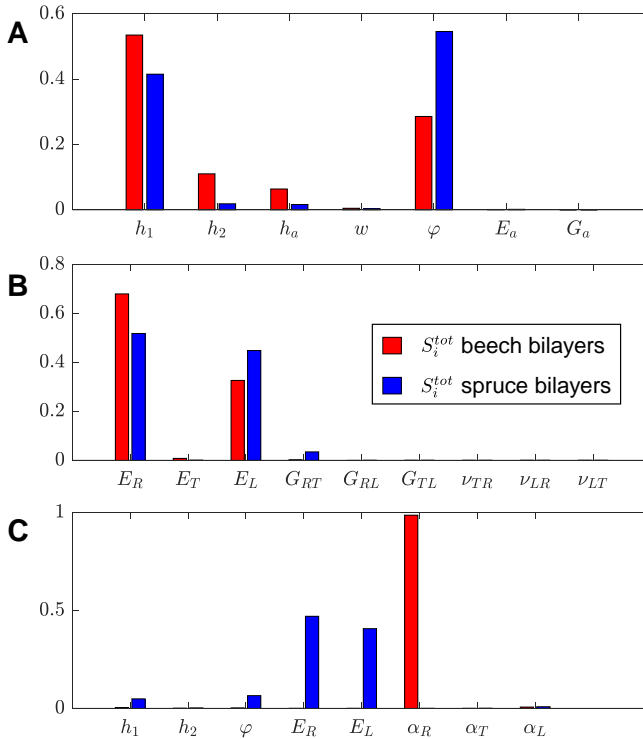


FIGURE 5.6: **Results of sensitivity analyses.** Values of total Sobol' indices S_i^{tot} for UQ 1-6 for Config. 2 of beech (red) and spruce (blue) bilayers. UQ 1 and 2 (A), UQ 3 and 4 (B), and UQ 5 and 6 (C).

Results

The total Sobol' indices S_i^{tot} from the six conducted UQs are displayed in Fig. 5.6 and the corresponding model output Y can be found in Tab. 5.1. From UQ1 and UQ2, it can be seen that variations in adhesive properties (E_a and G_a) completely vanish in terms of output κ and that in the same analyses h_1 and φ are mostly responsible for variations in κ . For beech, h_2 and h_a are attributed minor importance as well. In the second analyses (UQ3 and UQ4) only the axial layer stiffness E_R (active layer) and E_L (passive layer) seem to be of relevance. These values, along with the swelling coefficients were chosen for the third set of analyses, UQ5 and UQ6. Here, considerable differences are visible between the two species, as for beech, only variation in α_R seems to impact variation in κ . On the other hand, for spruce, the layer stiffnesses appear to be the most important model input parameters.

TABLE 5.1: **Input and output of uncertainty quantification.** Model input parameters (X_i) with used sampling parameters (i.e., attributed uncertainty μ and COV, and with PDFs \mathcal{N} , \mathcal{LN} , and \mathcal{BXII}) and model output (Y) for the six conducted sensitivity analyses. First moments (μ) represent ordinate axis intercept of moisture dependent function of the wood independent engineering constants taken from [11], i.e., at $\omega = 0$. UQ 1,3, and 5 for beech bilayers (black font), and UQ 2,4, and 6 for spruce bilayers (gray font).

X_i		Y									
UQ 1 & 2	μ	h_1	h_2	h_a	w	φ	E_a	G_a	κ		
		10 mm	20 mm	0.5 mm	100 mm	10°	754 MPa	290 MPa	0.55 mm ⁻¹	0.42 mm ⁻¹	
		10 mm	20 mm	0.5 mm	100 mm	10°	754 MPa	290 MPa			
	COV	1%	0.5%	10%	0.5%	10%	10%	10%	10%	0.73%	
		1%	0.5%	10%	0.5%	10%	10%	10%	10%	1.38%	
	PDF	\mathcal{N}	\mathcal{N}	\mathcal{N}	\mathcal{N}	\mathcal{N}	\mathcal{LN}	\mathcal{LN}			
UQ 3 & 4	μ	E_R	E_T	E_L	G_{RT}	G_{RL}	G_{TL}	ν_{TR}	ν_{LR}	ν_{LT}	κ
		2566 MPa	885 MPa	17137 MPa	668 MPa	1482 MPa	1100 MPa	0.29	0.38	0.34	0.55 mm ⁻¹
		1000 MPa	506 MPa	12792 MPa	61 MPa	763 MPa	881 MPa	0.15	0.23	0.29	0.42 mm ⁻¹
	COV	10%	10%	10%	10%	10%	10%	10%	10%	10%	1.77%
		10%	10%	10%	10%	10%	10%	10%	10%	10%	3.79%
	PDF	\mathcal{LN}	\mathcal{LN}	\mathcal{LN}	\mathcal{LN}	\mathcal{LN}	\mathcal{LN}	\mathcal{LN}	\mathcal{LN}	\mathcal{LN}	
UQ 5 & 6	μ	h_1	h_2	φ	E_R	E_L	α_R^a	α_T	α_L	κ	
		10 mm	20 mm	10°	2566 MPa	17137 MPa	0.00178% ⁻¹	0.0040% ⁻¹	0.00011% ⁻¹	0.55 mm ⁻¹	
		10 mm	20 mm	10°	1000 MPa	12792 MPa	0.00169% ⁻¹	0.0033% ⁻¹	0.00005% ⁻¹	0.42 mm ⁻¹	
	COV	1%	0.5%	10%	10%	10%	7.56%	10%	10%	8.33%	
		1%	0.5%	10%	10%	10%	13.86%	10%	10%	3.99%	
	PDF	\mathcal{N}	\mathcal{N}	\mathcal{N}	\mathcal{LN}	\mathcal{LN}	\mathcal{BXII}	\mathcal{LN}	\mathcal{LN}	\mathcal{LN}	

^a Values as determined in Fig. 5.7 and Tab. 5.2

S3. The sensitivity parameter S_i^{tot}

Any computational model \mathcal{M} with model-response random vector $Y = \mathcal{M}(X)$ and input random vector $X \sim f_X$, where f_X is the product of each marginal distribution assuming a set of M independent input parameters, can be expressed using a spectral approach [150, 151]. The response Y is considered as point in a function space of square integrable functions (\mathbf{L}^2) with coordinates y_α . Hereby, the set of multivariate polynomials $\{\Psi_\alpha, \alpha \in \mathbb{N}^M\}$ form an orthonormal basis in \mathbf{L}^2 . The (M -dimensional) multivariate basis is given by

$$\Psi_\alpha(x) := \prod_{i=1}^M \Psi_{\alpha_i}^{(i)}(x_i) \quad (5.2)$$

and the model response can be written as

$$Y = \mathcal{M}(X) = \sum_{\alpha \in \mathbb{N}^M} y_\alpha \Psi_\alpha(X) \approx \sum_{\alpha \in \mathcal{A}^{M,p}} y_\alpha \Psi_\alpha(X), \quad (5.3)$$

where $\alpha \in \mathbb{N}^M$ is a multi-index of dimension M and $\mathcal{A}^{M,p}$ defines a sparse truncated basis set of total polynomial degree p . The residual resulting from the truncation is minimized by a least-square method. The finite number of coefficients y_α of the polynomial for the truncated expansion can, due to the orthogonality of the basis, be individually calculated by projection of \mathcal{M} onto Ψ_α :

$$y_\alpha = \langle \mathcal{M}(X), \Psi_\alpha(X) \rangle = \int_{\mathcal{D}_X} \mathcal{M}(x) \Psi_\alpha(x) f_X(x) dx, \quad (5.4)$$

where \mathcal{D}_X is the support of the probability density function f_X . The integral can be evaluated by quadrature where the chosen type of polynomial is orthogonal with respect to the corresponding weight function w such that $w \equiv f_X$. A limited number of model evaluations is sufficient for calculating y_α . The obtained PC expansion can then be rearranged to read analogous to a Sobol' decomposition [152]. Total Sobol' indices S_i^{tot} for input variable X_i of the model can, thus, be directly computed with the obtained coefficients y_α as

$$S_i^{tot} = D_i^{tot} / D = \sum_{\alpha \in \mathcal{A}_i^{tot}} y_\alpha^2 / D, \quad (5.5)$$

such that $\mathcal{A}_i^{tot} = \{\alpha \in \mathbb{N}^M : \alpha_i > 0\}$, D_i^{tot} is the partial variance (sum over all orders) of parameter X_i , and D is the variance of Y ($D = \text{Var}[\mathcal{M}(X)]$).

S4. Statistical analysis of shrinkage coefficient in active layer

Measurement and determination of coefficient α^φ

Differential shrinkage coefficients (also referred to as swelling, moisture expansion or contraction coefficients) were measured on 207 reference samples of beech and 132 of spruce. The samples were cut from the active layers of the investigated bilayer samples as cuboid samples with edge length corresponding to thickness of active layers (for config. 1-3, 10, 20, and 30 mm) and length of 50 mm in R-direction (or inclined R-direction, by an angle φ). The samples were cut at 95% RH for beech and at 85% RH for spruce and relocated for 4 weeks to 65% RH and 50% RH respectively. The samples were weighted and sample dimensions were measured in initial state, after reaching desorption equilibrium after 4 weeks in dry climate, and after oven-drying the samples for 48 hours at 103°C. Differential shrinkage coefficients were calculated as $\alpha = \varepsilon^\omega \Delta\omega^{-1}$ where ε^ω is the recorded shrinkage strain. The moisture contents ω were calculated as $\Delta\omega = (m_\omega - m_0)m_0^{-1}$ where m_ω and m_0 are the sample masses at moisture level ω and at oven-dry state.

Derivation of Probabilistic Model for α_R

The measured differential shrinkage coefficients (α^φ) are shown in Fig. 5.7 as a function of growth ring inclination φ . A linear and a strain tensor rotation model were fitted to the data and compared in order to correct for the inclination φ and to transform α^φ to coefficients in principal anatomical R-direction α_R , where $\varphi = 0$. The linear transformation, $\alpha^\varphi - 2(\alpha_T - \alpha_R)\pi^{-1}\varphi$, was chosen. A slightly skewed distribution of data points (Fig. 5.7C) resulted from the measurements of shrinkage coefficients. A two-parameter log-normal (\mathcal{LN}) and a three-parameter Burr type XII (\mathcal{BXII}) distribution were fitted to the transformed data α_R . A better fit was obtained using the Burr distribution as demonstrated by a Likelihood-ratio test shown in Tab. 5.2, which ruled out the effects of the additional fitting parameter. A value of $\mu_{\alpha_R} = 0.00178 \text{ \%}^{-1}$ with COV=7.56% was obtained for beech shrinkage and $\mu_{\alpha_R} = 0.00169 \text{ \%}^{-1}$ with COV=13.86% for spruce shrinkage, both characterized by the Burr type XII distribution with parameters as shown in Tab. 5.2. Results show a high variability in the derived probabilistic model. However, these results are in accordance with natural variability typically found in biological materials, especially in wood.

TABLE 5.2: **Statistical test results on differential swelling coefficient measurements.** Complementary to Fig. 5.7. Goodness of fit of linear regression and tensor rotation fit to data and parameters of fitted distributions to φ -corrected data. A likelihood-ratio test is used to compare fit of two PDFs having a different number of parameters. Values for beech (black font) and spruce (gray font).

Fit type	Data	Parameter 1	Parameter 2	Parameter 3	GOF ^a	μ_{a_R} (%-1)	σ_{a_R} (%-1 $\times 10^{-4}$)	COV ^b (%)
		a_R (%-1)	a_T (%-1)		SSE ^c (%-2 $\times 10^{-6}$)			
Linear regression	α^p	0.00178 0.00169	0.00318 0.00284		3.88 7.86			
Tensor rotation	α^p	0.00184 0.00175	0.00400 ^d 0.00330 ^d		4.03 8.37			
Log-normal distribution	a_R	$\lambda = -6.33$ $\lambda = -6.392$	$\zeta = 0.0793$ $\zeta = 0.159$		1528 899	0.00178 0.00169	1.42 2.72	7.94 16.03
Burr Type XII distribution	a_R	$\lambda = 0.00189$ $\lambda = 0.00189$	$c = 19.1$ $c = 10.2$	$k = 2.33$ $k = 2.47$	1537 914	0.00178 0.00169	1.35 2.35	7.56 13.86
Likelihood-ratio test ^f		G^2 ^g	C_α ^h		p -value ⁱ			
		18.44 29.09	7.815 7.815		3.568×10^{-4} 2.148×10^{-6}			

^a Goodness of fit; ^b Coefficient of variation; ^c Sum of squared errors
^d Preassigned values for physical meaning of tensor rotation
^e Abs. log-likelihood of maximizing parameters θ^{MLE}
^f Burr dist. fits data better if $G^2 = 2 |\log \mathcal{L}(\lambda, c, k) - \log \mathcal{L}(\lambda, \zeta)| > C_\alpha$
^g Statistic of test; ^h Test condition ($\sim \chi^2$) at significance level $\alpha = 0.05$; ⁱ Test confidence level

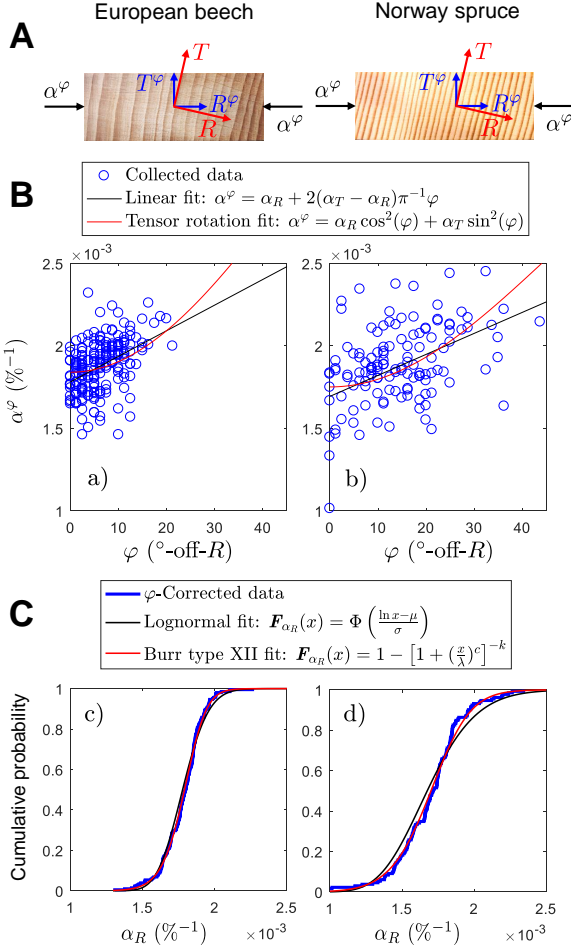


FIGURE 5.7: Statistical analysis of shrinkage coefficient. **A:** Scheme of material axes and measurement directions. **B:** Measured differential swelling coefficients α^φ vs. growth ring inclination φ for beech and spruce wood reference samples along best fit lines for linear regression (black line) and for strain tensor rotation (red line). **C:** Cumulative probability plot of corrected differential swelling coefficients α_R by linear regression to $\varphi = 0$ for reference samples along log-normal cumulative distribution fit (black line) and Burr cumulative distribution fit (red line).

INDUSTRIAL APPLICATION OF SELF-SHAPING WOOD

6.1 INTRODUCTION

The studies of chapters 4 and 5 [146, 153] were conducted with the aim of industrial and large-scale application of self-shaping wood as stated in the motivation of chapter 1. Findings of both studies significantly contributed towards the integration of wood bilayer production into an industrial framework, which was the goal of an *Innosuisse* project with a duration of 2.5 years conducted between 2017 and 2019. The project aimed not only at the integration of an alternative manufacturing process for production of curved timber elements, but also at the application in a real-life built structure for proof of concept and as a demonstrator of the capabilities of self-shaping wood. Therefore, in a combined effort between *Innosuisse* partners and partners from a project selected for the *Remstal Gartenschau 2019*, the *Urbach tower* project was developed and realized. The 14 m high Urbach tower (Fig. 6.1) represents the first structure worldwide made from self-shaped and load-bearing timber components at building-scale. Its design is based on the new self-shaping process of curved wood components developed in the frame of this thesis.

In contrast to the inherently reversible movement of wood bilayers as a function of moisture, the produced curved cross-laminated timber (CLT) elements are fully form-stable after a stacking-lamination. The required one-time deformation of wood bilayers is effectively frozen by the gluing of multiple bilayers on top of each other, such as shown in Fig. 5.1. Hereby, the freely swellable bottom edge of the bilayer's active layer, enabling the self-shaping, is hindered from any moisture-dependent movement by being glued to the next bilayer's top edge of passive layer.

This chapter is subdivided into three parts. Section 6.2 will describe the *Urbach tower* project for the sake of direct proof of concept and applicability of curved timber elements produced with the self-shaping method proposed in chapter 5. Section 6.3 will deal with the challenges and characterization of implementing the process in industry. Especially addressing sorting, monitoring, and assessment of variability in measured and predicted curvature of large-scale bilayer plates. Finally, section 6.4 will address and characterize the load-bearing behavior of self-shaped curved CLT elements.

Specifically, the quality of the stacking- and locking-lamination of two curved bilayers was hypothesized as being not suitable for structural applications. The potentially large thicknesses of the adhesive bond, due to the non-feasible planing and machining of the glued surfaces in the curved state, were of structural concern.



FIGURE 6.1: **The Urbach tower.** Worldwide first built application of form-stable self-shaping wood in Urbach, Germany, at the occasion of the *Remstal Gartenschau 2019*. (Photo credit (©): ICD/ITKE University of Stuttgart)

6.2 THE URBACH TOWER: PROJECT DESCRIPTION

The Urbach tower consists of 12 joined single-curved CLT lamellae that span up to 15 m. The lamellae were cut out from half-cylindrical curved sheets composed of elemental components, which attained their target curvature by self-shaping upon drying. The elemental components were spruce wood bilayers, made of wood regionally sourced from Switzerland, that were assembled in flat state as 5.0 x 1.20 m plates. After kiln-drying of the plates towards usage moisture content (MC), they achieved a radius of curvature of about 2.40 m (Fig. 6.2a). The curved plates were then assembled and stacked to form a half-cylinder-like shape (Fig. 6.2b and d), from which the lamellae were cut out and then detailed by a 5-axis CNC machine (Fig. 6.2c, e and f). The final curved CLT lay-up consisted of two glued bilayer plates of each 40 mm thickness (10 mm passive layer, 30 mm active layer), a 10 mm additional perpendicular locking layer, a water barrier foil, and a 15 mm larch facade cladding. The larch facade was coated with a durable and inorganic coating for protecting the wood against UV-induced decay and color changes [154]. The finished parts were transported to the construction site to be assembled in four groups of three pre-assembled lamellae in just a single day of assembly on-site.

The CLT load-bearing structure cantilevers over the 14 m height of the tower with a structural thickness of only 90 mm (40 mm + 40 mm + 10 mm). This results in a span-to-thickness ratio of approximately 160:1. The highly slender and lightweight structure is enabled by the tower's inherent surface-activeness due to the curvature and apparent twist of the lamellae in conjunction with the tower's cylindrical cross-section [155]. The curved CLT lamellae were connected by crossing-screws, whose arrangement throughout the structure was optimised by means of computational structural design tools. The structural concept and design is detailed in [155], the official project description can be found at [156], and additional technical information is given in Tab. 6.1.

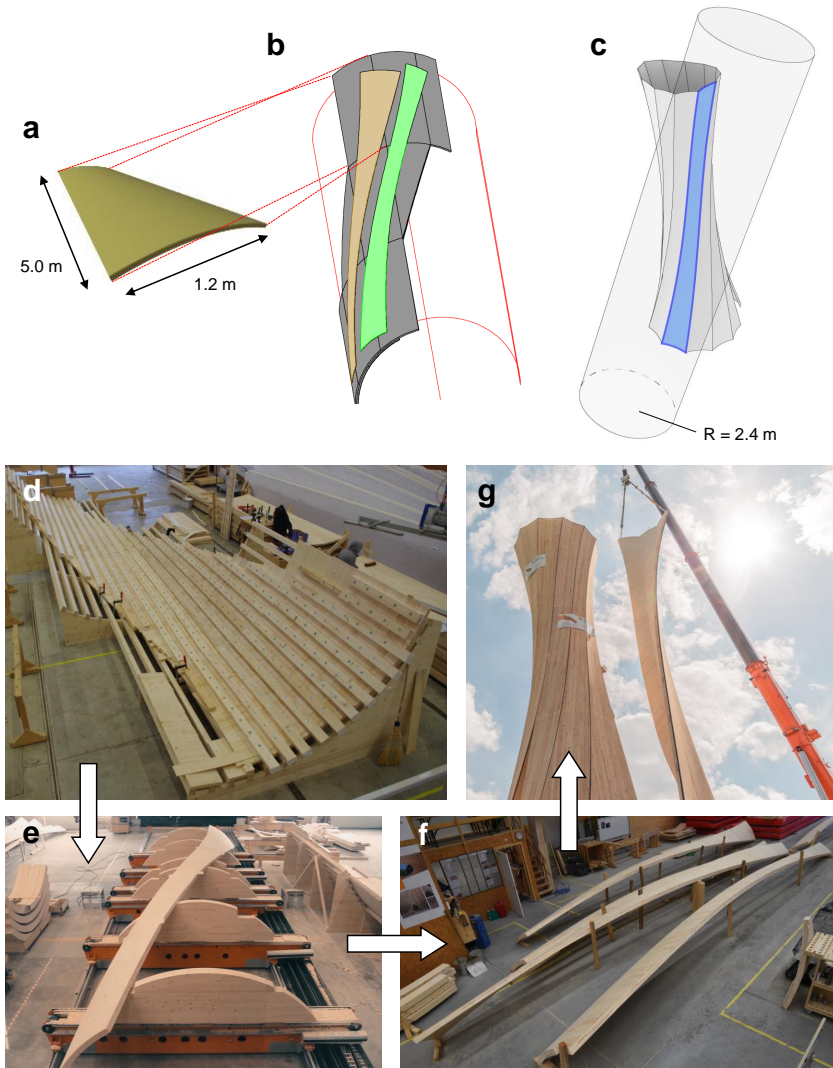


FIGURE 6.2: Urbach tower production process and assembly. **a** Self-shaped 5.0 m x 1.2 m wood bilayer plates as basic elements. **b** Assembly of basic elements to a half-cylinder for stacking-lamination. **c** Concept of diagonal lamella cutting along a single-curved cylinder. **d** Stacking-lamination by screw pressing. **e** Cut-out lamella before CNC milling. **f** Single lamellas after CNC milling. **g** On-site assembly. (Images credit (©): Empa, ICD/ITKE University of Stuttgart, Blumer-Lehmann AG)

TABLE 6.1: **Urbach tower technical information.** Source: [155].

Tower height	14 m
Tower diameter	4.9 m to 1.8 m to 3.1 m
CLT thickness	90 mm
Radius of curvature of CLT	2.4 m
Solid volume of structural timber	9.54 m ³
Surface area	106 m ²
Total weight of CLT structure	4000 Kg
Length of connection seams	157 m
Pairs of crossing-screws	520
CNC machining time	90 min/lamella
On-site assembly time	8 h

Project team

ICD University of Stuttgart: Dylan Wood, Achim Menges (Architectural design & self-forming curved wood components research and development). *ITKE, University of Stuttgart*: Simon Bechert, Lotte Aldinger, Jan Knippers (Structural design and engineering). *Applied Cellulose & Wood Materials, Empa / Wood Materials Science, ETH Zurich*: Philippe Grönquist, Markus Rüggeberg, Ingo Burgert (PI: Self-forming curved wood components research and development). *Lehmann Holzwerk AG & Blumer-Lehmann AG*: David Riggerbach, Katharina Lehmann (Wood manufacturing and construction & self-forming curved wood components research and development).

Project support

Innosuisse (Swiss innovation agency), *Deutsche Bundesstiftung Umwelt* (German federal environmental foundation), *University of Stuttgart*, *Gemeinde Urbach, Remstal Gartenschau 2019 GmbH*.

6.3 SELF-SHAPING MANUFACTURING PROCESS

The industrial production and shaping of the single 1.20 m by 5.00 m curved bilayer components (6.2a) was monitored with respect to MC change and curvature after drying. Hereafter, the data resulting from the manufacturing process is analyzed and discussed using the example of 31 curved elemental plates produced for the lamellas of the Urbach tower.

6.3.1 *Materials and methods*

Spruce wood bilayer plates of 1.2 m width and 5 m length were industrially produced at the sawmill of *Lehmann Holzwerk AG* to curve along the width direction. The manufacturing process is shown step by step in Fig. 6.3a. The Norway spruce wood came from the region of St.-Gallen, Switzerland, and the cut boards were graded into a C24 [157] strength class. Air-dried but high-MC active layer boards of 30 mm thickness, 10 cm width, and 5 m length were manually sorted by MC and standing annual ring orientation. They were then edge-glued using a single-component polyurethane glue (1cPUR, RP 2730 *Collano AG*). For each active layer plate, 12 boards were edge-glued together. Before gluing, MCs were recorded on each single board of the active layers with a capacitive wood moisture meter (*Brookhuis*) at depths of 10 and 15 mm and at 2 positions along the length. Passive layer boards of 10 mm thickness and MCs of $12\% \pm 2\%$ were then glued onto each active layer plate using 1cPUR adhesive. The flat bilayer plates were then technically dried in an industrial timber drying kiln (*Mühlböck Holztrocknungsanlagen GmbH*) at 60°C for 160 hours. Hereby, the conditioning step¹ was adapted in order to minimize the over-drying process. After drying, MCs in the active layer boards of each plate were measured again with the same procedure, resulting in 48 measurements per plate and in total, 1488 measurements. Finally, curvature of each of the 31 bilayer plate was determined by a three point arc-segment method as an average of measurements at the front and back sides of the plate. The target curvature of the plates, corresponding to the exact manufactured configuration and MC-difference, was predicted by numerical simulations using the procedures described in [153].

¹ In the conditioning step, the usually over-dried wood is backwards-conditioned to the (higher) target MC set by the regulating system [158].

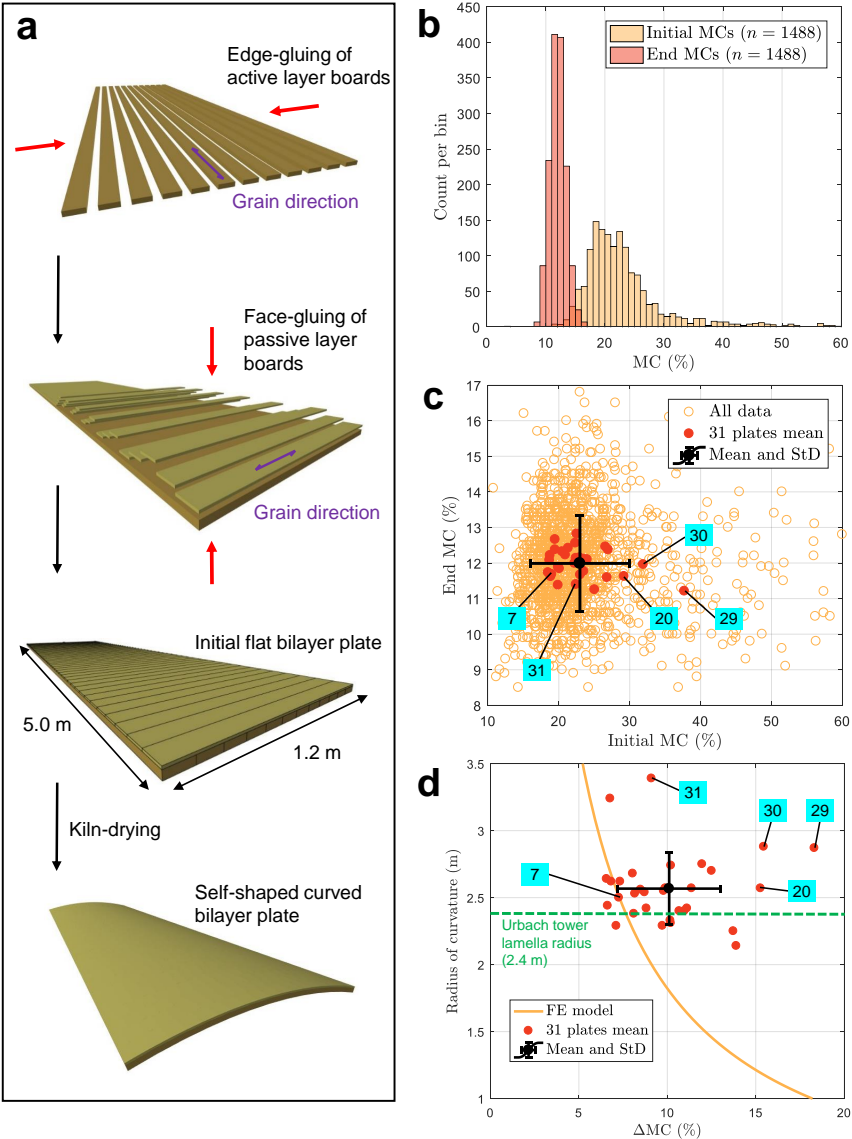


FIGURE 6.3: Self-shaping manufacturing process and monitoring. **a**: Schematic bilayer plate manufacturing. **b**: Distribution of MC-data of the active layers before and after kiln-drying. **c**: Start and end MCs of each single MC-measurement. **d**: MC-difference (corrected) plotted against radius of curvature, compared to FE model simulation. (Numbers in cyan boxes represent single plates shown in Fig. 6.4)

6.3.2 Results and discussion

The initial MCs of the active layer after air-drying and sorting reached a mean value with standard deviation (StD) of $22 \pm 8\%$ (Fig. 6.3b and c). It can be recognized that the spread of distribution is large, with a large amount of measurements above the speculated fibre saturation point (MC $> 33\%$), indicating strong initial gradients of MC in single boards. In fact, precise air-drying and homogeneous MC distribution along a single board is challenging to achieve in an industrial framework due to the constraint of space-saving outdoors stacking of fresh-sawn green-state boards in large piles. The MCs after kiln-drying showed a much narrower distribution with $12 \pm 1.3\%$. Here, the variability in MC is often caused by the specific position of a board inside the large kiln chamber, in which the generated climate is known to spatially vary during the drying process. However, a StD of 1.3% can also be caused by the inherent variability in wood structure alone, indicating a rather homogeneous and adequate drying process with respect to achieved variability.

The radius of curvature of 31 bilayer plates reached a value of 2.6 ± 0.5 m with a mean difference in MC of $10 \pm 3\%$ (Fig. 6.3d). The target radius of curvature proposed by the FE numerical simulation was, for that range of MC-difference, between 1.5 and 2.5 m. It can be recognized that most of the data points² scatter above the curve of simulation data³ and that therefore, radii achieved by industrial bilayer production are higher than their predicted radii. However, the scattering range of the points is large and intersects the model line, and therefore, an interpretation based on tendency is difficult. Nevertheless, it could be observed that points lying further away from the model-curve tend to correspond to plates with a very large initial spread in MC in the active layer, as shown for example for plates #20, 29, 30, and 31, marked in Fig. 6.3c and d, and separately shown in Fig. 6.4. Therefore, a narrow distribution of MCs in single plates is favorable in terms of predictability, which is underlined e.g. with plate #7.

2 Mean values of radii and MC-differences of the 31 plates where initial MCs were corrected to 33% if lying above in order to exclusively account for the hygroscopic range.

3 Notice: In Fig. 6.3d, the curve labelled "FE model" is shown as a continuous line. In reality, discrete points were modelled in regular intervals of MC=1% using a numerical model with high complexity [11, 153]. A second-order polynomial function with only two parameters, which is displayed in the graph instead of the discrete points fits the simulated data points perfectly ($R^2 \approx 1$).

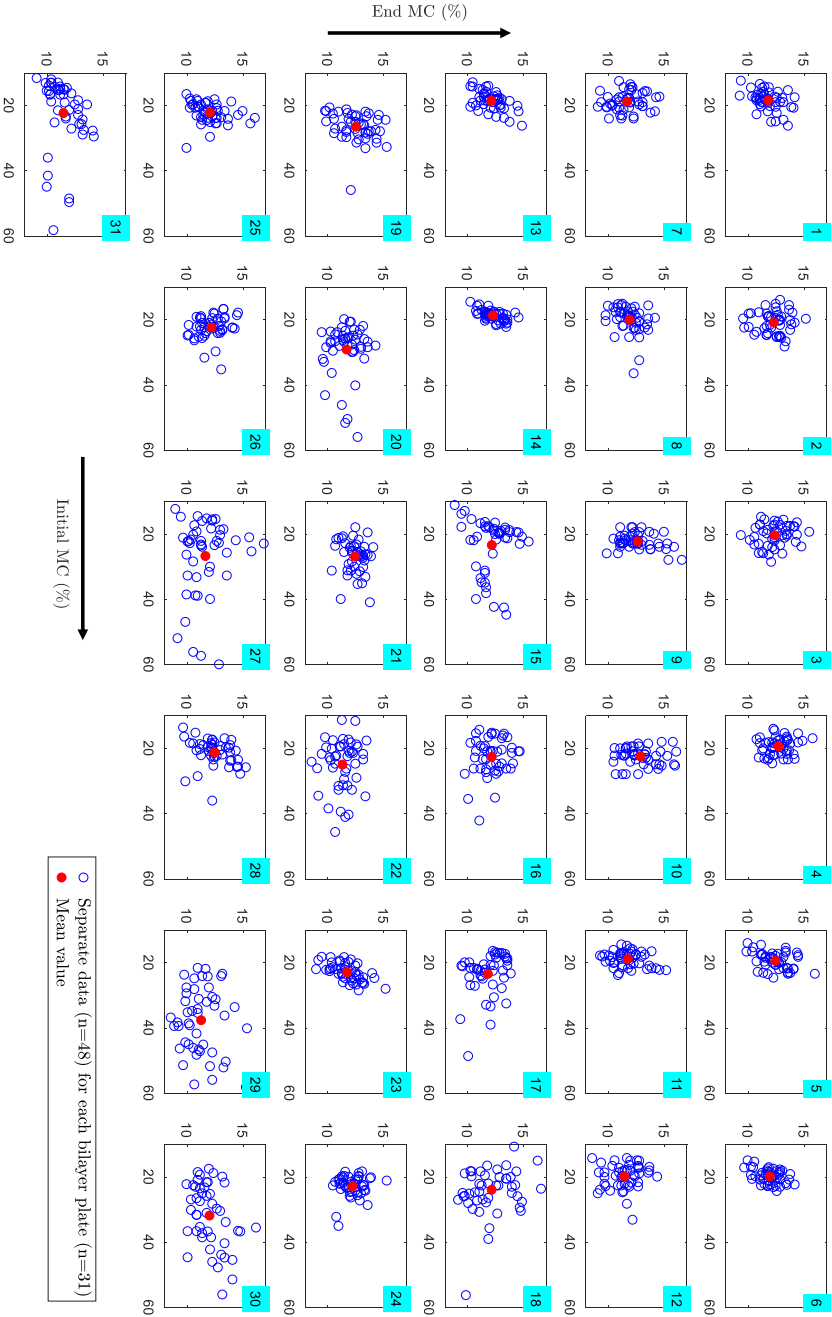


FIGURE 6.4: Moisture contents (MC) separated for each of the 31 bilayer plates. Initial MCs on horizontal axes, MCs after kiln-drying on vertical axes.

In the practical case of the Urbach tower, the spread in radii still was inside an acceptable range. Here, in order to laminate the curved plates together in the process of the locking lamination (shown Fig. 6.6a), both plates were pressed by screw-lamination onto blank beam supports of 2.40 m radius of curvature. The low bending stiffness along the plate's curved width-direction, since a 3/4-proportion of the thickness is wood transverse to the fibre direction, allowed for easily deforming the plates to the slightly lower radius. A decisive advantage of this process is that a guaranteed radius can be achieved, as there are practically no spring-back forces driving the parts to backwards deformation after the lamination process. In standard form-giving processes, these forces represent a major drawback as they can only be quantified in approximate manner [159], and setting a predictable target curvature required for the precise further automated milling-processing or assembly is challenging.

6.3.3 *Model over-estimation of spruce wood bilayers*

The observed over-estimation of curvature in the case of the industrially-produced spruce wood bilayers for the Urbach tower could also be observed previously at laboratory scale and with defect-free wood samples, as reported in [153]. Further investigations have been conducted in the frame of this thesis for better characterization of the predictability of the industrially relevant wood species Norway spruce. It was shown that the annual ring orientation in the active layer influences the predictability [160]. Best predictions (or lowest over-estimations) were achieved for perfectly standing annual rings. The highest over-estimations were observed in the range of an inclination of 30° from the standing configuration, whereas for configurations with 15° and 45° over-estimations were lower. In the same study, an influence of direction of annual ring pattern between active layer boards could be observed. Anti-symmetric (parallel) patterns of annual-rings of active layer boards resulted in best predictability, and at the same time, most homogeneous curvatures along the curving length. For the bi-layer plates of the Urbach tower, edge-gluing was conducted such that the plate contained no mirroring active layer boards. However, even though the active layer boards were sorted not only by quality and MC but also with respect to annual ring orientation targeted to be standing, a moderate variability in the latter could be observed in each of the 31 plates. Its effect on predictability of radius of curvature on industrial scale was not assessed. Mainly because at that scale, multiple additional effects might in-

terplay to affect curvature prediction. For example, minor cracks happened during drying procedure both in the active and passive layers. In addition, knots, tilted grain orientation along a board, local rot or fungi attack of the moist wood, or even poor quality of the adhesive bonding line cannot be avoided at this scale.

Since even at the laboratory scale, the overestimation of spruce bilayers could not yet be explained, such large-scale effects were given less priority. Further investigations conducted at laboratory scale, measuring precise strain field development in the active layers over time by digital image correlation techniques, have supported this setting of priorities [161]. In the study of [161], it was revealed that the model overestimation in the case of different configurations of spruce wood bilayers is likely due to a poor shear transfer that could be experimentally observed in the wood of the active layers in zones near the interface, but that was not observed in the corresponding strain fields of the FE models. A valid explanation for these observations has not been found yet. Most probable hypotheses are a local non-linear elastic shear behavior in the spruce early-wood, and a stress- and moisture-dependency of hygro-expansion parameters. In contrast, it was shown in a previous numerical study that prediction of curvature is independent of complex deformation mechanisms. In fact, adding visco-elasticity, mechano-sorption, or plasticity deformation modes in addition to exclusively elasticity did not affect curvature [162].

6.3.4 *Summary*

Industrial production of large-scale spruce wood bilayer plates was successfully realized. The built and investigated plates were used as basic elements for 15 m long lamellas for the Urbach tower. The spread in curvature of the plates could be kept narrow enough to allow a precise target radius of curvature of 2.4 m after a stacking- and form-locking lamination of two plates onto each other. No spring-back effects resulted during the procedure, making it more predictive than standard cold-pressing for achieving curved timber structures. The apparent over-estimation of the FE model with respect to the industrially produced large-scale plates are attributed to the interplay of numerous complex global and local effects such as high initial spread in MC, quality of wood, and annual ring orientation. However, unresolved issues at the laboratory scale such as non-captured mechanical effects in the model, which supposedly impact shear transfer in early-wood of the active layers near the interface, still play a role, also at

the industrial scale. The high initial spread in MC can be reduced in future applications if custom-adaption of kiln-drying chambers would be made possible in order to dry from green states to the high initial MCs with high reliability. This would by-pass the initially uneven air drying and manual sorting of the boards by MC, thereby reducing an important uncertainty with respect to predictability of curvature.

6.4 STRUCTURAL TESTING

The structural elements of the Urbach tower consist of 90 mm thick curved CLT elements. This lay-up was realized by stack-lamination of two bilayer plates and a 10 mm additional layer as described previously and depicted in Fig. 6.6. Uncertainties with respect to load bearing behavior of these CLT elements arise with the consideration that the residual stress state of the self-shaping of the bilayers might negatively impact bending strength and stiffness. It is not known, how these high residual stresses affect structural behavior when superimposed with externally induced stresses. Even though such residual stresses are also present for conventional cold-bent curved lamella laminations [163], the stress state at the intra-bilayer adhesive interfaces is different with the self-shaping method. In addition, the glue joint between bilayer plates, glued in curved state without planing beforehand, might be of reduced quality because of the increased gap thickness. In order to address both issues, structural characterization tests, namely a three-point bending and a block-shear test, were conducted in order to assess the load-bearing behavior after the stack-lamination. Specifically, a gap-filling and custom-tailored two-component polyurethane (2cPUR) adhesive was tested against a standard 1cPUR adhesive, both for the three-point bending and the block-shear tests. The used 2cPUR adhesive consists of a polyol and an isocyanate component, and in contrast to 1cPUR, possesses a high cohesive strength suitable for thick gluelines, but is not yet officially accredited for structural applications [164].

6.4.1 *Materials and methods*

6.4.1.1 *Three-point bending test*

Self-shaped CLT samples ($n = 20$) of lay-up 10/30 mm (bilayer) + 10/30 mm (bilayer) + 10 (cold-bent) mm (as shown in Fig. 6.6a), with total thicknesses of 90 mm, lengths of 1.20 m, and widths of 18 cm were subjected to a three-point bending test. The samples had a radius of curvature of 3 m and were cut sequentially from a self-shaped stack-laminated CLT plate made out of C24 strength-graded boards. The inter-bilayer lamination was conducted using 1cPUR adhesive (*Collano AG*) for 10 samples, and a 2cPUR gap-filling adhesive (*Collano AG*, for details see [164]) for another 10. At the moment of testing, the samples were approximately acclimatized to 50% relative humidity and 20°C. The test setup was designed

as statically determinate system and consisted of one fixed and one sliding support, and between them, a span of 1.0 m (Figs. 6.5a and 6.6b). The rotational degree of freedom at the supports was provided by metallic hinged plates glued onto beech laminated veneer lumber (LVL) blocks of dimensions 20x20x5 cm, which were screwed to the samples with six metallic screws at each support. The screws penetrated the samples vertically by 7 cm from below and thus acted as shear reinforcements at the support region in order to avoid shear failure. The sliding support was enabled by two greased metallic sliding plates below the support. In order to design the custom-built test setup with respect to occurring forces and displacements, the load bearing behavior was approximated beforehand by 3D FE simulations using a linear elastic and orthotropic material law for spruce wood for the exact geometry of the test specimens, which was defined by industrial production constraints at the sawmill. The samples were loaded at mid-span with a rounded steel block pressing onto a 10x18x2 cm beech LVL plate for load distribution into the samples. The steel pressing block was connected via a load registering cell to a suspended steel I-profile connecting two pulling oil-hydraulic cylinders from each side, which were fixed to the ground. The load (F) was applied by simultaneously regulating oil pressure in both cylinders and the resulting vertical displacements (v) of the samples were measured below the samples at mid-span with a suspended linear variable differential transformer. The samples were loaded until failure inside a time-span of 120 seconds.

6.4.1.2 Calculation of global bending strength and stiffness

The global bending strength f_b was calculated for each sample as the bending stress at failure:

$$f_b = \frac{M_{max}}{I} y = \frac{3F_{max}l}{2bh^2}, \quad (6.1)$$

where F_{max} represents the maximal force reached at failure of the samples and $M_{max} = F_{max}l/4$ the bending moment at failure. The symbols l , b , and h stand for span, width, and thickness of the samples. I is the beam's second moment of area, and for a quadratic cross-section, $I = h^3b/12$. The above equality assumes that the neutral axis situates at half of the beam thickness, such that the distance to the neutral axes is $y = h/2$, following recommendations of DIN 52186 [165] for wood.

The global bending stiffness of the curved beam can be found by first formulating an expression for the beam deflection using the principle of

virtual work by following a general theory of structures [166]. Hereby, the system's external work equals its internal work. Therefore, with introduction of the adequate virtual system, the sum of virtual external forces times the real (unknown) displacements must equal the sum of virtual internal forces times the real internal deformations. Applied to the curved beam system in Fig. 6.5, the formulation reads:

$$vF^v = \int_0^{\theta/2} \frac{M^r M^v}{E_b I} R d\varphi + \int_0^{\theta/2} \frac{V^r V^v}{GA} R d\varphi + \int_0^{\theta/2} \frac{N^r N^v}{E_n A} R d\varphi. \quad (6.2)$$

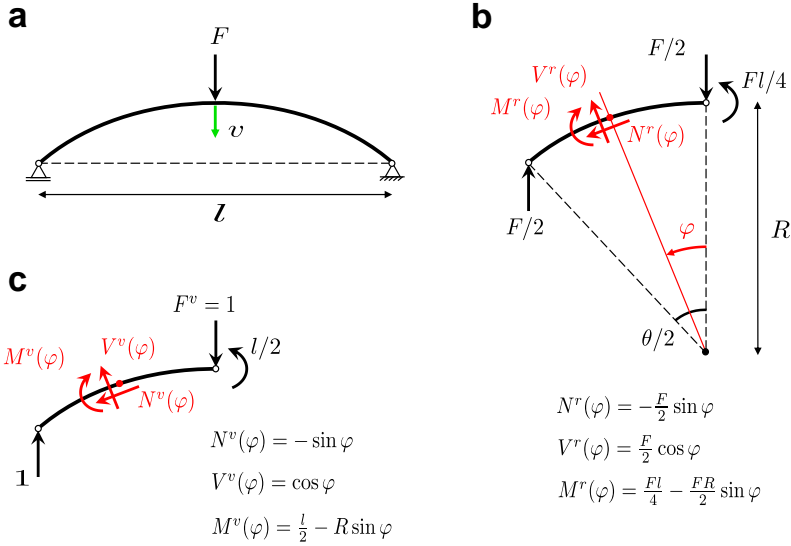


FIGURE 6.5: **Structural system for a simply supported curved beam.** **a:** Beam with radius of curvature R , supported by a pin and a sliding support, displaying deflection v while loaded in the middle by a force F . **b:** Replacement equivalent structural system with half-opening angle $\theta/2$. **c:** Virtual equivalent structural system with virtual external force and internal forces.

Hereby, the (real) curved beam deflection v is directly expressed, as the external virtual force $F^v = 1$. Further, R is the radius of curvature of the beam, θ is the opening angle from one support to the other, φ is the path-variable along θ , and the symbols M , V , and N stand for internal moments, shear, and normal forces with superscripts r and v denoting origin from

the real and the virtual system as shown in Fig. 6.5b and c. Further, E_b is the unknown global bending stiffness and G and E_n are stiffnesses of the beam under shear and under normal forces. By neglecting the two last terms in Eq. 6.2 since their contribution is assumed to be small⁴, and by reformulating, the expression of the global bending stiffness of the curved beam reads:

$$E_b = \frac{F}{v} \frac{R}{2I} \int_0^{\theta/2} \left(\frac{l}{2} - R \sin \varphi \right)^2 d\varphi. \quad (6.3)$$

For simplicity, it is assumed that the span l and the radius of curvature R of the beam remain constant in the range of the measured F - v data. For the tested beam samples described above, the term F/v was derived as the slope of a straight line fitted in the force (F) -displacement (v) diagram between values of 10% and 40% of F_{max} . The half-opening angle $\theta/2$ of the beam between the two supports was calculated using the arc chord-length expression $l = 2R \sin(\theta/2)$, with $l = 1$ m and $R = 3$ m, resulting in $\theta/2 = 0.1674$ rad.

6.4.1.3 Block-shear test

Block samples (50 x 50 x 50 mm) were cut out in representative manner from twin samples of the self-shaped CLT samples tested by three-point bending. For each of both adhesives used for the locking-lamination step (Fig. 6.6a), 30 samples were prepared such that the joint of interest was exactly at the middle of each sample and straightly aligned with the edges. The tests were conducted by using a universal testing machine (Zwick Roell, shown in Fig. 6.6c) in displacement-controlled mode with 2 mm/min and following *DIN 52187* [167]. The samples were loaded until failure and block-shear strength was determined according to *DIN EN 16351* [168] as the force at failure divided by the sheared area.

6.4.2 Results and discussion

The results of the three point bending tests are displayed in Fig. 6.6b. In the load-deflection graph, no apparent difference between samples laminated with 1cPUR or 2cPUR can be observed. The samples failed at a force of

⁴ Owing to the fact that the system is statically determinate, that squared cos and sin terms are assumed negligible, and that the radius of curvature R of the beam is large compared to the span l . Further, non-trivial assumptions on global shear modulus G and global stiffness to normal forces E_n would need to be made in the other case.

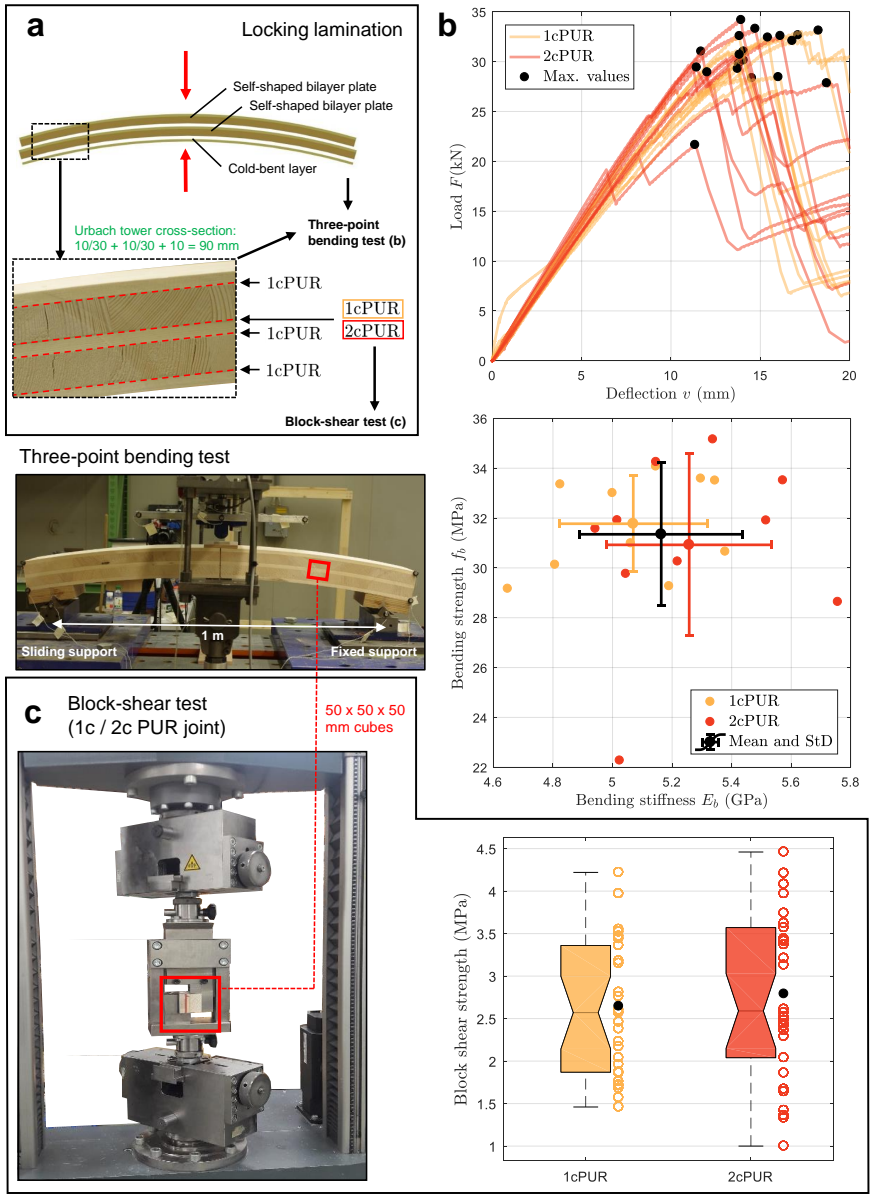


FIGURE 6.6: Structural testing of self-shaped CLT. **a:** Setup of locking- or stacking-lamination procedure and overview of used adhesives per glue joint. **b:** Image of three-point bending test setup and results: Load-deflection graph and global bending strength-stiffness graph. **c:** Image of block-shear test setup and results (black dots represent mean values and circles are single data points).

around 30 kN and a vertical displacement of about 15 mm. After failure, samples showed a remaining lifting capacity between 5 - 15 kN. In the graph of global bending strength versus stiffness, a slight but not significant tendency can be observed towards samples laminated with 1cPUR reaching higher values of bending strength but lower values of bending stiffness. However, a single outlier in the 2cPUR samples might have influenced the reduced average in bending strength. Generally, high global bending strengths were reached, with a mean value of 31.5 MPa. This corresponds to a characteristic global bending strength of 25.7 MPa, which is calculated as the lower 5% quantile value of a lognormal distribution fit to the data according to *DIN EN 14358* [169]. Therefore, rather than reducing material properties for design due to the residual stress state of shaping⁵, it is more straightforward to assign a specific strength grade, here e.g. C24, according to *DIN EN 1995 (Eurocode 5)* [157], which is also the initial strength grade of the sorted boards prior to self-shaping. In the case of the strength, global and local values do not supposedly show high differences, and therefore, strength grades can be assigned. However, this is not the case for the bending stiffness. In fact, the global bending stiffness of the tested samples reached a mean value of about 5.15 GPa, which is lower by approximately a factor of 2-3 compared to local characteristic bending stiffness for the corresponding strength grade (C24). Here, local values, i.e. for single parallel and perpendicular grain-oriented lamellae, would need to be backwards-calculated using the test data. However, the structure's stiffness is usually required as a global value in the frame dimensioning, e.g. of a structure's serviceability. Furthermore, in applied structures, the observed a-priori low bending stiffness can be compensated by fixed and stiff supports where horizontal displacements are prevented in order to activate the arching-action effect of the curved beams or plates.

In the above presented procedure for the calculation of the bending stiffness, the horizontal deformation of the beams was not considered. An additional stiffness formulation (e.g. Eq. 6.3) in terms of horizontal deformation could lead to a set of two equations for the principle of virtual work, and therefore, these could be solved in terms of an additional unknown, the global shear moduli. The deflection contributions from global

⁵ Note that in this case, under three-point bending, the residual axial stresses of self-shaping act as an internal pre-stressing at the edges of the beams. For example, the top edge is under tension after the self-shaping, whereas compression is induced under the external bending load. If desired, the influence of initial residual stresses could be assessed by numerical modelling for a given custom external loading in terms of inverse fitting with respect to the deformation behavior.

shear and global bending could thus be separated from each other, which would be expected to raise the value of pure global bending stiffness due to the presumed low shear stiffness because of rolling shear in the transverse layers.

In the tested setup, the thickness-to-span ratio was small (1 : 11.1) due to production constraints. Because of high shear regions at the supports under three-point bending, the vertical screws connecting the support plates served as shear reinforcements. In fact, no shear failure at the support region was observed and the general failure mode was bending and rolling shear around the region of point transmission of the applied force. Additionally, and corresponding to the values of bending strength and stiffness, no significant difference in failure mode between samples of the two adhesive categories could be observed, leading to the conclusion that in terms of load-bearing behavior under bending there is no difference with respect to the adhesive used for the locking lamination. Overall, similar findings and conclusions apply to the case of self-shaped CLT beams as in the case of conventionally curved CLT beams, which obtained a *European Technical Approval* in [163]. However, the level of validity of the herein presented results should be considered with respect to the low number of tested samples ($n = 20$).

The results of the block-shear tests are shown in Fig. 6.6c. The mean values of block-shear strength of the glue joints are around 2.7 MPa with no significant⁶ difference between 1cPUR and 2cPUR samples. However, a slightly higher variability is observed for the 2cPUR samples and in general, standard deviations are high. Nevertheless, both adhesives reached values above the required block-shear strength of 1.4 MPa as stated in *DIN EN 16351* [168] for spruce CLT structural elements. For both adhesives, gap thicknesses were approximately uniformly distributed in the range of 0.1 - 3 mm. However, for all the samples, even the 1cPUR samples, only wood failure was observed, which means that the portion of lower values of block-shear strength can be attributed to failure in rolling shear. Overall, even though no statistical difference can be observed between 1cPUR and 2cPUR samples, both are able to fulfill static structural requirements⁷ in spite of the large gaps. Therefore, the large gaps resulting from the lack of

6 Notched boxplots, as shown in Fig. 6.6c, allow for direct visual inference of statistical significance. The part of the box that is notched represents the 95% confidence level interval of the median of the data set. Therefore, if the notches of two boxplots do not overlap, both medians of the data sets supposedly show a difference that is statistically significant.

7 Excluding delamination tests.

processing possibilities of self-shaped curved bilayers before the stacking-lamination are not of structural concern.

6.4.3 *Summary*

Both a three-point bending and a block-shear test on samples stack laminated with either 1cPUR or 2cPUR did not show significant difference in load-bearing behavior. Therefore, a custom gap-filling adhesive such as the 2cPUR is not required for static structural applications of self-shaped CLT elements where concerns arise with respect to the large gaps of the stacking and locking lamination of curved bilayer parts. Structurally, self-shaped curved CLT, despite the residual stress state of shaping, appears to perform in comparable manner to conventional CLT timber in terms of fulfilling normative standards. However, the initially graded wood's strength class at the sawmill might not correspond to the final curved CLT element's strength grading after production, likewise as in conventionally cold-bent curved CLT.

HYGROMORPHIC SELF-SHAPING WOOD GRIDSHELL STRUCTURES

7.1 PUBLICATION PREAMBLE

Computational analysis of hygromorphic self-shaping wood gridshell structures

Philippe Grönquist^{1,2}, Prijanthy Pandchadcharam², Dylan Wood³,
 Mohammad M. Hassani², Achim Menges³, Markus Rüggeberg^{1,2}, Falk K.
 Wittel²

¹ Empa, Laboratory for Cellulose & Wood Materials, 8600 Dübendorf, Switzerland

² ETH Zurich, Institute for Building Materials, 8093 Zürich, Switzerland

³ University of Stuttgart, Institute for Computational Design and Construction, 70174
 Stuttgart, Germany

Preprint submitted to *Royal Society Open Science* on 18 December 2019

Author contributions: Conceptualization, PG; methodology, PG and FKW; formal analysis, PG and PP; writing–original draft preparation, PG; writing–review and editing, PG, PP, DW, AM, MR, FKW; visualization, PG and DW; supervision, PG, DW, AM, MR, FKW; funding acquisition, MR.

Key findings

- A way of overcoming the limitation of shaping of anisotropic self-shaping cross-ply laminate plates and to achieve double-curved structures is presented in the form of gridshell systems composed of narrow self-shaping strips.
- The phase-space of curvature of self-shaping wood gridshells is analyzed by parametric computational models and shows dependency on strip geometry.
- Self-shaping timber gridshells represent a beneficial alternative in terms of erection procedure compared to conventional active-bent gridshells.

Abstract

Bi-layered composites capable of extensive self-shaping are of increasing relevance to science and engineering. Such composites can be made out of anisotropic materials that are responsive to changes in a state variable, e.g. wood, which swells and shrinks due to changes in moisture. When extensive bending is desired, such bilayers are usually designed as cross-ply structures. However, the nature of cross-ply laminates tends to prevent effective changes of the Gaussian curvature so that a plate-like geometry of the composite will be partly restricted from shaping. Therefore, the most effective approach for maximizing bending is to keep the composite in a narrow strip configuration so that Gaussian curvature remains constant during shaping. This represents a fundamental limitation for many applications where self-shaped double-curved structures could be beneficial, e.g. in timber architecture. In this study, we propose to achieve double-curved structures by a gridshell configuration of narrow self-shaping bilayer strips. Using numerical mechanical simulations, we investigate the phase-space of shaping for self-shaping wood gridshells. We show that double curvature can be achieved and that the corresponding change in Gaussian curvature is dependent on the system's geometry. Furthermore, we discuss a novel application potential in the form of self-erecting timber gridshells for architecture.

7.2 INTRODUCTION

Programmable self-shaping materials are widely studied, e.g. at small scale in fields such as soft robotics [47, 52, 170–174], or at medium and large scale mostly for adaptive structures in construction applications [8, 66, 67, 69, 175, 176]. A commonly known principle of obtaining self-shaping systems is the bilayer-laminate. A residual stress state, responsible for the shaping, can be obtained by two bonded materials with different expansion or retraction properties with respect to a controllable state-variable such as the moisture content [146, 177]. In the case of narrow bilayer strips, the resulting differential strain (ε_0 , or stretch $\lambda_0 = \varepsilon_0 + 1$) across the thickness (h) direction is directly proportional to the induced curvature of shaping ($\kappa_0 = h^{-1}\varepsilon_0$). This type of curvature is often termed natural curvature [14, 15] since in quasi-2D configuration, bilayer strips are free from shaping restrictions of plate-like geometries such as shown in Fig. 7.1. For plate geometries, the shaping can be very complex especially for anisotropic composites, e.g. a laminate of two plies of the same material with different fiber or strong direction with respect to each-other. Often, a cross-ply structure is chosen, which is maximizing the amount of differential strain. However, such configurations tend to exclusively achieve saddle-like shapes, similar to the example in Fig. 7.1b. The reason is that cross-ply structures of stiff anisotropic composites prevent significant in-plane stretching, which results in very limited and negative changes in Gaussian curvature $K = \kappa_1\kappa_2$; the product of curvatures along two principal directions 1 and 2. To achieve large changes in K , such non-isometric deformations usually strive towards a coupled bending and in-plane stretching [14, 15, 61]. Excluded are composites with programmable stability effects, e.g. bi-stable snapping systems [59, 178, 179].

New applications for anisotropic self-shaping composites would be made possible by structures that, in contrast, allow $\Delta K > 0$. This could include for example initially flat structures self-shaping towards dome-like shells. One of the most suitable materials for self-shaping applications at medium- and large-scale is wood [153, 180]. Wood is a material that can readily be applied as a self-shaping composite thanks to its innate capacity of anisotropic swelling and shrinkage and does not need any modification or complicate synthesis [7]. In addition, it is a common and low-cost construction material with unrivaled environmental virtues such as full renewability, low embodied energy, and natural degradability. However, similar to the case of anisotropic shaping composites mentioned above, self-shaping

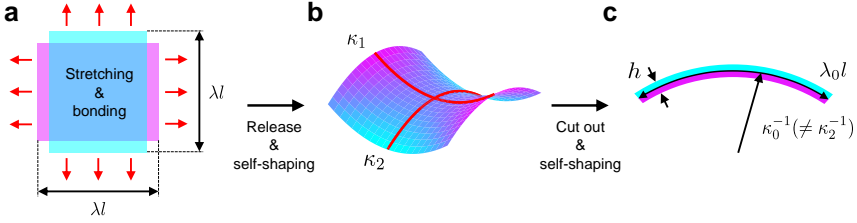


FIGURE 7.1: **Curvatures of a bilayer-composite.** **a:** Two elastic sheets of thickness $h/2$ are stretched by a factor of λ and then bonded together. The same configuration is achievable by first bonding two stimuli responsive layers together and inducing λ with the stimuli, e.g. a moisture-content change in wood will result in anisotropic swelling- or shrinkage-induced stretches in the single layers. **b:** Upon release, the bilayer-composite plate-like sheet self-shapes into an exemplary saddle configuration with principal curvatures κ_1 and κ_2 . **c:** A narrow quasi-2D strip cut out from the sheet displays natural curvature κ_0 and stretch λ_0 (On the basis of [14, 15]).

bilayer plates made out of wood typically adopt a saddle-like configuration and thus suffer from the above mentioned restriction $\Delta K < 0$ [67, 68].

In this study, we show a way to overcome the mentioned limitations by self-shaping gridshell systems (see movie S1, Fig. 7.5), focusing on orthogonal and interconnected narrow wood bilayer strips. Each wood bilayer strip will thrive towards shaping to its natural curvature when the humidity is changed, and ideally, the gridshell system will realize a shape where $\Delta K > 0$. However, the system's behavior, especially the exerted effect of rigid interconnections on the shaping, is yet unknown. In this context, we analyze the self-shaping behavior of wood gridshell structures at medium scale by parametric numerical studies using the Finite Element (FE) method. By investigating principal curvatures, natural curvatures, mean and Gaussian curvatures, we quantify and discuss the phase-space-dependent shaping behavior and draw relevant conclusions for application to self-assembly architecture and construction processes. For such applications, gridshell systems offer a lightweight and material efficient method of covering large spaces with structurally performative curved forms [181–187].

7.3 METHODS

Self-shaping wood bilayer 3x3 gridshells with 0.5 m long strips were modelled using the FE method with the commercial software *Abaqus 6.14*. The model was set up by parametric *Python* scripting, which allowed for covering a wide parameter space. The developed automatic computational framework is described in supplementary Fig. 7.6. The moisture change, from 20% to 12% WMC, inducing the shaping, was modelled by a steady-state change in field variable with automatic incrementation and with a non-linear-geometry static analysis. The model was meshed with quadratic brick elements with reduced integration and 2x2x2 integration points. A single bilayer strip is composed of a passive layer (PL) with thickness h_1 and width w tied to an active layer (AL) of thickness h_2 . The three local wood anatomical directions, radial (R), tangential (T), and longitudinal (L) were assigned to the PL and AL as shown in Fig. 7.2 so that the wood fiber direction L corresponded to the strip direction in the PL and to the perpendicular direction (in the grid-plane) in the AL. The interaction of the strips was modelled by a surface-to-surface contact (finite sliding, no tangential friction, normal separation enabled). Further, the strips were tied together by a wire-line with hinge-connector properties (rotational degree of freedom about the grid out-of-plane axis), which was coupled to the inner surface of cylindrical holes of 2 mm in diameter through the middle of the strips (distributed coupling) through reference points. This setup represents no-slip metallic screw-connections between the strips of the grid and was chosen to avoid further contact problems in the model. The grid is held by a vertical support and a pin at the extremities of a single mid-strip.

The wood species European beech (*Fagus sylvatica* L.) was modelled as a linear hygro-elastic and orthotropic material with distinct material properties in directions R, T, and L, and dependent on WMC, denoted ω . The nine independent engineering constants of the fourth-order elastic stiffness tensor \mathbf{C}^{el} are shown in supplementary Table 7.1. The hygro-expansion and retraction coefficients α_i used in the analyses, also termed differential swelling and shrinkage coefficients, were chosen as $\alpha_R = 0.0019$, $\alpha_T = 0.0040$, and $\alpha_L = 0.0001$ in units of $\%^{-1}$ [100, 153]. The parameters α_i represent elements in the diagonal hygro-expansion coefficient tensor $\boldsymbol{\alpha}$. The overall material behavior is characterized by the free energy function

$$\Psi = \frac{1}{2} \boldsymbol{\varepsilon}^{el} : \mathbf{C}^{el} : \boldsymbol{\varepsilon}^{el}, \quad (7.1)$$

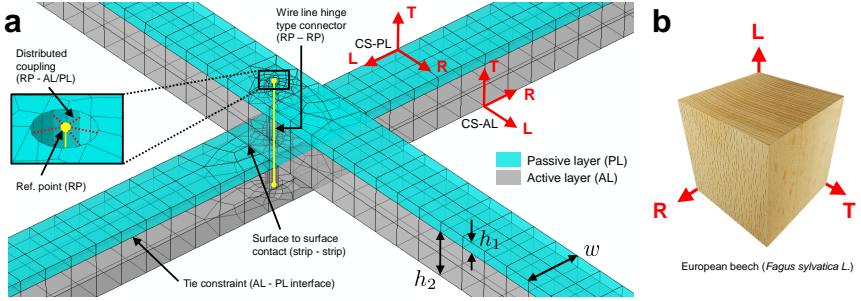


FIGURE 7.2: **Gridshell FE model setup.** **a:** Detail of FE model at strip intersection with parameters h_1 , h_2 , and w . Local orthotropic coordinate systems (CS) R, T, and L assigned to passive and active layers (PL and AL) of strips. **b:** Local anatomical directions R, T, and L visualized on a macroscopic cube of European beech wood.

where the Cauchy stress tensor σ is derived from the material law as

$$\sigma = \frac{\partial \Psi}{\partial \epsilon^{tot}} = C^{el} : (\epsilon^{tot} - \epsilon^{\omega}) = C^{el} : \epsilon^{el}. \quad (7.2)$$

Hereby, the total strain tensor calculates as $\epsilon^{tot} = \epsilon^{el} + \epsilon^{\omega}$ and the hygro-expansion strain tensor is $\epsilon^{\omega} = \alpha d\omega$ for a moisture increment $d\omega$.

Curvatures κ_1 and κ_2 along directions 1 and 2 (see coordinate system in Fig. 7.3) were calculated by automatic retrieving of coordinate lines on the deformed mid-strips by the inverse of radii of circles fitted to the coordinate lines. Respective natural curvatures κ_0 of the strips were calculated by 2D plane stress FE models of single strips with setup and boundary conditions matching the above description.

7.4 RESULTS AND DISCUSSION

Self-shaping gridshells, half a meter wide and composed of 3×3 intersecting wood bilayer strips made out of European beech were investigated. In a 3×3 grid, rigid-body and symmetric angle changes between the strips are prevented, and the system serves as an elementary representative of a rigidly interconnected larger grid. The gridshells were modelled to start in a flat state at an initially high wood moisture content (WMC) of 20%, and then shape while drying to 12% WMC. This roughly corresponds to conditioning the wood at 80% and 50% relative humidity climates at 20°C [188].

Both the thickness h and the width w of the strips were varied inside an interval of 5 to 25 and 5 to 45 mm. The boundaries of h and w were chosen as to represent application-based and feasible configurations at the medium-scale for a proof of concept. In fact, wood strips with $h, w < 5$ mm ($h_1 = 1$ and $h_2 = 4$ mm) are difficult to efficiently machine and $h > 25$ mm and $w > 45$ mm already represent building-scale dimensions. The ratio $h_1 : h_2$ was constantly maintained to be 1:4, which for beech wood approximately corresponds to the ratio maximizing the natural curvature and minimizing elastic energy [146]. Curvatures of the gridshell configurations after self-shaping by drying are shown in Fig. 7.3 along the initial and deformed states of the grids at the extremities of the phase-space (configurations A, B, C, and D) for both simulated and experimental samples.

The graphs of the middle-strip gridshell curvatures κ_1 and κ_2 show that narrower strips and lower thicknesses result in increasingly curved gridshells. E.g., configuration A reaches $\kappa_1 = \kappa_2 = 3.2 \text{ m}^{-1}$, which corresponds to a radius of curvature of approximately 31 cm. A change in shaping mode can be observed for $h = 5$ mm at $w \approx 30$ mm. The gridshell curvature κ_1 is zero for $w < 30$ mm while κ_2 is high. This behavior is inverted abruptly for $w > 30$ mm. The gridshells B and C illustrate this phenomenon. This behavior can be explained by the fact that in either mode (B and C) the system's energetic cost of restraining the whole set of strips along a certain axis and allowing the other strips (along the other axis) to freely bend is lower than restraining both κ_1 and κ_2 to be $< \kappa_0$. The fact that these modes apparently depend on w for $h = 5$ mm but not for $h > 5$ mm can be explained by the strongly increasing contribution of h on the residual elastic energy of shaping [146]. This implies a transition from w to h in dictating morphogenesis. In addition, the shaping of single strips is known to increase with a thickness ratio $h_1 : h_2$ close to the optimal ratio [146]. However, it can be observed here that the shaping of the gridshells is prevented by an increasing width because of rigid restraints at the screw joints of the strips. In fact, at lower values of h , thinner strips tend to bend in-plane and thus allow the rigid screw connections to spatially slip with respect to each other, on an imaginary shell plate surface. This allows for the system to realize a coupled bending and in-plane stretch for increased overall change in K . The in-plane bending of a border strip from configuration A is visualized in supplementary Fig. 7.7 for both computational and physical models. The physical models built for validation show similar magnitude of shaping and same shaping mechanism as the numerical models.

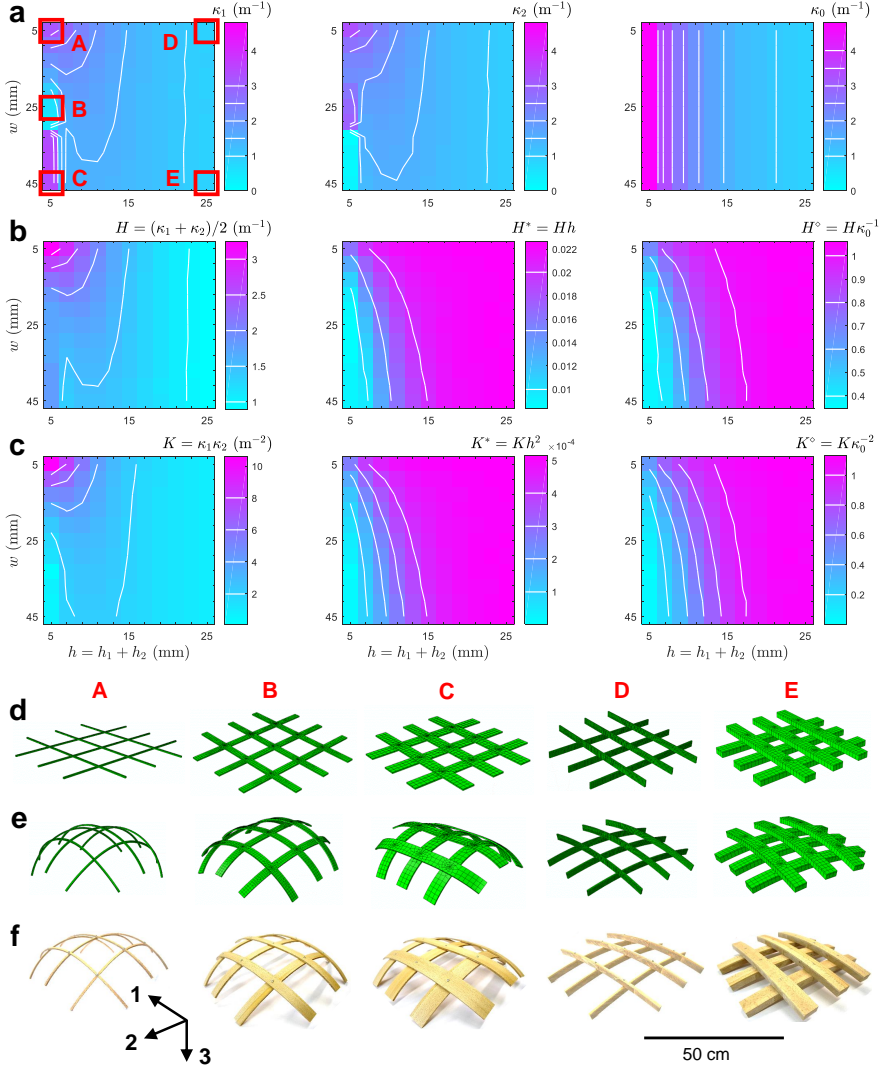


FIGURE 7.3: Phase space of gridshell curvatures after self-shaping in dependence of width w and thickness h for 121 (11x11) Finite Element model solutions. **a:** Curvatures along middle strips in directions 1 and 2 (κ_1 and κ_2) and natural curvatures κ_0 . A, B, C, D, E denote configurations at extremities of analyzed phase space. **b:** Mean curvatures H , and mean dimensionless curvatures H^* and H° . **c:** Gaussian curvatures K , and dimensionless Gaussian curvatures K^* and K° . **d:** Configurations A, B, C, D, E in initial state (wet). **e:** Configurations after self-shaping (dry). **f:** Experimental configurations, 1:1 physical model rebuilds of the FE models using beech wood.

In the graph of the mean curvature H (the arithmetic average of κ_1 and κ_2) the effect of strip width w on shaping becomes apparent and it is revealed that wider strips increasingly reduce gridshell curvature for lower values of h . The plot of mean dimensionless curvature $H^* = Hh \approx \varepsilon_m$ reveals a dependence of average bending strain ε_m on configuration. It should be noted here that the value $\kappa_0 h$ is constant for all h and w because of the compatibility $\kappa_0 = h^{-1}\varepsilon_0$ where ε_0 is the bending strain of an infinitely narrow strip. Therefore, the investigated gridshell configurations tend towards higher bending strains in proportion to h as h itself is increased, and a dependence on w is observed for $h < 10$ mm. Alternatively, and instead of showing the amount of gridshell shaping in terms of bending strain alone, the dimensionless plot $H^\diamond = H\kappa_0^{-1} \approx \varepsilon_m \varepsilon_0^{-1}$ represents the shaping behavior in terms of curvature realized in proportion to natural curvature of single strips, or in terms of average bending strain achieved in proportion to natural bending strain. It can be seen that an increasing thickness of the strips contributes towards the gridshell shaping to a higher extent where H reaches up to approximately 105 % of the value of κ_0 . However, at around $h = 10$ mm, this behavior is critically inverted and at around $h = 5$ mm, H reaches approximately 40 % of κ_0 only. We explain this behavior by the fact that for thicker and wider strips, the bending moments, instead of resulting in in-plane deformations as for the narrow and thin strips, result in further out-of-plane deformations of the strips in a manner as to increase their curvature so that $\kappa_1, \kappa_2 > \kappa_0$. Therefore, configurations where $H^\diamond = H\kappa_0^{-1} > 1$ are not impossible. However, we note that by varying w , the proportional spacing of the strips in the grid with respect to w is automatically varied too, and that this influence regarding configurations where $H^\diamond = H\kappa_0^{-1} > 1$ is not determined.

The plot of achieved double-curvature, i.e. the Gaussian curvature $K = \kappa_1 \kappa_2$ shows a very similar trend than that of the mean curvature H . However, it is apparent here that the configurations B and C effectively do not achieve double-curvature. In general, thicker and wider strips result in lower values of K . Similar to H^* , the graph of $K^* = Kh^2$ surprisingly shows that the double-curvature scaled over squared thickness is higher for thicker strips. Application-wise, e.g. for load-bearing self-shaped and double-curved gridshells structures, this suggests that an optimum of slenderness of strips compared to double-curvature-benefits, i.e. bending moment free members, may exist. Finally, in the same manner, the dimensionless double-curvature $K^\diamond = K\kappa_0^{-2}$ shows a matching trend with H^\diamond , leading to the conclusion that the qualitative behavior of mean gridshell curvatures

corresponds to that of the Gaussian curvatures in the case where the gridshells adopt a double-curvature (e.g. configurations A, D, and E).

The highly non-trivial but complete parametric space of a self-shaping gridshell would additionally include the number and spacing of the strips, variation in layer thickness ratio of the strips, variation in initial and target moisture contents, and variation in wood species and local anisotropic material orientations in the layers. Nonetheless, the presented analysis and implications are deemed as independent of scale and may be readily applied to other self-shaping composite systems beyond wood, e.g. in the field of soft actuated matter.

7.5 APPLICATION

For timber gridshells in architecture, the double curvature is a decisive advantage that ideally enables bending-moment-free members under self-weight. In this context, the presented principle of self-shaping would be able to resolve some classical challenges inherent to timber gridshells. In fact, standard construction methods like pre-forming of the curved strips require intensive processes of forming and bending. Post-forming of a gridshell, a further method, can be achieved by a combination of lifting and elastically bending (active bending) the structure into a fixed position. However, heavy edge constraints are required to confine the elastic bending forces in the strips [189–191] (see in Fig. 7.4). A type of self-forming process using gravity and mechanical locking of the individual layers has been shown at conceptual level but still requires additional machining and forcing of the structure into the curved shape [192]. In addition, conventional gridshell design is limited by the achievable cold-bending radius with respect to the lamella thickness and the wood quality [193, 194]. Shaping a structure through the arrangement and material programming of its individual elements, like in the self-shaping process (Fig. 7.4), alludes to new types of simple, yet sophisticated deployable structures at medium to larger scale (0.1 m to 10 m) and addresses the mentioned problems restricting conventional gridshell designs. Most importantly, self-shaping can deplete the need of tedious elastic shaping by exterior forces.

In order to realize such applications, some challenges remain to be addressed. In self-shaping gridshells, the timber strip members would be inherently composed of a large proportion of the strips with wood of grain direction being transverse to the strip direction. In the case of the investigated gridshell cross-sections above, for example, a 4/5 proportion is

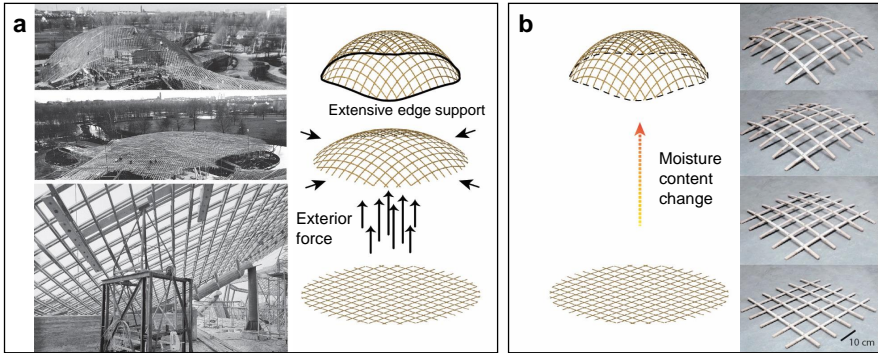


FIGURE 7.4: **Gridshell shaping procedures.** **a:** Conventional procedure by shaping the gridshell via exterior forces for active elastic bending; Extensive edge support is needed in the assembled configuration (Photo credit: *Institute for lightweight structures and conceptual design, University of Stuttgart*). **b:** Novel proposed procedure by hygromorphic self-shaping of the single strips; No exterior forces and lighter edge support.

composed of wood with perpendicular grain direction. Therefore, large-scale load-bearing gridshells might be prone to increased buckling risks because of the normal forces in the members [195]. It could be of relevance, for example, how the a priori reduced critical buckling load depends on the grid spacing parameters affecting the buckling length. Therefore, the possible phase-space for large-scale applications of self-shaping timber gridshells might be reduced because of design restrictions with respect to stability. Nevertheless, such aspects highly depend on the material or wood species used [193, 194], and European beech typically shows higher strength and stiffness than the common traditional softwoods used for timber gridshells [13].

Timber gridshells, thanks to their slenderness, can be formed to adopt complex-curved shapes beyond uniform double curvature [196, 197]. Such complex shapes are also possible with self-shaping. However, the programming of such complex self-shaping gridshells by numerical analysis will need to be integrated in application-based form-finding procedures that are traditionally used for standard design of gridshell geometry under service loading conditions [198–203]. Especially, the minimizing of overall strain energy, here induced by the self-shaping, and with it the additional contributions of in-plane bending moments identified above, might be rel-

evant for form-finding design [204]. Furthermore, and in contrast to the investigated configurations, an even more effective achieving of a uniform $\Delta K > 0$ by self-shaping with respect to strain energy minimization might be achieved by an in-plane slip degree of freedom at the connections of the strips. Finally, while the computational analysis in this study focused on simple symmetric gridshell configurations, further tuning and variation of the strip geometry is made possible by parametric computational tools such as the model used above. Such tools of digital design, coupled to digital robotic fabrication, could be used to shape more complex shell forms at large scale for architectural applications.

7.6 CONCLUSIONS

Our results show that self-shaping wood gridshells enable positive changes in Gaussian curvature (K), which is impossible for solid plate geometries of single bilayer-composites of anisotropic materials. The shaping behavior appears to be dictated by complex interactions between the strip's thickness and width. On one hand, for thin and narrow strips, the large change in K is enabled by the in-plane bending deformations of the strips of the rigid-jointed grid. On the other hand, for thicker and wider strips with lower changes in K , in-plane bending moments enforce the system's shaping towards values close to or slightly surpassing the natural curvature of single strips. The presented self-shaping would overcome many of the constraints of post-formed timber gridshells in the sense that complex lifting and forming is replaced with distributed autonomous actuation. Less structure is needed to constrain the shell after forming, tighter radii of curvature, and more complex lamella interactions would be made possible.

7.7 SUPPLEMENTARY MATERIALS

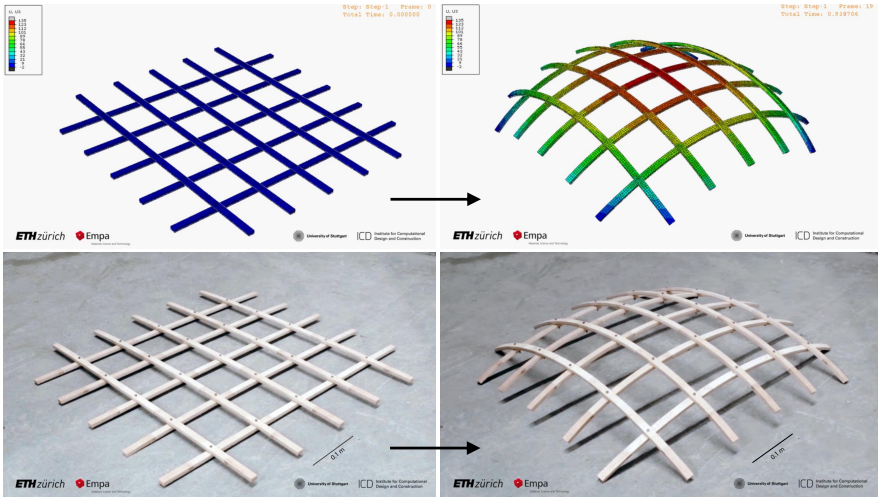


FIGURE 7.5: *Movie S1: Caption: : Exemplary gridshell self-shaping process in computational and physical model.* FE simulation of self-shaping process of a 5x5 gridshell made out of beech wood and physical reconstruction. U_3 : Out of plane displacements in mm. Parameters: Strip geometry: 600 mm length, 12 mm width, 2 mm passive layer thickness (radial orientation), 5 mm active layer thickness (longitudinal orientation). Boundary conditions: Change in moisture content from 14% to 21%, physical sample relocation from 65% to 95% relative humidity climate at 20°C.

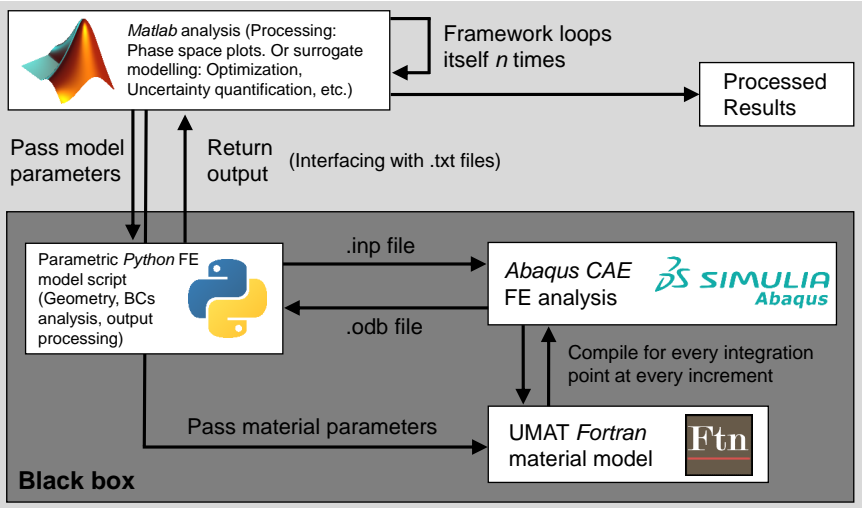


FIGURE 7.6: **Framework for parametric FE analysis.** Analysis parameters such as FE model geometry or boundary conditions (BCs) can be automatically sampled via *Matlab* scripts and passed for FE analysis to parametric *Python* scripts. FE model material parameters can be directly passed to user material subroutines (UMAT) written in *Fortran* 77 (not used in this study). The framework is based on a black box approach and, therefore, facilitates parametric analyses such as phase diagrams, optimizations, or uncertainty quantification, which can be conducted in frameworks decoupled from the FE analyses. (*The authors state not be associated or sponsored by any of the organizations whose logo is appearing in this figure*).

TABLE 7.1: **Coefficients for calculation of moisture-dependent elastic engineering constants.** The elastic engineering constants P_i calculate as $P_i = b_0 + b_1\omega$ for European beech wood [11, 115] and for ω in %. Young’s and shear moduli E_i and G_i in units of MPa, Poisson ratios ν_i dimensionless.

	E_R	E_T	E_L	G_{RT}	G_{RL}	G_{TL}	ν_{TR}	ν_{LR}	ν_{LT}
b_0	2566	885	17137	668	1482	1100	0.293	0.383	0.337
b_1	-59.7	-23.4	-282.4	-15.2	-15.3	-17.8	-0.001	-0.009	-0.009

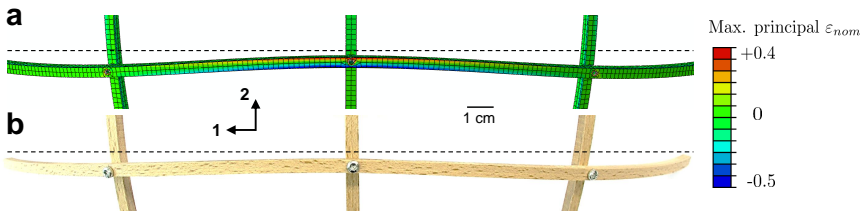


FIGURE 7.7: **In-plane bending of a border strip from configuration A visualized in the 1-2 plane.** **a:** Maximal principal nominal strains of deformed FE model configuration. It can be recognized that at the crossing between middle and border strips, the in-plane bending strain takes over the self-shaping (out of plane) strains as the maximal principal strain components of the strain tensor. **b:** Image of Experimental configuration A.

SYNTHESIS

8.1 GENERAL DISCUSSION

The work in this thesis can be attributed to two sequences in biomimetic research for architecture and construction, following [30], illustrated in Fig. 8.1. It was motivated equally by the previously identified self-shaping capacity of biological systems [37] with abstraction to wood [7] (bottom up approach), and by the need of a more favorable technical solution for producing curved timber elements (top down approach). The investigation of the applied biological principle of self-shaping to wood [7], in combination to the wood science and engineering field, especially the sub-field of wood computational mechanics [11], lead to the new fundamental insights presented in chapters 4 and 5. These new insights then enabled the technical work and implementation into the construction and architecture field as presented in chapter 6, and finally, enabled the bionic product and demonstrator in the form of the *Urbach tower*. Chapter 7 then treated on limitations and additional possibilities of the applied biomimetic principle of self-shaping wood at large scale. Hereafter, both the fundamental and the technical work will be summarized and discussed.

8.1.1 *Summary and bridging of main investigations*

In chapter 4 (paper I), based on the work in [7], a simple model for prediction of curvature of two laminated materials with different expansion coefficients with respect to each-other was adapted to the material wood. Hereby, especially the moisture-dependency of the elastic parameters of wood and the correct anisotropy reduction from a 3D to a 2D analytical model were accounted for. The geometry and material parameters entering the model have been characterized in terms of propagation of variability. Furthermore, parametric studies have been conducted showing the influence of input parameters on curvature, elastic energy, and axial stresses. Especially, it was shown that certain combinations of parameters, e.g. an optimal thickness ratio of the thicknesses of both layers, minimize occurring axial stresses and elastic energy at the same time curvature is maximized.

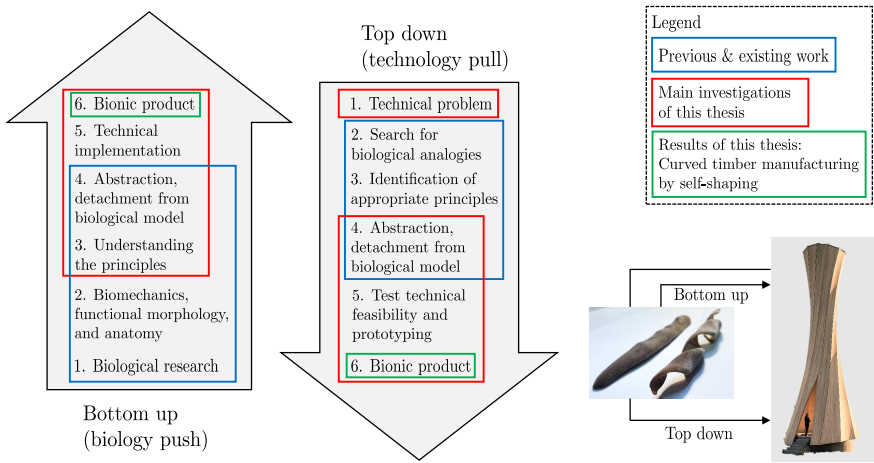


FIGURE 8.1: **Thesis work in the context of process sequences in biomimetic research.** Bottom up and top down process sequences as proposed in [30].

These considerations are of particular importance in application-based design, e.g. for the reduction of delamination risk by keeping stresses low.

While these findings are valuable and easily applicable for practical design, their validity is restricted by the limitations inherent to the assumptions made to derive the model. Specifically, the 2D model only considered linear elastic material behavior and steady-state moisture content (MC) changes. However, it was stated in chapter 1 and shown in chapter 3, that such conditions are not applicable to wood with respect to state-of-the-art simulation of material behavior. In order to address these issues and to gain in-depth understanding of the 3D material behavior under self-shaping, especially in terms of desired knowledge about the time-dependent behavior in context of moisture diffusion for up-scaling of layer thicknesses, the investigations in chapter 5 were conducted.

In chapter 5 (paper II), a complex material model for wood [11] was used in combination with 3D numerical mechanical analysis and transient moisture diffusion for computation of curvatures and time-dependent stresses and strains of self-shaping wood bilayers. Specifically, and in contrast to chapter 4, the numerically and experimentally investigated configurations of beech and spruce wood possessed layer thicknesses up to 30 mm. Aspects already covered in chapter 4, e.g. that axial stress levels remain in-

dependent of bilayer thickness given that the layer thickness ratio is the same, could be verified. It was demonstrated that curvature remains constant if layer stress ratios remain balanced under the influence of different deformation mechanisms, which is the case for wood bilayers. In fact, rate- and moisture-dependent mechanisms happening in both active and passive layers, such as visco-elasticity or mechano-sorption, appeared to compensate each-other and result in a constant layer stress ratio over time after moisture equilibration. In addition, it was shown that such axial stresses remained low, in contrast to values found in chapter 4, because creep mechanisms prevent exceeding strengths and yield stresses during the time of shaping. A critical moment during shaping could be identified as the time when axial stresses in the active layer are of tensile nature due to the initial drying phase dictated by surface boundary conditions. This critical time is reached when moisture gradients are steepest, shortly (1-15 h) after climate relocation of the bilayers. Finally, another aspect from chapter 4 that could be verified using the complex numerical model was that for beech wood, the sensitivity of the swelling coefficient was the highest among the tested parameters with respect to influence on curvature. On the other hand, none of the tested parameters majorly impacted variability of curvature in the case of spruce wood.

In addition, thanks to the investigations on thick layers, chapter 5 presented for the first time the concept of the novel self-shaping manufacturing approach for curved timber elements for building-scale components using wood bilayers. Self-shaping was presented as a smart alternative to standard cold-bending of thin lamellae for industrial production of form-stable curved mass timber. The unique combination of a computational mechanical analysis, a sensitivity analysis, and an experimental investigation allowed for capturing the behavior of thick self-shaping wood bilayers, and further, allowed for the development of a manufacturing process for large-scale curved cross-laminated timber (CLT). In a next step, the findings of both chapters 4 and 5 were directly applied in an industrial frame in the context of an *Innosuisse* project. The major findings relevant to the industrial production have been, from chapter 4, the optimal layer thickness ratio in order to minimize axial stresses, and from chapter 5, the crucial adaption of the industrial kiln-drying process towards a milder drying in order to avoid drying cracks in the active layers. Therewith, the manufacturing process characterized in chapter 6 could be successfully developed.

Chapter 6 described the first worldwide built application of self-shaping wood, the *Urbach Tower*. In this collaborative project between architects,

structural engineers, materials scientists, and a timber saw-mill and construction company, a self-shaping manufacturing process was developed in the integral framework of raw material processing in the sawmill up to the finished building components and tower assembly on-site. The focus was on the development and characterization of the manufacturing process and its resulting product, form-stable curved CLT plate-elements. It was shown that boards used for manufacturing the active layers need to be of best possible quality and of standing annual ring orientation. This ensures that the variability in curvature resulting from structural inhomogeneity is reduced. In addition, the initial MCs of active layers need to be of low variability as a broad distribution due to less strict sorting inside a bilayer plate resulted in higher deviation with respect to target curvature. In fact, the variability in curvature observed for the 31 produced plates was attributed to the variability in initial MCs. The numerical prediction by FE models appeared to represent an upper bound of achieved curvature. However, due to the low bending stiffness of the plates in the curved direction, plates could be readily stack-laminated into the final form-stable curved CLT shape using a light form-work with predefined radius of curvature. It was observed that there was no spring-back, which is a decisive advantage in terms of predictability of shape compared to other production methods as the parts can directly be processed by CNC machines without further scanning and characterization of geometry. Finally, it was shown that self-shaped curved CLT is suitable for structural applications. The major concern laid in the fact that the gap thickness of the adhesive joint of the stack-lamination would be too large for standard adhesives such as 1cPUR to be used. However, both a three-point bending and a shear-block tested proved that the gap thickness did not influence load-bearing behavior and that a specialized gap filling adhesive (2cPUR) is not of necessity.

The developed manufacturing process successfully allowed for building the curved lamellae used for the *Urbach Tower* project. Therefore, suitability for industrial application, as well as suitability for use in structural timber structures was proven. However, the process is restricted to plates that curve along a single direction. The tower's apparent twist and curvature along multiple directions is due to the diagonal cutting out of single-curved half-cylinder sheets. In contrast, the self-shaping process applied to wood would be of tremendous competitiveness if, in addition, double-curvature could be achieved. In fact, architecture and timber engineering often favor form- or surface-active structures [155] such as double-curved shells, which are efficient in terms of load-bearing and material utiliza-

tion because of the thin cross-sections enabling to span large areas. As was shown in chapter 2, achieving double-curvature, i.e. a large change in Gaussian curvature, is a very restricted concept for self-shaping composites made out of anisotropic materials such as wood bilayers. Especially, if layer-thicknesses for large-scale application are required. Therefore, in chapter 7, a conceptual solution was developed and investigated at a medium scale by application of computational mechanical analysis.

Chapter 7 (paper III) showed how bi-layered anisotropic materials can achieve a positive change in Gaussian curvature by self-shaping towards double-curved shell-like structures. According to chapter 2, the composites need to be in narrow strip configurations in order to allow the strips to shape towards curvatures equivalent to their natural curvature. Therefore, the strips were organized in orthogonal grids where the slenderness allowed for large in-plane stretches along both strip-directions. The results were self-shaped double-curved gridshells originating from initially flat wood bilayer strips. The conducted numerical study showed that the shaping behavior is dependent on the strip's width and thickness, and that some configurations can achieve double-curvature while others do not. Furthermore, depending on width and thickness, the natural curvature can even be surpassed in the gridshell configuration due to the system behavior. It was stated that the self-shaping behavior still would need to be integrated into the standard form-finding process used in order to design gridshells, and that this might be a non-trivial task. In addition, a full parameter space would need to be covered, including custom changes in MC and layer thickness-ratio, which also significantly might impact the grid system's shaping behavior.

While the study in chapter 7 focused on simple symmetric grid shell configurations at a conceptual level, large-scale applications might be made possible with digital design and fabrication in the same manner as such an application was made possible in chapter 6 based on the studies in chapter 4 and 5. A benefit of large-scale self-shaping gridshells would be that a challenge typical to the common timber gridshells in architecture would be solved in addition. Namely, the tedious erection procedure by extensive elastic bending using exterior forces. Using the self-shaping strips, the gridshell could erect itself and in the built state, would need less edge-constraining as the elastic forces would be contained inside the structure in the form of residual stresses of self-shaping.

8.1.2 *Simple analytical versus complex numerical model - Which is appropriate?*

In this thesis, two models were presented in order to model self-shaping wood materials. While one model is of rather simple analytical nature, the other is complex and implemented into a finite element framework. As can be seen in chapters 4 and 5, the two models do not significantly differ from each-other in terms of precision of curvature-prediction alone.

The simple analytical model derived in chapter 4 proved to accurately model curvatures of thin bending beech bilayer in a precision range of 10%. Thanks to its analytical nature, a very large number of input parameters can rapidly be tested and analyzed by parametric analysis, both in terms of design with respect to deformation and stresses, and of sensitivity analysis of input parameters. In fact, the model showed to be suitable even for Monte-Carlo based approaches of uncertainty quantification, where usually, a number $> 10^6 - 10^9$ model evaluations are necessary. Furthermore, the simple model presents the straightforward advantage of being easy to understand and to implement by a broad range of practising engineers for direct applications in design and product development. As an alternative, even simpler models can also be used, whose precision of prediction is presumably similar [7, 51]. However, such models do not consider the complex effects that happen with respect to the mechanical behavior of wood and are limited to predict the natural curvature of bending-only wood bilayers.

On the other hand, the numerical model used in chapter 5, where the complexity mainly originates from the used material model for wood rather than the modelling technique itself, proved useful for both the prediction of deformation and in order to capture the exact rate dependent deformation mechanisms. In addition, an integral 3D continuum is represented by modelling a 1:1 physical geometry and by considering local and time-dependent processes such as moisture diffusion. Therefore, and in contrast to the simple analytical model, any custom geometry of self-shaping wood composites can be modelled. However, in terms of parametric analysis, advanced mathematical tools such as the polynomial chaos expansion need to be applied in order to create a surrogate model for the sake of sensitivity analysis as model-run-times do not allow brute Monte-Carlo sampling.

In summary, the simple analytical model can be recommended when there is a need for quick and efficient prediction of natural curvature of wood bilayers produced in the cross-ply configuration. However, a deeper understanding of material behavior is missing. Therefore, the complex numerical model can be used. But other than in a scientific framework, its

complexity is a major drawback with respect to user-friendliness in applied engineering.

8.1.3 *Tackling model-overestimation in spruce wood*

As stated in chapter 5 and 6, in the case of spruce wood bilayers, considerable overestimation of curvature by the numerical model could be observed, whereas beech bilayer curvature could be modelled more accurately. While beech is a diffuse-porous hardwood species with a rather homogeneous density profile across annual rings, spruce is a species with special softwood behavior. One example for this is the pronounced rolling-shear, originating from the intricate mechanical behavior of the easy to buckle and low-density earlywood layers in-between strong latewood layers [205]. As mentioned in chapters 5 and 6, problems in predictability could originate either from complex material behavior, such as non-linear elastic mechanical behavior that is not captured in the model parameters used, inaccuracy especially in visco-elastic and mechano-sorptive material parameters, or in the local mechanical behavior, e.g. curvature of annual rings or a scale-dependency of mechanical behavior of early- and latewood layers. Some of these problems were addressed in additional work conducted during this thesis, and discussed in chapter 6¹. A major observation was that the local deformations measured by digital image correlation in active layers near the interface of spruce bilayers did not match data obtained by numerical simulations, which would indicate a poor shear transfer in reality, and hint at issues with existing understanding of wood material behavior. However, due to the complexity, even these considerations have up to date not lead towards a better understanding on how to increase prediction-precision of spruce wood bilayer curvature.

The sensitivity analyses conducted in chapters 4 and 5 have revealed a critical dependency of variability in curvature on variability in axial stiffnesses for spruce, but on variability in swelling coefficients for beech. However, also for spruce, swelling aspects could be considered as the cause of model over-estimation. As was shown in chapter 3, the interplay between wood mechanics and swelling, both coupled by the micro-structure, might be of relevance. For example, swelling appears to induce shear strain in samples of Norway spruce [206, 207]. This behavior was not captured in the model used, as the swelling, i.e. volume changes, was thermody-

¹ Methods, results, and discussions of the additional works are shown in separate reports [160, 161].

namically decoupled from the mechanical energy formulation of the system [11]². Furthermore, when experimentally measuring swelling coefficients needed for the model, shearing or coupling entries of the tensor containing the swelling coefficients are usually neglected, as the parameters are measured purely by deformations in principal directions of prismatic samples. In addition, as known for some polymers, the influence of the stress state internally acting on the wood might play a role on moisture diffusion, equilibrium MC, and hygro-expansion coefficients [208–210]. Furthermore, moisture transport itself was modelled by fitting a 3D anisotropic Fickian diffusion model to experimental curves of MC development over time. However, more precise transport models exist that consider non-Fickian diffusion models for wood [211].

Not yet considered either were strategies such as quantification of reversibility of curvature of large-scale wood bilayers. Such investigations would lead to detection of possible damages by differences in curvature. However, complex effects such as time-dependency of mechanics and the sorption hysteresis do not make such experimental work trivial. Other methods could be used such as automated detection of damage and cracks with acoustic emission, digital image correlation, or synchrotron-based tomographic microscopy in order to capture local effects during the shaping process [212]. Damage effects could subsequently be included in the continuum mechanical material model e.g. by adding cohesive zones for including fracture behavior or implementing damage laws to the relevant material parameters. However, such approaches would follow a philosophy of inverse-fitting, which is a procedure commonly accepted in engineering for practical reasons, but lacks the fundamental aspect of predictive constitutive material modelling. On a more fundamental level, multi-scale models could be used in order to shed light on the underlying structure-property relationships instead of on the phenomenological macroscopic mechanical behavior of wood [124, 127–131].

8.1.4 *Enhancing model precision by reduction of variability*

Regardless of the model used in order to predict curvature and its degree of precision, an important aspect for predictability is to cope with uncertainty induced by the variability in model input parameters. Specifically, this variability is unavoidable for the material parameters of wood. It is therefore of high interest to characterize the probability density functions

² Notice: The same applies to beech wood.

of natural distributions of these properties. In the investigations conducted in chapters 4 and 5, such functions were, for the most parameters, assumed using subjective judgement. Using both analytical and numerical models, sensitivity analyses were conducted in order to quantify what model input parameter had the strongest impact on variability in model output (the curvature) when its own value was changed in the frame of its natural distribution. It was shown, when using beech wood, that the highest sensitivity can be attributed to the axial swelling coefficient in the bilayer's active layer. Therefore, if its epistemic uncertainty can be reduced by precise measurement, the model's uncertainty can be significantly reduced too. However, it is important to note that the aleatory uncertainty can never be reduced by characterization measurements alone. Therefore, the model precision will always be limited to the range of aleatory natural distribution of the material parameters.

At large-scale in industrial production, next to the obvious quality sorting, e.g. minimizing knots, some strategies allow for further minimization of the aleatory uncertainty of swelling coefficient in the active layer. For example, it is known that the swelling coefficient for wood is highly dependent on local material direction but also on structural aspects such as density or the microfibril angle. From these considerations, two strategies arise in terms of better prediction at the large scale. One option is to produce boards with the least amount of variability in annual ring inclination, e.g. perfectly rift-sawn boards with no annual ring curvature. The other option is to cut the rift boards along positions in the stem that show the least amount of variability in microfibril angle or density. For example, one could systematically exclude boards containing mixed xylem types, e.g. reaction wood, as here, the microfibril angle changes swelling behavior and adds additional and undesired residual reaction stresses to the boards [213, 214]. However, industrial cost-effectiveness of such considerations still would need to be assessed in terms of desired or required model precision that such measures would entail. And as was stated in chapter 6, the variability in MCs still represents the major challenge.

8.1.5 *Scale-dependent versus scale-independent effects in self-shaping wood*

Since the up-scaling of wood bilayers from the laboratory to the industrial scale was a major objective, it is noteworthy, from the conducted analyses in this thesis, to distinguish and to summarize scale-independent and scale-dependent effects affecting the shaping behavior. As shown in the analysis

of chapter 4 and confirmed in chapter 5, the major scale-independent aspect is that the axial residual stresses of self-shaping are not dependent on the total thickness of the layers but only on layer-thickness ratio. This fact seems at first counter-intuitive but is rationalized by the fact that thicker bilayers bend less due to the simple compatibility condition $\kappa = h^{-1}\varepsilon$ (see ³) and that therefore, a balance between κ and h results in a constant value of ε , and therewith, of axial bending stress. As a consequence, rate-dependent wood deformation mechanisms do not influence the shaping behavior in dependence of scale either. On the other hand, a relevant scale-dependency was found in total elastic energy of shaping, and in stresses caused by moisture gradients. The total (2D) elastic energy was found to increase linearly with h and the time of moisture equilibration is approximately proportional to h^2 (see ⁴), resulting in higher moisture gradients affecting the local mechanical behavior. Therefore, the combined effects may highly impact fracture energy and thus play a relevant role in addressing cracking and delamination in function of h . By these thoughts, it can also be concluded that there is an upper limit of feasible thicknesses of wood bilayers, above which, the bilayers crack and delaminate upon the MC change instead of self-shaping. However, it needs to be noted that the maximum thickness will also depend on boundary conditions, e.g. the rate of imposed climatic change.

8.1.6 *Optimizing the industrial production of self-shaped CLT*

New and complex manufacturing processes such as the one presented in chapter 6 might be difficult to integrate into standard production schedule of traditional timber manufacturing and building companies. Concerns arise mainly in the willingness to shift towards new processes that defy the known standard procedures in terms of wood processing. For example, in the self-shaping manufacturing of curved CLT, great care needs to be taken with respect to the quality of the wood used. The boards not only need to be sorted by strength-grading, as in the usual case, but also regarding standing annual rings or MC. Afterwards, the boards need to be carefully edge-glued in order to form the active layer plate elements, which is also a process usually omitted in standard CLT production. Also, a specific pattern of parallel annual rings between the boards needs to be

³ κ : Curvature of bending; h : total layer thickness as sum of both layers of the wood bilayer; ε : Equivalent bending strain.

⁴ Assuming Fickian transport laws.

respected for best predictability. Furthermore, standard procedures such as the kiln-drying schedule need to be adapted.

Further challenges arise from the lack of possibilities to control the process with respect to monitoring, e.g. of the wood MCs and deformations over the production time. It was shown in chapter 6 that a major problem was the initial sorting of boards in terms of MC. Following *DIN EN 338* [215], timber is usually sorted and graded by strength, stiffness, and density, whereas grading by MC is much less prevalent [216] because of uncontrolled climatic conditions before and after sorting. While it is easier using machine and visual grading to sort boards by quality and standing annual ring orientation, it is much more challenging to sort timber accurately by MC because of the uncontrolled conditions the boards endure until the sorting. In fact, raw logs are often provided by the forestry industry in a wet, over-hygrosopic state, where the exact MC can not be controlled because of considerable variability across logs, across the position in the log, and because of gradients over the thickness. Therefore, even by air-storage at controlled conditions, boards will not adapt a homogeneous MC in a time frame useful for industry. In this sense, the challenge lies in sorting the boards by initial MCs just below the fiber saturation point but, in order to achieve enough curvature, above approximately 22% MC. This sorting needs to be conducted either before or after the sorting by quality and annual ring orientation. And if the variability in MC can not be kept low enough, as was shown in chapter 6, kiln-drying chambers preferably need to be adapted in order to be able to reach a given initial MC in the range of 22%-30% with low variability.

In summary, the industrial production process would be optimized both in terms of quality and predictability of curvature by measures such as versatility and adaptability in the production. Additionally, measures such as optimal sorting, monitoring, and drying of initial boards would notably contribute towards an optimized industrial production process.

8.1.7 *Addressing cracking and delamination of CLT elements made from self-shaping wood*

Next to considerations mentioned above in terms of scale- or thickness-dependency of the cracking risk, the cracking at large-scale in CLT elements represents a further point of interest. As shown in chapters 4 and 5, the residual stresses of self-shaping of wood bilayers ultimately result in compressive stresses at the active layer edge when the bilayer is relocated

from wet to dry climate. Therefore, after the stack- or locking-lamination shown in chapter 6 to obtain curved CLT elements, a beneficial compressive pre-stress is acting on each of the lamellae on roughly half of their cross-section in the thickness direction. Compared to standard cold-bent lamellae for producing CLT, the stress state is similar. But in contrast, due to the slower shaping, no initial damage presumably⁵ occurs in the lamellae with grain perpendicular to the curvature direction. Therefore, curved CLT elements, especially produced from self-shaped parts, are conceptually less prone to cracking than straight CLT elements. In addition, the thicker active layer boards are edge-glued whereas the thinner passive layer boards are not, and this concept respects recommendations given for optimal avoidance of cracks in CLT. Specifically, studies showed that cracks can be avoided by minimizing layer thickness or by edge gluing of the boards [217]. Even more optimal conditions can be met when the annual ring orientation of the boards is standing, as this complies with recommendations in order to minimize tensile stresses in layers due to moisture-variations in service life-time [218, 219]. In addition, a standing annual ring orientation in the active layers of self-shaping wood⁶ was demonstrated as preferable in terms of predictability of shaping behavior.

On the other hand, when addressing delamination, the adhesive and adhesion properties are usually of higher importance than the wood properties and the CLT assembly [220, 221]. Here, if structural applications are desired, delamination tests should to be conducted in order to assess whether the adhesive glue-line is able to sustain harsh climatic changes [168]. However, for self-shaping wood and CLT made thereof, these requirements are usually of low concerns since cracking in the wood is likely to happen first under either climate or mechanical loading. This is the case especially when Norway spruce wood is used. Still, conducting such delamination would be required if hardwoods such as European beech are used, where in proportion to wood mechanical strength, the strength of the adhesive bond is lower and the swelling is higher [222, 223].

8.1.8 *Integrating self-shaping manufacturing for double-curved structures*

A possibility for achieving double-curved structures was shown in chapter 7. However, the presented gridshell shaping behavior was studied at a

⁵ The visco-elastic creep keeps the residual stresses below the strengths during the shaping, whereas in conventional elastic bending the stresses act instantaneously. However, as mentioned previously, damage formation during self-shaping was not assessed in this work.

⁶ For rift-cut boards: R direction perpendicular and T direction in stacking direction.

medium scale more applicable to furniture design. In terms of modelling and prediction of shaping behavior, the same procedure could also be applied at the large scale. However, additional aspects such as the structure's dead load and details of the connections between the strips would need to be considered. And as already mentioned in chapter 7, a crucial step is the integration of the modelling of self-shaping behavior in the frame of form-finding processes in order to design the structure in terms of required geometry under live loads. The manufacturing process itself would only need to be adapted in terms of enabling to join the strip elements along their length direction. But the strips could easily be cut sequentially from a sheet or plate of bi-layered wood as shown in chapter 6. Furthermore, a fundamental consideration with respect to application at large scale is whether it is desired to build the gridshell in flat state and let it shape itself into the desired double-curved structure, with subsequent form-locking by stacking lamination or mechanical fastening with a second, identical structure. Another approach would be simply to let the single strips deform prior to the assembly in a grid configuration, to stack-laminate them, and to assemble the double-curved structure on-site. However, with this the benefits of space-saving in terms of storage and transportation would be lost and the on-site assembly might be challenging compared to an assembly in flat state. In conventional gridshells, the pre-fabrication of curved parts is increasingly desired and preferred over elastic bending [197]. On one hand, digital design and fabrication nowadays facilitate the manufacturing of curved parts, and on the other, no residual stresses of elastic bending of the gridshell, which negatively impact load-bearing capacity [194], would be present if, e.g. subtractive milling is used. However, and especially for such cases, the self-shaping manufacturing method presented in chapter 6 would be beneficial, as it is presumed that the manufacturing method is overall cheaper and that the residual stress state of self-shaping is beneficial under externally-induced bending stresses. A drawback in the context of pre-fabricated gridshell elements would be that self-shaped curved CLT would need to compete to conventionally produced glued-laminated timber (GLT). Because of lamella lay-up, GLT beams are typically stronger and stiffer than CLT beams, and therefore, more suited for long-spanning gridshell elements where bending behavior is of relevance. However, bending in gridshells may be entirely avoided by suitable design with respect to double-curvature.

8.2 SUMMARY

In the context of the objectives introduced in chapter 1, the investigations in this thesis can be summarized in terms of fundamental analysis of material behavior as:

- The shaping behavior of biomimetic self-shaping wood composites was analyzed by parametric studies using a wood-adapted analytical formula for curvature, elastic energy, and stress prediction. In addition, by using a complex computational mechanical model, 3D and large-scale effects such as moisture diffusion and the relevant time-dependent mechanical behavior could be assessed.
- Next to parametric analyses and effects of complex mechanical behavior at large scale, strategies for optimal predictability of shape were investigated and discussed for two wood species, European beech and Norway spruce. Sensitivity analyses were conducted where impact of variability in different model input parameters was calculated in terms of variability of resulting curvature.
- Limitations and possibilities for achieving double-curved structures were investigated. Parametric analyses were conducted in order to investigate the system-shaping behavior of grids consisting of connected narrow wood bilayer strips. It was shown that, on a system level, such structures are able to shape towards domes with a positive change in Gaussian curvature.

In terms of applied investigations at industrial scale:

- Together with research and industry partners, an adaptive manufacturing process for production of form-stable curved CLT timber elements by using the self-shaping method was successfully developed. The production process was customized in order to achieve the target radius of curvature required for a demonstrator and proof-of-concept project, the Urbach tower.
- The industrial self-shaping manufacturing method was enabled by setting a required quality of wood and of the lamination steps. Furthermore, the process was characterized by monitoring wood MCs and deformations throughout the process. In addition, the produced curved CLT elements were tested by static loading tests in view of structural applications.

8.3 SIGNIFICANCE AND APPLICATION POTENTIAL

The application potential of large-scale self-shaping wood was demonstrated by the developed manufacturing process for the *Urbach tower* project. A major benefit is that there is no spring-back effect after the lamination of the curved components. This represents a decisive advantage compared to conventional production processes as still today, extent of spring-back cannot be accurately predicted. In general, while the self-shaping manufacturing process can still be competed by standard cold-bending for configurations such as the curved panels from the *Urbach tower* project, it represents a niche-manufacturing technique for highly curved parts. The usual restrictions of a certain maximal lamella thickness for a given radius of curvature do not apply in the same manner. Especially at the building scale, it was shown in chapter 6 that a 10 mm + 30 mm thick bi-layered wood configuration achieves a radius of curvature of approx. 2.60 m by self-shaping. This relation can be illustrated with Fig. 8.2, which showcases that an effective economical benefit is possible by considering both active and passive layer lamellae together. For the same radius of curvature, the passive layer lamellae need to be slightly thinner than conventional cold bent lamellae but active layer lamellae can be thicker by a factor of more than two. Therefore, the beneficial application potential lies in timber structures that are highly curved. Examples could include tall tower structures with cylindrical cross-sections, e.g. wind turbine towers.

In this thesis, next to using Norway spruce for self-shaping, also the species European beech was characterized in this respect. European beech is a wood species nowadays gaining relevance in the modern European timber sector because of its still underutilized potential and thanks to its availability and the recent research in applied technology and engineering [225]. In addition, the relation shown in Fig. 8.2 is even more beneficial for beech wood, which achieves higher curvatures by self-shaping than spruce for same lamella thicknesses. In terms of general significance, the developed manufacturing method for curved timber components will entail further promotion to use timber of both species in free-form architecture, and therefore, contribute to a more sustainable building sector for the future.

In the context of materials science of self-shaping composites, especially the aspect of locking-lamination of multiple self-shaped parts after a one-time actuation and the system behavior of a grid-assembly of thin strips that changes its Gaussian curvature could be of significance and applica-

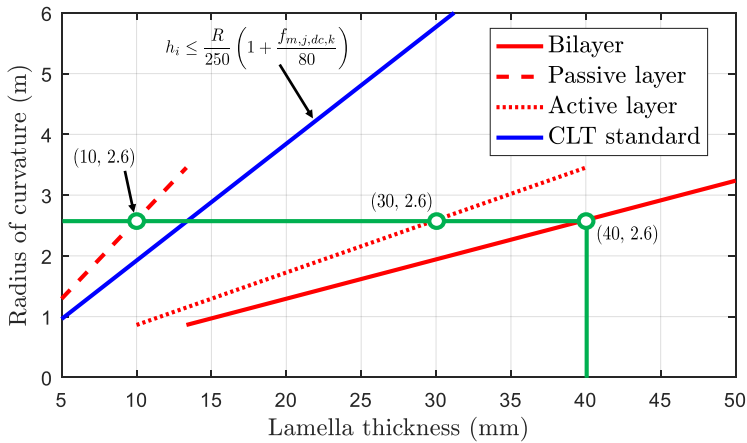


FIGURE 8.2: Comparison of achievable radii of curvatures of standard and self-shaped curved spruce CLT. Conventional CLT lamella thickness (h_i , blue line) calculated following recommendations of CLT standards *prEN16351* [168]. Hereby, R (mm) is the radius of curvature and $f_{m,j,dc,k}$ (MPa) is the declared characteristic value of bending strength of finger-jointed boards (assuming C24 grade wood, $f_{m,j,dc,k} \approx 24$ MPa [224]). Bilayer thickness ($h_1 + h_2$, red line) is calculated for spruce bilayers drying from 22 to 12% MC and with a constant layer-thickness ratio of $h_1 : h_2 = 1 : 3$ (using the plane-strain model from chapter 4 corrected by an underestimation of radius of 58%, according to the findings of chapter 6). Passive (h_1) and active (h_2) lamella thicknesses are shown separately. Green line and dots represent the 31 produced bilayer plates described in chapter 6, with an average achieved radius of 2.6 m.

bility to other self-shaping systems. Wood is a material readily usable for self-shaping at large scale thanks to its beneficial properties of anisotropy, hygroscopy, and strong mechanical properties. However, the shown studies and concepts directly apply to other synthetic materials at every length scale that possess these properties. The results of the investigations in this thesis showcase the strength and potential of applying biomimetic concepts to the engineering of materials. In this context, especially the concept of a system acting as autonomous actuator but later on, serving as form-stable structural element impressively demonstrates the combination of two functionalities.

8.4 OUTLOOK

8.4.1 *Fundamental level*

Further work of interest at a fundamental level, i.e. mainly on an experimental and modelling level in order to characterize wood mechanical behavior and to increase accuracy of the models, can be summarized as follows:

- Further characterization of wood deformation mechanisms, especially all diagonal and off-diagonal viscoelastic and mechanosorptive parameters of the respective orthotropic compliance tensors. The model used in this thesis still makes assumptions on some of the parameters by either scaling them by density from parameters available for other species, or by scaling them by the proportions of the elastic properties.
- Investigation of non-linearity in elastic behavior in certain parameters, especially transverse shear parameters of spruce wood because of the specific material behavior originating from the cellular microstructure.
- Investigation of effects of a residual stress state on moisture diffusion, moisture adsorption capacity, and swelling and shrinkage coefficients. These parameters have not yet been thoroughly characterized for wood in dependence of state variables such as the stress state for use in numerical modelling.
- Precise determination of probability density functions for every material parameter, to be used in uncertainty quantification and sensitivity analyses. An example of such a characterization is shown in chapter 5 in subsection S4 of section 5.7, for the swelling coefficients in the active layers.
- For dynamic systems: Investigation of the actuation fatigue behavior and reversibility for a large number of cycles and different bilayer configurations. Insight with respect to reversibility could indicate potential formation of damages during the actuation process, also in the case of just a single-time actuation as is necessary for the application of the self-shaping manufacturing process.

- Assessment of shaping behavior of wood bilayers made from different wood species in order to correlate wood-specific structural aspects with predictability of bilayer curvature. For instance, in hardwoods, if a dependency on diffuse- or ring-porosity can be observed, and in softwoods, if a dependency on density differences and width of early- and latewood layers can be observed.

In this thesis, it was shown that bilayer shaping represents an intriguing system of mechanical residual loads acting on wood and on the adhesive bond at the interface. At the same time, MC is changed by time-dependent diffusion phenomena, the bilayer bends, and as a result a complex residual stress state is formed. Both effects simultaneously impact deformation behavior and influence each-other. This degree of complexity is highly non-trivial in terms of experimental characterization and numerical modelling. Therefore, in terms of wood material modelling, the bilayer systems if modelled accurately, would represent a strong measure of validity of the model. A model capable of exactly predicting deformations with such complex phenomena would be highly desirable in every related field from classical wood materials science up to structural timber engineering and architecture.

8.4.2 *Applied level*

On a level relevant to industrial application in terms of using self-shaping wood for manufacturing of complex curved timber elements for architecture, the following points may be of future relevance:

- Assessment of effect of board quality specifics on shaping behavior. This could include, e.g. number and area of knots per given area, annual ring width and curvature, zones of rot and decay by fungi, in-situ fiber-flow along board length, and MC variation along the thickness and width of boards. Hand-in-hand, a powerful and automated recording and scanning strategy would need to be implemented into the sawmill production process, which would be in dynamic interaction with numerical prediction models for shape-change.
- The technical adaption of industrial drying kilns. In the *Urbach tower* project, boards were manually sorted by initial MC, which resulted in a broad distribution, due to the lack of possibility to technically dry wood to high initial MCs, e.g. to $> 22\%$. In fact, the interplay of

ventilation, air-flow parameters, temperature, relative humidity, and closed-loop monitoring in the drying kiln and its effect on the wood to be dried is non-trivial.

- The development of an automated computational design framework. Such a tool would allow for integrated design and, especially, backwards calculation of shape-change. A designer or engineer would be able to draw the desired complex curved part, which would then be analyzed by backwards FE simulations that locally decompose the structure into single initial flat building blocks and provide the exact lay-up and boundary conditions such as required MC change. Optimally, the implemented industrial production process would be dynamically adapted to the needs of each designed project with respect to the single building blocks necessitated. Ideally, the output of the computational tool would include direct sawmill requirements such as board quality or annual ring pattern in view of a lean production process. This aspect also includes the mentioned need of integrating design of self-shaping into form-finding design processes, e.g. as in the case of self-shaping gridshell structures.
- Optimization of processes in view of long-term cost minimization. Specifically, an automated sorting of boards with respect to quality, annual ring orientation, and MC with respect to a lean production process. Boards of inadequate quality would merely need to be distributed into parts, where for instance, curvature could be lower than the prediction. Or in other terms, models could be developed that allow curvature prediction by knowing specifics of board quality.
- Benchmarking studies and effective cost savings compared to different techniques of production of curved timber components. The difficulty lies in the assessment of standard form-giving processes of curved CLT. In fact, the process itself is not standardized but each manufacturer tends to have own methods and different cost calculations per final cubic meter of curved timber components. Here, especially the economics of scale would need to be considered. Specifically, the cost of investment in machines or tools required for the self-shaping production and their long-term benefits over investments into standard production means of curved components given a specific volume of demand.
- The manufacturing principles using the self-shaping method could also be applied to the wider field and to other materials besides

wood. The material system, irrespective of the scale and if not composed by two different materials, merely needs to possess similar properties, i.e. anisotropy in mechanical and expansive behavior. Especially the concept of a one-time actuation of a part subsequently rendered form-stable towards the stimuli is a promising concept. Examples could include one-time hydrogel actuators for soft robotics, the production of curved metallic parts, or again using wood, curved furniture design.

- In addition to static systems, also dynamic systems might be of interest in the timber building sector. For example, double-curved grid-shell structures could be used multiple times as non-permanent and mobile pavilion structures that are able to assemble but also disassemble themselves by a controlled change of relative humidity.

While these mentioned points yet represent non-trivial challenges to industry and engineering, the interplay between future complex digital fabrication and design can be regarded as highly promising in order to integrate such new aspects of manufacturing. Challenges such as the sorting, the scanning, the automated and inverse prediction of shape and of lay-up might not pose problems to future automated robotic systems. However, the idleness of the construction sector and the willingness of manufacturing companies to adapt towards production of timber with complex curved geometries can still be seen as the major challenge.

BIBLIOGRAPHY

1. Oliver, C. D., Nassar, N. T., Lippke, B. R. & McCarter, J. B. Carbon, Fossil Fuel, and Biodiversity Mitigation With Wood and Forests. *Journal of Sustainable Forestry* **33**, 248 (2014).
2. Schickhofer, G. *Starrer und nachgiebiger Verbund bei geschichteten, flächenhaften Holzstrukturen* PhD thesis (Technische Universität Graz, 1994).
3. Brandner, R. *Production and Technology of Cross Laminated Timber (CLT): A state-of-the-art Report* in (Focus Solid Timber Solutions - European Conference on Cross Laminated Timber (CLT), Graz, Austria, Volume 1, 2013).
4. Cornwall, W. Tall timber. *Science* **353**, 1354 (2016).
5. Menges, A., Schwinn, T. & Krieg, O. D. *Advancing Wood Architecture: A Computational Approach* (Routledge, 2016).
6. *Digital Wood Design: Innovative Techniques of Representation in Architectural Design* (eds Bianconi, F. & Filippucci, M.) (Springer International Publishing, 2019).
7. Rüggeberg, M. & Burgert, I. Bio-Inspired Wooden Actuators for Large Scale Applications. *Plos One* **10**, e0120718 (2015).
8. Correa, D., Papadopoulou, A., Guberan, C., Jhaveri, N., Reichert, S., Menges, A. & Tibbits, S. 3D-Printed Wood: Programming Hygroscopic Material Transformations. *3d Printing and Additive Manufacturing* **2**, 106 (2015).
9. Harlow, W. M., Côté, W. A. & Day, A. C. The Opening Mechanism of Pine Cone Scales. *Journal of Forestry* **62**, 538 (1964).
10. Gibson, L. J. The hierarchical structure and mechanics of plant materials. *Journal of The Royal Society Interface* **9**, 2749 (2012).
11. Hassani, M. M., Wittel, F. K., Hering, S. & Hermann, H. J. Rheological model for wood. *Computer Methods in Applied Mechanics and Engineering* **283**, 1032 (2015).

12. Kretschmann, D. E. in *Wood handbook — Wood as an engineering material (Centennial Edition)* (ed U.S. Department of Agriculture Forest Service, F. P. L.) 5,1 (General Technical Report FPL-GTR-190, Oxford, 2010).
13. Wagenführ, R. *Holzatlas (Sixth Edition)* (Fachbuchverlag Leipzig im Carl Hanser Verlag, 2007).
14. Armon, S., Efrati, E., Kupferman, R. & Sharon, E. Geometry and Mechanics in the Opening of Chiral Seed Pods. *Science* **333**, 1726 (2011).
15. Pezzulla, M., Smith, G. P., Nardinocchi, P. & Holmes, D. P. Geometry and mechanics of thin growing bilayers. *Soft Matter* **12**, 4435 (2016).
16. Sarikaya, M. An Introduction to Biomimetics - a Structural Viewpoint. *Microscopy Research and Technique* **27**, 360 (1994).
17. Vincent Julian F.V, Bogatyreva Olga A, Bogatyrev Nikolaj R, Bowyer Adrian & Pahl Anja-Karina. Biomimetics: its practice and theory. *Journal of The Royal Society Interface* **3**, 471 (2006).
18. Fratzl Peter. Biomimetic materials research: what can we really learn from nature's structural materials? *Journal of The Royal Society Interface* **4**, 637 (2007).
19. Da Vinci, L. Codex on the Flight of Birds (1505).
20. Lakes, R. Materials with structural hierarchy. En. *Nature* **361**, 511 (1993).
21. Srinivasan, A. V. Smart biological systems as models for engineered structures. *Materials Science & Engineering C-Biomimetic and Supramolecular Systems* **4**, 19 (1996).
22. Fratzl, P. & Weinkamer, R. Nature's hierarchical materials. *Progress in Materials Science* **52**, 1263 (2007).
23. Keckes, J., Burgert, I., Frühmann, K., Müller, M., Kölln, K., Hamilton, M., Burghammer, M., Roth, S. V., Stanzl-Tschegg, S. & Fratzl, P. Cell-wall recovery after irreversible deformation of wood. En. *Nature Materials* **2**, 810 (2003).
24. Gordon J. E., Jeronimidis G., Watt William, Harris B. & Ham A. C. Composites with high work of fracture. *Philosophical Transactions of the Royal Society of London. Series A, Mathematical and Physical Sciences* **294**, 545 (1980).

25. Marthin, O. & Gamstedt, E. K. Damage shielding mechanisms in hierarchical composites in nature with potential for design of tougher structural materials. *Royal Society Open Science* **6**, 181733 (2019).
26. Jeronimidis, G. & Atkins, A. Mechanics of Biological-Materials and Structures - Nature's Lessons for the Engineer. *Proceedings of the Institution of Mechanical Engineers Part C-Journal of Mechanical Engineering Science* **209**, 221 (1995).
27. John, G., Clements-Croome, D. & Jeronimidis, G. Sustainable building solutions: a review of lessons from the natural world. *Building and Environment* **40**, 319 (2005).
28. Gruber, P. & Jeronimidis, G. Has biomimetics arrived in architecture? *Bioinspiration & Biomimetics* **7**, 010201 (2012).
29. Menges, A. Biomimetic design processes in architecture: morphogenetic and evolutionary computational design. *Bioinspiration & Biomimetics* **7**, 015003 (2012).
30. Knippers, J. & Speck, T. Design and construction principles in nature and architecture. *Bioinspiration & Biomimetics* **7**, 015002 (2012).
31. Oda, R., Huc, I., Schmutz, M., Candau, S. J. & MacKintosh, F. C. Tuning bilayer twist using chiral counterions. *Nature* **399**, 566 (1999).
32. Dawson, J., Vincent, J. F. V. & Rocca, A. M. How pine cones open. *Nature* **390**, 668 (1997).
33. Le Duigou, A. & Castro, M. Evaluation of force generation mechanisms in natural, passive hydraulic actuators. *Scientific Reports* **6**, 18105 (2016).
34. Elbaum, R., Zaltzman, L., Burgert, I. & Fratzl, P. The Role of Wheat Awns in the Seed Dispersal Unit. *Science* **316**, 884 (2007).
35. Aharoni, H., Abraham, Y., Elbaum, R., Sharon, E. & Kupferman, R. Emergence of Spontaneous Twist and Curvature in Non-Euclidean Rods: Application to Erodium Plant Cells. *Physical Review Letters* **108**, 238106 (23 2012).
36. Skotheim, J. M. & Mahadevan, L. Physical Limits and Design Principles for Plant and Fungal Movements. *Science* **308**, 1308 (2005).
37. Burgert, I. & Fratzl, P. Actuation systems in plants as prototypes for bioinspired devices. *Philosophical Transactions of the Royal Society a-Mathematical Physical and Engineering Sciences* **367**, 1541 (2009).

38. Fratzl, P. & Barth, F. G. Biomaterial systems for mechanosensing and actuation. *Nature* **462**, 442 (2009).
39. Reyssat, E. & Mahadevan, L. Hygromorphs: from pine cones to biomimetic bilayers. *Journal of the Royal Society Interface* **6**, 951 (2009).
40. Harrington, M. J., Razghandi, K., Ditsch, F., Guiducci, L., Rueggeberg, M., Dunlop, J. W. C., Fratzl, P., Neinhuis, C. & Burgert, I. Origami-like unfolding of hydro-actuated ice plant seed capsules. *Nature Communications* **2**, 337 (2011).
41. Erb, R. M., Sander, J. S., Grisch, R. & Studart, A. R. Self-shaping composites with programmable bioinspired microstructures. *Nature Communications* **4**, 1712 (2013).
42. Le Duigou, A. & Castro, M. Moisture-induced self-shaping flax-reinforced polypropylene biocomposite actuator. *Industrial Crops and Products* **71**, 1 (2015).
43. Guiducci, L., Razghandi, K., Bertinetti, L., Turcaud, S., Rueggeberg, M., Weaver, J. C., Fratzl, P., Burgert, I. & Dunlop, J. W. C. Honeycomb Actuators Inspired by the Unfolding of Ice Plant Seed Capsules. *Plos One* **11**, e0163506 (2016).
44. Van Opdenbosch, D., Fritz-Popovski, G., Wagermaier, W., Paris, O. & Zollfrank, C. Moisture-Driven Ceramic Bilayer Actuators from a Biotemplating Approach. *Advanced Materials* **28**, 5235 (2016).
45. Poppinga, S., Zollfrank, C., Prucker, O., R  he, J., Menges, A., Cheng, T. & Speck, T. Toward a New Generation of Smart Biomimetic Actuators for Architecture. *Advanced Materials* **30**, 1703653 (2018).
46. Eder, M., Amini, S. & Fratzl, P. Biological composites—complex structures for functional diversity. *Science* **362**, 543 (2018).
47. Studart, A. R. & Erb, R. M. Bioinspired materials that self-shape through programmed microstructures. *Soft Matter* **10**, 1284 (2014).
48. Li, S. & Wang, K. W. Plant-inspired adaptive structures and materials for morphing and actuation: a review. *Bioinspiration & Biomimetics* **12**, 011001 (2017).
49. Huss, J. C., Fratzl, P., Dunlop, J. W. C., Merritt, D. J., Miller, B. P. & Eder, M. Protecting Offspring Against Fire: Lessons From Banksia Seed Pods. *Frontiers in Plant Science* **10**, 283 (2019).
50. Le Duigou, A., Chabaud, G., Scarpa, F. & Castro, M. Bioinspired Electro-Thermo-Hygro Reversible Shape-Changing Materials by 4D Printing. *Advanced Functional Materials* **0**, 1903280 (2019).

51. Timoshenko, S. Analysis of bi-metal thermostats. *Journal of the Optical Society of America* **11**, p. 233 (1925).
52. Lum, G. Z., Ye, Z., Dong, X., Marvi, H., Erin, O., Hu, W. & Sitti, M. Shape-programmable magnetic soft matter. *Proceedings of the National Academy of Sciences* **113**, E6007 (2016).
53. Pezzulla, M., Shillig, S. A., Nardinocchi, P. & Holmes, D. P. Morphing of geometric composites via residual swelling. *Soft Matter* **11**, 5812 (2015).
54. Siefert, E., Reyssat, E., Bico, J. & Roman, B. Bio-inspired pneumatic shape-morphing elastomers. *Nature Materials* **18**, 24+ (2019).
55. Neagu, R. C., Gamstedt, E. K. & Lindström, M. Influence of wood-fibre hygroexpansion on the dimensional instability of fibre mats and composites. *Composites Part A: Applied Science and Manufacturing* **36**, 772 (2005).
56. Reyssat, E. & Mahadevan, L. How wet paper curls. *EPL* **93**, 54001 (2011).
57. Svandberg, J. M. *Predictions of manufacturing induced shape distortions - high performance thermoset composites* PhD thesis (Luleå University of Technology, 2002).
58. Brauner, C. *Analysis of process-induced distortions and residual stresses of composite structures* PhD thesis (University of Bremen, 2013).
59. Forterre, Y., Skotheim, J. M., Dumais, J. & Mahadevan, L. How the Venus flytrap snaps. *Nature* **433**, 421 (2005).
60. O'Neill, B. in *Elementary Differential Geometry (Second Edition)* (ed O'Neill, B.) 202 (Academic Press, Boston, 2006).
61. Efrati, E., Sharon, E. & Kupferman, R. Elastic theory of unconstrained non-Euclidean plates. *Journal of the Mechanics and Physics of Solids* **57**, 762 (2009).
62. Ehret, A. E. *Introductory notes on the non-linear continuum mechanics of solids* (Handout to the lecture "Mechanics of soft materials and tissues", ETH Zürich, 2017).
63. Reddy, J. *Theory and Analysis of Elastic Plates and Shells* (Boca Raton: CRC Press, 2007).
64. Nardinocchi, P., Pezzulla, M. & Teresi, L. Anisotropic swelling of thin gel sheets. *Soft Matter* **11**, 1492 (2015).

65. Reichert, S., Menges, A. & Correa, D. Meteorosensitive architecture: Biomimetic building skins based on materially embedded and hygroscopically enabled responsiveness. *Computer-Aided Design* **60**, 50 (2015).
66. Wood, D., Correa Zuluaga, D., Krieg, O. & Menges, A. Material computation—4D timber construction: Towards building-scale hygroscopic actuated, self-constructing timber surfaces. *International Journal of Architectural Computing* **14** (2016).
67. Wood, D., Vailati, C., Menges, A. & Rüggeberg, M. Hygroscopically actuated wood elements for weather responsive and self-forming building parts – Facilitating upscaling and complex shape changes. *Construction and Building Materials* **165**, 782 (2018).
68. Holstov, A., Bridgens, B. & Farmer, G. Hygromorphic materials for sustainable responsive architecture. *Construction and Building Materials* **98**, 570 (2015).
69. Holstov, A., Farmer, G. & Bridgens, B. Sustainable Materialisation of Responsive Architecture. *Sustainability* **9**, 435 (2017).
70. Vailati, C. *Climate adaptive building solutions based on the autonomous movement of wooden bi-layered structures* PhD thesis (Eidgenössische Technische Hochschule ETH Zürich, Diss. No. 24912, 2018).
71. Vailati, C., Hass, P., Burgert, I. & Rüggeberg, M. Upscaling of wood bilayers: design principles for controlling shape change and increasing moisture change rate. *Materials and Structures* **50**, 250 (2017).
72. Vailati, C., Bachtar, E., Hass, P., Burgert, I. & Rüggeberg, M. An autonomous shading system based on coupled wood bilayer elements. *Energy And Buildings* **158**, 1013 (2018).
73. Vailati, C., Rüggeberg, M., Burgert, I. & Hass, P. The kinetics of wooden bilayers is not affected by different wood adhesive systems. *Wood Science And Technology* **52**, 1589 (2018).
74. Abdelmohsen, S., Adriaenssens, S., El-Dabaa, R., Gabriele, S., Olivieri, L. & Teresi, L. A multi-physics approach for modeling hygroscopic behavior in wood low-tech architectural adaptive systems. *Computer-Aided Design* **106**, 43 (2019).
75. Ashby, M. F. in *Materials Selection in Mechanical Design (Fourth Edition)* (ed Ashby, M. F.) 57 (Butterworth-Heinemann, Oxford, 2011).

76. Harrington, J. J. *Hierarchical modelling of softwood hygro-elastic properties* PhD thesis (University of Canterbury, Christchurch, New Zealand, 2002).
77. Reiterer, A., Lichtenegger, H., Tschegg, S. & Fratzl, P. Experimental evidence for a mechanical function of the cellulose microfibril angle in wood cell walls. *Philosophical Magazine A* **79**, 2173 (1999).
78. Burgert, I. Exploring the micromechanical design of plant cell walls. *American Journal of Botany* **93**, 1391 (2006).
79. Caudullo, G., Welk, E. & San-Miguel-Ayanz, J. Chorological maps for the main European woody species. *Data in Brief* **12**, 662 (2017).
80. Sell, J. *Eigenschaften und Kenngrößen von Holzarten* (Fourth Edition) (Baufachverlag Lignum, Zürich, 2000).
81. Fredriksson, M. On Wood-Water Interactions in the Over-Hygroscopic Moisture Range-Mechanisms, Methods, and Influence of Wood Modification. *Forests* **10** (2019).
82. Thybring, E. E., Kymalainen, M. & Rautkari, L. Experimental techniques for characterising water in wood covering the range from dry to fully water-saturated. *Wood Science and Technology* **52**, 297 (2018).
83. Fredriksson, M. & Thybring, E. E. Scanning or desorption isotherms? Characterising sorption hysteresis of wood. *Cellulose* **25**, 4477 (2018).
84. Engelund, E. T., Thygesen, L. G., Svensson, S. & Hill, C. A. S. A critical discussion of the physics of wood–water interactions. *Wood Science and Technology* **47**, 141 (2013).
85. Kulasinski, K. *Physical and Mechanical Aspects of Moisture Adsorption in Wood Biopolymers Investigated with Atomistic Simulations* PhD thesis (Eidgenössische Technische Hochschule ETH Zürich, Diss. No. 23046, 2015).
86. Bertinetti, L., Fratzl, P. & Zemb, T. Chemical, colloidal and mechanical contributions to the state of water in wood cell walls. *New Journal of Physics* **18**, 083048 (2016).
87. Willems, W. Hygroscopic wood moisture: single and dimerized water molecules at hydroxyl-pair sites? *Wood Science and Technology* **52**, 777 (2018).
88. Zelinka, S. L., Glass, S. V. & Thybring, E. E. Myth versus reality: Do parabolic sorption isotherm models reflect actual wood-water thermodynamics? *Wood Science and Technology* **52**, 1701 (2018).

89. Chen, M., Zhang, C., Shomali, A., Coasne, B., Carmeliet, J. & Derome, D. Wood–Moisture Relationships Studied with Molecular Simulations: Methodological Guidelines. *Forests* **10** (2019).
90. Thommes, M., Kaneko, K., Neimark, A. V., Olivier, J. P., Rodriguez-Reinoso, F., Rouquerol, J. & Sing, K. S. Physisorption of gases, with special reference to the evaluation of surface area and pore size distribution (IUPAC Technical Report). *Pure and Applied Chemistry* **87**, 1051 (2015).
91. Chen, M., Coasne, B., Guyer, R., Derome, D. & Carmeliet, J. Role of hydrogen bonding in hysteresis observed in sorption-induced swelling of soft nanoporous polymers. *En. Nature Communications* **9**, 3507 (2018).
92. Salmén, L. & Larsson, P. A. On the origin of sorption hysteresis in cellulosic materials. *Carbohydrate Polymers* **182**, 15 (2018).
93. Rémond, R., Almeida, G. & Perré, P. The gripped-box model: A simple and robust formulation of sorption hysteresis for lignocellulosic materials. *Construction and Building Materials* **170**, 716 (2018).
94. Grönquist, P., Frey, M., Keplinger, T. & Burgert, I. Mesoporosity of Delignified Wood Investigated by Water Vapor Sorption. *ACS Omega* **4**, 12425 (2019).
95. Mörrath, E. Beiträge zur Kenntnis der Quellungserscheinungen des Buchenholzes. de. *Kolloid-Beihfte* **33**, 131 (1931).
96. Skaar, C. *Wood-Water Relations* (Springer-Verlag, Berlin Heidelberg, 1988).
97. Nopens, M., Riegler, M., Hansmann, C. & Krause, A. Simultaneous change of wood mass and dimension caused by moisture dynamics. *Scientific Reports* **9** (2019).
98. U.S. Department of Agriculture Forest Service, F. P. L. *Wood handbook — Wood as an engineering material (Centennial Edition)* (General Technical Report FPL-GTR-190, Madison, 2010).
99. Bachtiar, E. V. *Material characterization of wood, adhesive and coating of cultural heritage under various climatic conditions* PhD thesis (Eidgenössische Technische Hochschule ETH Zürich, Diss. No. 24727, 2017).
100. Hering, S. *Charakterisierung und Modellierung der Materialeigenschaften von Rotbuchenholz zur Simulation von Holzverklebungen* PhD thesis (Eidgenössische Technische Hochschule ETH Zürich, Diss. No. 19903, 2011).

101. Speck, T. & Burgert, I. Plant Stems: Functional Design and Mechanics. *Annual Review of Materials Research* **41**, 169 (2011).
102. Conners, T. E. & Medvecz, P. J. Wood as bimodular material. *Wood and Fiber Science* **24**, 413 (1992).
103. Niemz, P. & Sonderegger, W. *Holzphysik: Physik des Holzes und der Holzwerkstoffe* (Fachbuchverlag Leipzig im Carl Hanser Verlag, 2017).
104. Grimsel, M. *Mechanisches Verhalten von Holz: Struktur- und Parameteridentifikation eines anisotropen Werkstoffes* PhD thesis (TU Dresden, Germany, 1999).
105. Keunecke, D., Hering, S. & Niemz, P. Three-dimensional elastic behaviour of common yew and Norway spruce. *Wood Science and Technology* **42** (2008).
106. Hering, S., Keunecke, D. & Niemz, P. *Visualising anisotropic material properties of different wood species* (Poster at ETH Zürich, Institute for Building Materials, 2013).
107. Hassani, M. M. *Adhesive Bonding of Structural Hardwood Elements* PhD thesis (Eidgenössische Technische Hochschule ETH Zürich, Diss. No. 22900, 2015).
108. Richardson, E. J. *A Multiphysics Finite Element Model of the Wood Cell Wall* PhD thesis (University of Glasgow, 2018).
109. Füssl, J., Lukacevic, M., Pillwein, S. & Pottmann, H. *Computational Mechanical Modelling of Wood—From Microstructural Characteristics Over Wood-Based Products to Advanced Timber Structures*. In: Bianconi F., Filippucci M. (eds) *Digital Wood Design. Lecture Notes in Civil Engineering* (Springer International Publishing, Cham, 2019).
110. Bathe, K. J. *Finite element procedures (second edition)* (Bathe, K. J., Waternertown, MA, 2006).
111. Ozyhar, T., Hering, S. & Niemz, P. Moisture-dependent elastic and strength anisotropy of European beech wood in tension. *Journal of Materials Science* **47**, 6141 (2012).
112. Ozyhar, T., Hering, S. & Niemz, P. Moisture-dependent orthotropic tension-compression asymmetry of wood. *Holzforschung* **67**, 395 (2013).
113. Ozyhar, T., Hering, S., Sanabria, S. J. & Niemz, P. Determining moisture-dependent elastic characteristics of beech wood by means of ultrasonic waves. *Wood Science and Technology* **47**, 329 (2013).

114. Ozyhar, T., Hering, S. & Niemz, P. Viscoelastic characterization of wood: Time dependence of the orthotropic compliance in tension and compression. *Journal of Rheology* **57**, 699 (2013).
115. Hering, S., Keunecke, D. & Niemz, P. Moisture-dependent orthotropic elasticity of beech wood. *Wood Science and Technology* **46**, 927 (2012).
116. Hering, S. & Niemz, P. Moisture-dependent, viscoelastic creep of European beech wood in longitudinal direction. *European Journal of Wood and Wood Products* **70**, 667 (2012).
117. Hering, S., Saft, S., Resch, E., Niemz, P. & Kaliske, M. Characterisation of moisture-dependent plasticity of beech wood and its application to a multi-surface plasticity model. *Holzforschung* **66**, 373 (2012).
118. Hanhijärvi Antti & Mackenzie-Helnwein Peter. Computational Analysis of Quality Reduction during Drying of Lumber due to Irrecoverable Deformation. I: Orthotropic Viscoelastic-Mechanosorptive-Plastic Material Model for the Transverse Plane of Wood. *Journal of Engineering Mechanics* **129**, 996 (2003).
119. Fortino, S., Mirianon, F. & Toratti, T. A 3D moisture-stress FEM analysis for time dependent problems in timber structures. *Mechanics of Time-Dependent Materials* **13**, 333 (2009).
120. Reichel, S. *Modellierung und Simulation hygro-mechanisch beanspruchter Strukturen aus Holz im kurz- und Langzeitbereich* PhD thesis (TU Dresden, Germany, 2015).
121. Hassani, M. M., Wittel, F. K., Ammann, S., Niemz, P. & Herrmann, H. J. Moisture-induced damage evolution in laminated beech. *Wood Science and Technology* **50**, 917 (2016).
122. Schwiedrzik, J., Raghavan, R., Rüggeberg, M., Hansen, S., Wehrs, J., Adusumalli, R. B., Zimmermann, T. & Michler, J. Identification of polymer matrix yield stress in the wood cell wall based on micropillar compression and micromechanical modelling. *Philosophical Magazine* **96**, 3461 (2016).
123. Nairn, J. Material point method simulations of transverse fracture in wood with realistic morphologies. *Holzforschung* **61** (2007).
124. Rafsanjani Abbasi, A. *Multiscale poroelastic model: Bridging the gap from cellular to macroscopic scale* PhD thesis (Eidgenössische Technische Hochschule ETH Zürich, Diss. No. 20821, 2013).

125. Füssl, J., Bader, T. & Eberhardsteiner, J. Computational Mechanics for Advanced Timber Engineering. *IACM expressions* **32**, 6 (2012).
126. Füssl, J., Lukacevic, M., Kandler, G. & Eberhardsteiner, J. A Comprehensive Mechanical Modeling Approach for the Design of Wood-Based Products. *IACM expressions* **35**, 8 (2014).
127. Qing, H. & Mishnaevsky, L. 3D hierarchical computational model of wood as a cellular material with fibril reinforced, heterogeneous multiple layers. *Mechanics of Materials* **41**, 1034 (2009).
128. Bader, T., Hofstetter, K., Hellmich, C. & Eberhardsteiner, J. Poromechanical scale transitions of failure stresses in wood: from the lignin to the spruce level. *ZAMM - Journal of Applied Mathematics and Mechanics / Zeitschrift für Angewandte Mathematik und Mechanik* **90**, 750 (2010).
129. Gamstedt, E. K., Bader, T. K. & de Borst, K. Mixed numerical–experimental methods in wood micromechanics. *Wood Science and Technology* **47**, 183 (2013).
130. Füssl, J., Li, M., Lukacevic, M., Eberhardsteiner, J. & Martin, C. Comparison of unit cell-based computational methods for predicting the strength of wood. *Engineering Structures* **141**, 427 (2017).
131. Mora Mendez, D. F., Olaniran, S. O., Rüggeberg, M., Burgert, I., Herrmann, H. J. & Wittel, F. K. Mechanical behavior of chemically modified Norway spruce: a generic hierarchical model for wood modifications. *Wood Science and Technology* **53**, 447 (2019).
132. Diaconu, D., Wassenberg, M. & Spiecker, H. Variability of European beech wood density as influenced by interactions between tree-ring growth and aspect. *Forest Ecosystems* **3**, 6 (2016).
133. Sobol, I. M. Sensitivity Estimates for Nonlinear Mathematical Models. *Mathematical Modelling and Computational Experiments* **1**, 407 (1993).
134. Sobol, I. M. & Kucherenko, S. S. Global sensitivity indices for nonlinear mathematical models. Review. *Wilmott Magazine* **1**, 56 (2005).
135. Marelli, S. & Sudret, B. UQLab: A Framework for Uncertainty Quantification in Matlab. *Proc. 2nd Int. Conf. on Vulnerability, Risk Analysis and Management, Liverpool, United Kingdom. Proceedings* 2554 (2014).
136. Zimin, Y., Ueda, T. & Pawłat, J. Energy distribution of residual stresses in bi-layer structure. *Przegląd elektrotechniczny* **6**, 111 (2012).

137. Nairn, J. A. Cross laminated timber properties including effects of non-glued edges and additional cracks. *European Journal of Wood and Wood Products* **75**, 973 (2017).
138. Hutchinson, J. W. & Suo, Z. in *Advances in Applied Mechanics* (eds Hutchinson, J. W. & Wu, T. Y.) 63 (Elsevier, 1991).
139. Evans, A. G. & Hutchinson, J. W. The thermomechanical integrity of thin films and multilayers. *Acta Metallurgica et Materialia* **43**, 2507 (1995).
140. Tibbits, S. 4D Printing: Multi-Material Shape Change. *Architectural Design* **84**, 116 (2014).
141. Yang, Y., Song, X., Li, X., Chen, Z., Zhou, C., Zhou, Q. & Chen, Y. Recent Progress in Biomimetic Additive Manufacturing Technology: From Materials to Functional Structures. *Advanced Materials* **30**, 1706539 (2018).
142. Mitchell, A., Lafont, U., Hołyńska, M. & Semprimoschnig, C. Additive manufacturing — A review of 4D printing and future applications. *Additive Manufacturing* **24**, 606 (2018).
143. Morimoto, T. & Ashida, F. Temperature-responsive bending of a bilayer gel. *International Journal of Solids and Structures* **56-57**, 20 (2015).
144. Drozdov, A. D. & Christiansen, J. d. Swelling-induced bending of bilayer gel beams. *Composite Structures* **153**, 961 (2016).
145. Nardinocchi, P. & Puntel, E. Finite bending solutions for layered gel beams. *International Journal of Solids and Structures* **90**, 228 (2016).
146. Grönquist, P., Wittel, F. K. & Rüggeberg, M. Modeling and design of thin bending wooden bilayers. *PLoS One* **13**, e0205607 (2018).
147. Brandmair, A., Jans, N., Clauss, S., Hass, P. & Niemz, P. Bonding of hardwoods with 1C PUR adhesives for timber construction. *Bauphysik* **34**, 210 (2012).
148. Casdorff, K., Klausler, O., Gabriel, J., Amen, C., Lehringer, C., BURGERT, I. & Keplinger, T. About the influence of a water-based priming system on the interactions between wood and one-component polyurethane adhesive studied by atomic force microscopy and confocal Raman spectroscopy imaging. *International Journal of Adhesion and Adhesives* **80**, 52 (2018).
149. Blatman, G. & Sudret, B. Adaptive sparse polynomial chaos expansion based on least angle regression. *Journal of Computational Physics* **230**, 2345 (2011).

150. Konakli, K. & Sudret, B. Global sensitivity analysis using low-rank tensor approximations. *Reliability Engineering & System Safety* **156**, 64 (2016).
151. Sudret, B., Marelli, S. & Wiart, J. in *2017 11th European Conference on Antennas and Propagation (eucaap)* 793 (Ieee, New York, 2017).
152. Sudret, B. & Mai, C. V. Computing derivative-based global sensitivity measures using polynomial chaos expansions. *Reliability Engineering & System Safety* **134**, 241 (2015).
153. Grönquist, P., Wood, D., Hassani, M. M., Wittel, F. K., Menges, A. & Rüggeberg, M. Analysis of hygroscopic self-shaping wood at large scale for curved mass timber structures. *Science Advances* **5** (2019).
154. Guo, H., Klose, D., Hou, Y., Jeschke, G. & Burgert, I. Highly Efficient UV Protection of the Biomaterial Wood by A Transparent TiO₂/Ce Xerogel. *ACS Applied Materials & Interfaces* **9**, 39040 (2017).
155. Aldinger, L., Bechert, S., Wood, D., Knippers, J. & Menges, A. *Design and Structural Modelling of Surface-Active Timber Structures Made from Curved CLT - Urbach Tower, Remstal Gartenschau 2019* in *Impact: Design With All Senses* (eds Gengnagel, C., Baverel, O., Burry, J., Ramsgaard Thomsen, M. & Weinzierl, S.) (Springer International Publishing, Cham, 2020), 419.
156. ICD University of Stuttgart. *Urbach tower: Online project description*. URL: <https://icd.uni-stuttgart.de/?p=23336>
157. DIN EN 1995-1-1/A2:2014-07. *Eurocode 5: Design of timber structures - Part 1-1: General - Common rules and rules for buildings; German version EN 1995-1-1:2004/A2:2014* (Beuth Verlag GmbH, 2014).
158. Trübswetter, T. *Holztrocknung: Verfahren zur Trocknung von Schnittholz – Planung von Trocknungsanlagen* (Carl Hanser Verlag GmbH, 2009).
159. Galuppi, L. & Royer-Carfagni, G. Localized contacts, stress concentrations and transient states in bent-lamination with viscoelastic adhesion. An analytical study. *International Journal of Mechanical Sciences* **103**, 275 (2015).
160. Hellmayr, R. *Untersuchen des Einflusses der Jahrringneigung und der Jahrringstellung auf die Voraussagbarkeit der Krümmung von Holzbilayern mit FE Modellen* tech. rep. (Internship report, Eidgenössische Technische Hochschule ETH Zürich, Institute for Building Materials, 2018).

161. Gao, M. *Identification of nonlinear behavior in spruce bilayer deformation* tech. rep. (MSc project thesis, Eidgenössische Technische Hochschule ETH Zürich, Institute for Building Materials, 2019).
162. Grönquist, P., Wittel, F. K. & Rüggeberg, M. *Upscaling of self-actuated wooden bilayers* in (Proceedings of the 7th GACM Colloquium on Computational Mechanics for Young Scientists from Academia and Industry, Stuttgart, Germany, 2017).
163. Stecher, G., Maderebner, R., Zingerle, P., Flach, M. & Kraler, A. *Curved cross-laminated timber elements* in (World Conference on Timber Engineering (WCTE) 2016, Vienna, Austria, 2014).
164. Bockel, S., Mayer, I., Konnerth, J., Niemz, P., Swaboda, C., Beyer, M., Harling, S., Weiland, G., Bieri, N. & Pichelin, F. Influence of wood extractives on two-component polyurethane adhesive for structural hardwood bonding. *The Journal of Adhesion* **94**, 829 (2018).
165. DIN 52186:1978-06. *Testing of wood; bending test* (Beuth Verlag GmbH, 1978).
166. Marti, P. *Theory of Structures: Fundamentals, Framed Structures, Plates and Shells* (Ernst & Sohn GmbH & Co. KG, 2013).
167. DIN 52187:1979-05. *Testing of wood; determination of ultimate shearing stress parallel to grain* (Beuth Verlag GmbH, 1979).
168. DIN EN 16351:2018-12 - Draft. *Timber structures - Cross laminated timber - Requirements; German and English version prEN 16351:2018* (Beuth Verlag GmbH, 2018).
169. DIN EN 14358:2016-11. *Timber structures - Calculation and verification of characteristic values; German version EN 14358:2016* (Beuth Verlag GmbH, 2016).
170. Thérien-Aubin, H., Moshe, M., Sharon, E. & Kumacheva, E. Shape transformations of soft matter governed by bi-axial stresses. *Soft Matter* **11**, 4600 (23 2015).
171. Huang, H.-W., Sakar, M. S., Petruska, A. J., Pané, S. & Nelson, B. J. Soft micromachines with programmable motility and morphology. *Nature Communications* **7**, 12263 (2016).
172. Sydney Gladman, A., Matsumoto, E. A., Nuzzo, R. G., Mahadevan, L. & Lewis, J. A. Biomimetic 4D printing. *Nature Materials* **15**, 413 (2016).

173. Van Manen, T., Janbaz, S. & Zadpoor, A. A. Programming the shape-shifting of flat soft matter. *Materials Today* **21**, 144 (2018).
174. Troyano, J., Carné-Sánchez, A. & MasPOCH, D. Programmable Self-Assembling 3D Architectures Generated by Patterning of Swellable MOF-Based Composite Films. *Advanced Materials* **31**, 1808235 (2019).
175. Scholz, R., Langhansl, M., Zollfrank, C. & Walther, F. Experimental study on the actuation and fatigue behavior of the biopolymeric material Cottonid. *Materials Today: Proceedings. 1st International Conference on Materials, Mimicking, Manufacturing from and for Bio Application (BioM&M)*, 27-29 June 2018 **7**, 476 (2019).
176. Le Duigou, A., Keryvin, V., Beaugrand, J., Pernes, M., Scarpa, F. & Castro, M. Humidity responsive actuation of bioinspired hygro-morph biocomposites (HBC) for adaptive structures. *Composites Part A: Applied Science and Manufacturing* **116**, 36 (2019).
177. Péron, M., Céline, A., Castro, M., Jacquemin, F. & Duigou, A. L. Study of hygroscopic stresses in asymmetric biocomposite laminates. *Composites Science and Technology* **169**, 7 (2019).
178. Schmied, J. U., Ferrand, H. L., Ermanni, P., Studart, A. R. & Arrieta, A. F. Programmable snapping composites with bio-inspired architecture. *Bioinspiration & Biomimetics* **12**, 026012 (2017).
179. Riley, K. S., Ferrand, H. L. & Arrieta, A. F. Modeling of snapping composite shells with magnetically aligned bio-inspired reinforcements. *Smart Materials and Structures* **27**, 114003 (2018).
180. Wojcik, M. in *Rethinking Wood - Future Dimensions of Timber Assembly* (eds Hudert, M. & Pfeiffer, S.) 251 (Birkhäuser, Basel, 2019).
181. Harris, R., Romer, J., Kelly, O. & Johnson, S. Design and construction of the Downland Gridshell. *Building Research & Information* **31**, 427 (2003).
182. Tayeb, F., Baverel, O., Caron, J.-F. & du Peloux, L. *Construction of gridshells composed of elastically bended elements and covered by a stretched three-dimensional membrane in Structural Membranes 2013* (Munich, Germany, 2013).
183. Naicu, D., Harris, R. & Williams, C. *Timber gridshells: Design methods and their application to a temporary pavilion in* (Quebec City, Canada, 2014).

184. Quinn, G. & Gengnagel, C. A Review Of Elastic Grid Shells, Their Erection Methods And The Potential Use Of Pneumatic Formwork. *In: Mobile and Rapidly Assembled Structures IV* **136**, 129 (2014).
185. Liddell, I. Frei Otto and the development of gridshells. *Case Studies in Structural Engineering* **4**, 39 (2015).
186. Du Peloux, L., Tayeb, F., Baverel, O. & Caron, J.-F. Construction of a Large Composite Gridshell Structure: A Lightweight Structure Made with Pultruded Glass Fibre Reinforced Polymer Tubes. *Structural Engineering International* **26**, 160 (2016).
187. Ghiyasinasab, M., Lehoux, N. & Menard, S. Production Phases and Market for Timber Gridshell Structures: A State-of-the-Art Review. *Bioresources* **12**, 9538 (2017).
188. Hansen, K. K. *Sorption isotherms: A catalogue* tech. rep. Kgs. Lyngby, Denmark: Technical University of Denmark. Byg Rapport, No. TR-162 (1986).
189. Lienhard, J., Alpermann, H., Gengnagel, C. & Knippers, J. Active Bending, a Review on Structures where Bending is Used as a Self-Formation Process. *International Journal of Space Structures* **28**, 187 (2013).
190. Pone, S., Colabella, S., DAmico, B., Fiore, A., Lancia, D. & Parenti, B. Timber Post-formed Gridshell: Digital Form-finding / drawing and building tool. *Proceedings of IASS Annual Symposia* **2013**, 1 (2013).
191. Quinn, G. & Gengnagel, C. in *Modelling Behaviour* (eds Thomsen, M., Tamke, M., Gengnagel, C., Faircloth, B. & Scheurer, F.) 257 (Springer, Cham, 2015).
192. Baseta, E. & Bollinger, K. Construction system for reversible self-formation of gridshells: Correspondence between physical and digital form. *ACADIA 2018 - Re/calibration: on imprecision and infidelity, At Universidad Iberoamericana, Mexico City, Mexico* (2018).
193. Collins, M., Cosgrove, T. & Mellad, A. Characterisation of OSB properties for application in gridshells. *Materials and Structures* **50** (2017).
194. Lara-Bocanegra, A. J., Majano-Majano, A., Arriaga, F. & Guaita, M. Long-term bending stress relaxation in timber laths for the structural design of lattice shells. *Construction and Building Materials* **193**, 565 (2018).
195. Bulenda, T. & Knippers, J. Stability of grid shells. *Computers & Structures* **79**, 1161 (2001).

196. Baek, C., Sageman-Furnas, A. O., Jawed, M. K. & Reis, P. M. Form finding in elastic gridshells. *Proceedings of the National Academy of Sciences* **115**, 75 (2018).
197. Charest, P., Potvin, A., Demers, C. M. H. & Menard, S. Assessing the Complexity of Timber Gridshells in Architecture through Shape, Structure, and Material Classification. *BioResources* **14**, 1364 (2019).
198. D'Amico, B., Kermani, A. & Zhang, H. Form finding and structural analysis of actively bent timber grid shells. *Engineering Structures* **81**, 195 (2014).
199. D'Amico, B., Kermani, A., Zhang, H., Shepherd, P. & Williams, C. Optimization of cross-section of actively bent grid shells with strength and geometric compatibility constraints. *Computers Structures* **154**, 163 (2015).
200. Mesnil, R., Douthe, C. & Baverel, O. Non-Standard Patterns for Grid-shell Structures: Fabrication and Structural Optimization. *Journal of the International Association for Shell and Spatial Structures* **58**, 277 (2017).
201. Collins, M. & Cosgrove, T. Dynamic relaxation modelling of braced bending active gridshells with rectangular sections. *Engineering Structures* **187**, 16 (2019).
202. Rombouts, J., Lombaert, G., De Laet, L. & Schevenels, M. A novel shape optimization approach for strained gridshells: Design and construction of a simply supported gridshell. *Engineering Structures* **192**, 166 (2019).
203. Tomasello, G., Adriaenssens, S. & Gabriele, S. Dynamic behavior of form-found shell structures according to Modal and Dynamic Funicularity. *Engineering Structures* **198**, 109521 (2019).
204. Li, J.-M. & Knippers, J. *Form-finding of grid shells with continuous elastic rods* in (London, UK, 2011).
205. Lanvermann, C. *Sorption and swelling within growth rings of Norway spruce and implications on the macroscopic scale* PhD thesis (Eidgenössische Technische Hochschule ETH Zürich, Diss. No. 21761, 2014).
206. Rafsanjani, A., Lanvermann, C., Niemz, P., Carmeliet, J. & Derome, D. Multiscale analysis of free swelling of Norway spruce. *Composites Part A: Applied Science and Manufacturing* **54**, 70 (2013).

207. Patera, A., Van den Bulcke, J., Boone, M. N., Derome, D. & Carmeliet, J. Swelling interactions of earlywood and latewood across a growth ring: global and local deformations. *Wood Science and Technology* **52**, 91 (2018).
208. Crank, J. A theoretical investigation of the influence of molecular relaxation and internal stress on diffusion in polymers. *Journal of Polymer Science* **11**, 151 (1953).
209. Neumann, S. & Marom, G. Prediction of Moisture Diffusion Parameters in Composite Materials Under Stress. *Journal of Composite Materials* **21**, 68 (1987).
210. Thybring, E. E., Glass, S. V. & Zelinka, S. L. Kinetics of Water Vapor Sorption in Wood Cell Walls: State of the Art and Research Needs. *Forests* **10** (2019).
211. Konopka, D. & Kaliske, M. Transient multi-FICKian hygro-mechanical analysis of wood. *Computers & Structures* **197**, 12 (2018).
212. Baensch, F. *Damage evolution in wood and layered wood composites monitored in situ by acoustic emission, digital image correlation and synchrotron based tomographic microscopy* PhD thesis (Eidgenössische Technische Hochschule ETH Zürich, Diss. No. 22372, 2015).
213. Burgert, I., Eder, M., Gierlinger, N. & Fratzl, P. Tensile and compressive stresses in tracheids are induced by swelling based on geometrical constraints of the wood cell. *Planta* **226**, 981 (2007).
214. Joffre, T., Neagu, R. C., Bardage, S. L. & Gamstedt, E. K. Modelling of the hygroelastic behaviour of normal and compression wood tracheids. *Journal of Structural Biology* **185**, 89 (2014).
215. DIN EN 338:2016-07. *Structural timber - Strength classes; German version EN 338:2016* (Beuth Verlag GmbH, 2016).
216. Hanhijärvi, A. & Ranta-Maunus, A. *Development of strength grading of timber using combined measurement techniques* (Report of the Combigrade-project - phase 2. Espoo 2008. VTT Publications 686, 2008).
217. Nairn, J. A. Predicting layer cracks in cross-laminated timber with evaluations of strategies for suppressing them. *European Journal of Wood and Wood Products* **77**, 405 (2019).
218. Gereke, T., Gustafsson, P. J., Persson, K. & Niemz, P. Experimental and numerical determination of the hygroscopic warping of cross-laminated solid wood panels. *Holzforschung* **63**, 340 (2009).

219. Gereke, T. & Niemz, P. Moisture-induced stresses in spruce cross-laminates. *Engineering Structures* **32**, 600 (2010).
220. Sikora, K. S., McPolin, D. O. & Harte, A. M. Shear Strength and Durability Testing of Adhesive Bonds in Cross-laminated Timber. *The Journal of Adhesion* **92**, 758 (2016).
221. Knorz, M., Torno, S. & van de Kuilen, J.-W. Bonding quality of industrially produced cross-laminated timber (CLT) as determined in delamination tests. *Construction and Building Materials* **133**, 219 (2017).
222. Aicher, S. & Reinhardt, H. W. Delaminierungseigenschaften und Scherfestigkeiten von verklebten rotkernigen Buchenholzlamellen. *Holz als Roh- und Werkstoff* **65**, 125 (2007).
223. Schmidt, M., Glos, P. & Wegener, G. Verklebung von Buchenholz für tragende Holzbauteile. *European Journal of Wood and Wood Products* **68**, 43 (2010).
224. Aicher, S. *Geklebte Verbindungen in Holzbauprodukten und -tragwerken* in (46. Fortbildungskurs, Swiss Wood Innovation Network, Holzverbindungen mit Klebstoffen für die Bauanwendung 2014, Weinfielden, Switzerland, 2014).
225. Ehrhart, T. *European beech glued laminated timber* PhD thesis (Eidgenössische Technische Hochschule ETH Zürich, Diss. No. 26173, 2019).

CURRICULUM VITAE

PERSONAL DATA

Name	Philippe Grönquist
Date of Birth	June 17, 1990
Place of Birth	Zug (ZG), Switzerland
Citizen of	Zug (ZG), Switzerland

EDUCATION

2016 – 2019	PhD student at the Laboratory for Cellulose & Wood Materials, <i>Swiss Federal Laboratories for Materials Science and Technology</i> , Dübendorf, Switzerland
2009 – 2016	Undergraduate and graduate studies in civil engineering, <i>Swiss Federal Institute of Technology</i> , Zürich, Switzerland <i>Final degree:</i> BSc & MSc ETH Civil Eng
2006 – 2009	<i>Kantonsschule Zürcher Unterland</i> , Bülach, Switzerland <i>Final degree:</i> Matura (university entrance diploma)
2005 – 2006	<i>Collège Calvin</i> , Genève, Switzerland
2002 – 2005	<i>Cycle d’Orientation de la Gradelle</i> , Chêne-Bougeries, Switzerland

EMPLOYMENT

2010 – 2017	Compulsory military service, Grenadier at Special Forces Command, <i>Swiss Armed Forces</i> , Switzerland
2014	Internship, Construction management, <i>Losinger Marazzi AG</i> , Zürich, Switzerland

PUBLICATIONS

ARTICLES PUBLISHED IN ISI PEER-REVIEWED JOURNALS

1. Mahrt, F., Marcolli, C., David, R. O., **Grönquist, P.**, Barthazy Meier, E. J., Lohmann, U. & Kanji, Z. A. Ice nucleation abilities of soot particles determined with the Horizontal Ice Nucleation Chamber. *Atmospheric Chemistry and Physics*, 18(18), 13363-13392, (2018), <https://doi.org/10.5194/acp-18-13363-2018>.
2. **Grönquist, P.**, Wittel, F. K. & Rüggeberg, M. Modeling and design of thin bending wooden bilayers. *PLoS ONE*, 13(10), e0205607, (2018), <https://doi.org/10.1371/journal.pone.0205607>.
3. **Grönquist, P.**, Schnider, T., Thoma, A., Gramazio, F., Kohler, M., Burgert, I. & Rüggeberg, M. Investigations on densified beech wood for application as a swelling dowel in timber joints. *Holzforschung*, 73(6), 559–568, (2019), <https://doi.org/10.1515/hf-2018-0106>.
4. **Grönquist, P.***, Frey, M.*, Keplinger, T. & Burgert, I. Mesoporosity of delignified wood investigated by water vapor sorption. *ACS Omega*, 4(7), 12425-12431, (2019), <https://doi.org/10.1021/acsomega.9b00862>. (*: Co-first authors)
5. Mahrt, F., Kilchhofer, K., Marcolli, C., **Grönquist, P.**, David, R. O., Rösch, M., Lohmann, U. & Kanji, Z. A. The Impact of Cloud Processing on the Ice Nucleation Abilities of Soot Particles at Cirrus Temperatures. *Journal of Geophysical Research: Atmospheres*, 124, (2019), <https://doi.org/10.1029/2019JD030922>.
6. **Grönquist, P.**, Wood, D., Hassani, M. M., Wittel, F. K., Menges, A. & Rüggeberg, M. Analysis of hygroscopic self-shaping wood at large-scale for curved mass timber structures. *Science Advances*, 5(9), eaax1311, (2019), <https://doi.org/10.1126/sciadv.aax1311>.

SUBMITTED JOURNAL ARTICLES

7. Bockel, S., Harling, S., **Grönquist, P.**, Niemz, P., Pichelin, F., Weiland, G. & Konnerth, J. Characterization of wood-adhesive bonds in wet conditions by means of nanoindentation and tensile shear strength. *European Journal of Wood and Wood Products*.
8. **Grönquist, P.**, Pandchadcharam, P., Wood, D., Menges, A., Rüggeberg, M. & Wittel, F. K. Computational analysis of hygromorphic self-shaping wood gridshell structures. *Royal Society Open Science*.
9. Mahrt, F., Alpert, P., Dou, J., **Grönquist, P.**, Corral-Arroyo, P., Ammann, M., Lohmann, U. & Kanji, Z. A. Aging induced changes in ice nucleation activity of combustion aerosol as determined by near edge X-ray absorption fine structure (NEXAFS) spectroscopy. *RSC Environmental Science: Processes & Impacts*.

PATENTS

1. Rüggeberg, M., Burgert, I., **Grönquist, P.**, Menges, A. & Wood, D. Manufacturing method of shaped multi-layer plant-fibre based components. WO2019/180006 A1 & EP3543000 A1, (2019).

BOOK CONTRIBUTIONS

1. Wood, D., Menges, A., **Grönquist, P.**, Rüggeberg, M., Burgert, I., Bechert, S., Aldinger, L., Knippers, J., Riggenbach, D. & Lehmann, K. From machine control to material programming: Self-shaping wood manufacturing of a high performance curved CLT structure - Urbach Tower. *Fabricate 2020: Making Resilient Architecture* (edited by Burry, J., Sabin, J. E., Sheil, B. & Skavara, M.) ISBN: 9781787358119, (2020)

SELECTED CONFERENCE CONTRIBUTIONS

INTERNATIONAL CONFERENCES

1. **Grönquist, P.**, Wittel, F. K. & Rüggeberg, M. Predicting the actuation of large-scale smart wooden bilayer systems. Oral talk at *3rd Euro Intelligent Materials 2017*. Kiel, Germany, 07-09 June 2017.
2. **Grönquist, P.**, Wittel, F. K. & Rüggeberg, M. Upscaling of Self-actuated Wooden Bilayers. Proceedings paper & oral talk at *7th GACM Colloquium on Computational Mechanics for Young Scientists from Academia and Industry*. Stuttgart, Germany, 11-13 October 2017.
3. **Grönquist, P.**, Wittel, F. K. & Rüggeberg, M. Mechanical Analysis of Wooden Bilayer Structures and Novel Application Possibilities in Timber Industry. Oral talk at *ASCE Engineering Mechanics Institute Conference 2018*. Cambridge, Massachusetts USA, 29 May - 01 June 2018.
4. **Grönquist, P.**, Frey, M., Thybring, E. E. & Burgert, I. Measuring hydroxyl accessibility of delignified wood by deuterium exchange. Invited oral talk at *1st European Symposium on Sorption Science*. Vienna, Austria, 05-07 September 2018.
5. **Grönquist, P.**, Wood, D., Wittel, F. K. & Rüggeberg, M. 4D self-shaping mechanisms for achieving double-curved wooden structures. Oral talk at *ECCOMAS International Conference on Computational Methods in Wood Mechanics 2019*. Växjö, Sweden, 17-19 June 2019.
6. **Grönquist, P.**, Wittel, F. K. & Rüggeberg, M. Modelling of self-shaping wood composites. Oral talk at *15th Annual Meeting of the Northern European Network for Wood Science and Engineering*. Lund, Sweden, 09-10 October 2019.

COLLOQUIA & SYMPOSIA

7. **Grönquist, P.**, Wittel, F. K. & Rüggeberg, M. Predicting the Actuation of Wooden Bilayers at Large Scale. Oral talk at *11th BOKU, ETH, Empa, and University of Freiburg Wood Science and Technology Doctoral Colloquium*. Tulln an der Donau, Austria, 28-29 August 2017.

8. **Grönquist, P.**, Frey, M., Thybring, E. E. & Burgert, I. Measuring hydroxyl accessibility of delignified wood by deuterium exchange. Oral talk at *12th BOKU, ETH, Empa, and University of Freiburg Wood Science and Technology Doctoral Colloquium*. Freiburg, Germany, 13-14 September 2018.
9. **Grönquist, P.**, Wood, D., Wittel, F. K., Burgert, I., Menges, A. & Rüggeberg, M. Sustainable Timber Architecture with Complex Geometry using Self-Shaping Manufacturing. Poster at *ASB Meet & Share Your Research Day at D-BAUG, ETH Zurich*. Zurich, Switzerland, 23 October 2018.
10. **Grönquist, P.**, Wood, D., Wittel, F. K. & Rüggeberg, M. Sustainable Timber Architecture with Complex Geometry using Self-Shaping Manufacturing. Oral talk at *Empa PhD Students Symposium*. Dübendorf, Switzerland, 26 November 2018.
11. **Grönquist, P.**, Rüggeberg, M. & Wittel, F. K. Computational analysis of hygromorphic self-shaping wood gridshell structures. Oral talk at *13th BOKU, ETH, Empa, and University of Freiburg Wood Science and Technology Doctoral Colloquium*. Dübendorf, Switzerland, 04-05 November 2019.

STUDENT SUPERVISION

1. Vanessa Studer, *Bestimmung herstellungsinduzierter Eigenspannungen von Holzbilayern*, BSc thesis, spring semester 2017, ETH Zurich, P. Grönquist, Dr. F. Wittel, Dr. M. Rüggeberg, Prof. Dr. I. Burgert, Prof. Dr. H. Hermann.
2. Jennifer Furrer, *Bestimmung herstellungsinduzierter Eigenspannungen von Holzbilayern*, BSc thesis, spring semester 2017, ETH Zurich, P. Grönquist, Dr. F. Wittel, Dr. M. Rüggeberg, Prof. Dr. I. Burgert, Prof. Dr. H. Hermann.
3. Anselmo Malvetti, *Bestimmung herstellungsinduzierter Eigenspannungen von Holzbilayern*, BSc thesis, spring semester 2017, ETH Zurich, P. Grönquist, Dr. F. Wittel, Dr. M. Rüggeberg, Prof. Dr. I. Burgert, Prof. Dr. H. Hermann.
4. Christina Siegrist, *Einfluss des Schichtdickenverhältnisses auf die Verformung von Holzbilayern*, MSc project thesis, autumn semester 2017, ETH Zurich, P. Grönquist, Dr. M. Klippel, Dr. M. Rüggeberg, Prof. Dr. A. Frangi.
5. Jeannine Herrsche, *Entwurf und Analyse von 4D Holzstrukturen: Doppelt-gekrümmte flächige Holzstrukturen infolge anisotropen Quellens*, BSc thesis, spring semester 2018, ETH Zurich, P. Grönquist, Dr. F. Wittel, Dr. M. Rüggeberg, Prof. Dr. I. Burgert.
6. Prijanthi Padchancharam, *Entwurf und Analyse von 4D Holzstrukturen: Holzbilayer als Streben von 3D-gekrümmten Gitterschalenstrukturen*, BSc thesis, spring semester 2018, ETH Zurich, P. Grönquist, Dr. F. Wittel, Dr. M. Rüggeberg, Prof. Dr. I. Burgert.
7. André Hägeli, *Entwurf und Analyse von 4D Holzstrukturen: Holzbilayer als Gelenkelemente von räumlichen Strukturen*, BSc thesis, spring semester 2018, ETH Zurich, P. Grönquist, Dr. F. Wittel, Dr. M. Rüggeberg, Prof. Dr. I. Burgert.
8. Lucas Schnell, *Entwurf und Analyse von 4D Holzstrukturen: Keile aus verdichtetem Holz*, BSc thesis, spring semester 2018, ETH Zurich, P. Grönquist, Dr. F. Wittel, Dr. M. Rüggeberg, Prof. Dr. I. Burgert.

9. Raphaela Hellmayr, *Untersuchen des Einflusses der Jahrringneigung und der Jahrringstellung auf die Voraussagbarkeit der Krümmung von Holzbilayern mit FE Modellen*, MSc internship, July-August 2018, BOKU Vienna, P. Grönquist, Dr. M. Rüggeberg.
10. Luca Imfeld, *Parameterstudie zur Überhöhung mittels Quelldruck von Bucheneinlagen*, MSc thesis, autumn semester 2018, ETH Zurich, K. Müller, P. Grönquist, Prof. Dr. A. Frangi.
11. Luca Angst, *Design and analysis of 4D wood*, BSc thesis, spring semester 2019, ETH Zurich, P. Grönquist, Dr. F. Wittel, Dr. M. Rüggeberg, Prof. Dr. I. Burgert.
12. Minxiang Gao, *Identification of nonlinear behavior in spruce bilayer deformation*, MSc project thesis, spring semester 2019, ETH Zurich, P. Grönquist, Dr. F. Wittel, Dr. M. Rüggeberg, Prof. Dr. I. Burgert.

INSTITUTE RELATED RESPONSIBILITIES

TEACHING RESPONSIBILITIES

1. *Werkstoffe III: Holz und Holzwerkstoffe: Quellverhalten und Mikromechanik*. Practical course, autumn semester 2017, Civil engineering BSc programme, ETH Zurich.
2. *FE Analysis with Abaqus and Python Scripting*. Workshop, 02 March 2018, Computational physics & Wood materials science BSc and MSc project & thesis students, ETH Zurich.
3. *Werkstoffe III: Holz und Holzwerkstoffe: Makromechanische Prüfungen*. Practical course, autumn semester 2018, Civil engineering BSc programme, ETH Zurich.
4. *Werkstoffe III: Holz und Holzwerkstoffe: Makromechanische Prüfungen*. Practical course, autumn semester 2019, Civil engineering BSc programme, ETH Zurich.

LABORATORY RESPONSIBILITIES

1. Dynamic vapor sorption instrument: Laboratory device responsibility (maintenance, measurements, data analysis).
2. Group IT administration: Partial responsibility (software & hardware).

DECLARATION

I, Philippe Grönquist, declare that this thesis is my own work and has not been submitted in any form for another degree or diploma at any university or other institute. Information derived from the published and unpublished work of others has been acknowledged in the text and a list of references is given in the bibliography.